

AD-A245 360



✓ ①

**POLAR LOWS OVER THE NORTHEAST GREENLAND SEA**

**Occurrence, structure, dynamics and development**

**DTIC**  
**ELECTE**  
**S D**  
**JAN 29 1992**

Erik A. Rasmussen  
University of Copenhagen

Torben S. Pedersen  
The Danish Meteorological Institute

This document has been approved  
for public release and sale; its  
distribution is unlimited.

December 1991

**92-02284**



92 1 28 065

~~92 1 0 110~~

Office of Naval Research

under Grant No.: N00014-87-G-0232,



Accession For	
NTIS CRA&I	<input checked="" type="checkbox"/>
DTIC TAB	<input type="checkbox"/>
Unannounced	<input type="checkbox"/>
Justification	
By _____	
Distribution/	
Availability Codes	
Dist	Avail and/or Special
A-1	

## Table of Contents

1. INTRODUCTION .....	1
1.1 Purpose and motivation for the project .....	1
2. BACKGROUND .....	2
2.1 A general description .....	2
3. POLAR LOWS AROUND GREENLAND .....	3
4. AN OBSERVATIONAL CASE STUDY .....	5
4.1 The initial polar low formation (the baroclinic phase) .....	6
4.2 The convective phase (phase 2) .....	7
4.2.1 The formation and development of arctic instability lows C and C* .....	9
5. METHODS OF ANALYSIS AND RESULTS .....	10
5.1 Diagnostic studies by means of different versions of the omega equation .....	10
5.1.1 The models .....	10
5.1.2 Forcing in the quasi-geostrophic omega-equation .....	13
5.1.3 Semi-geostrophic diagnostics .....	13
5.1.4 Concluding remarks .....	15
5.2 CISK versus "Free Ride" .....	16
5.2.1 A general solution to CISK .....	17
5.2.2 CISK and integrated Free Ride .....	19
5.2.3 Free Ride and CISK .....	20
5.2.3.1 Integrated Free Ride .....	21
5.2.3.2 Local Free Ride .....	22
5.2.4 Local and integrated balance in CISK .....	23
5.2.5 Conclusions .....	24
5.3 Numerical modelling studies .....	24
5.3.1 The HIRLAM model .....	25
5.3.1.1 Data assimilation .....	25
5.3.1.2 IPV analysis .....	27
5.3.2 The RAMS model .....	30
5.3.2.1 Simulation of the December 13 - 14, 1982 Bear Island case .....	31
5.3.2.2 Simulation of an arctic boundary layer front .....	33
5.3.2.3 Representation of clouds in the RAMS .....	35
6. CONCLUDING REMARKS .....	35
7. ACKNOWLEDGMENTS .....	37
8. REFERENCES .....	38
9. FIGURE LEGENDS .....	42
11. DISTRIBUTION .....	48

12. FIGURES .....	49
-------------------	----

## 1. INTRODUCTION

### 1.1 Purpose and motivation for the project

The purpose of the project reported on in this report has been to increase our knowledge of polar low occurrence, structure and dynamics in the Greenland region. To achieve this different methods have been applied including the use of diagnostic studies, theoretical analysis, and numerical modelling studies.

Polar lows are small scale cyclonic storms with gale or storm winds which occur in high latitudes. These storms are still not regularly depicted on the traditional meteorological charts and are often too small for detection by operational numerical weather analysis models, and therefore, rarely predicted. Twitchell and Fett (1988) pointed out, "that improved satellite observational capability combined with advanced numerical mesoscale weather analysis and prediction models will provide the basis for better detection and more accurate forecasting of these storms."

In Section 2 we will briefly present some basic information about polar lows. For a more detailed discussion the reader is referred to Twitchell et al. (1989).

Polar lows are known to be quite frequent in the Norwegian Sea and surrounding waters and much of the recent years research has been focused on developments in that region. However, polar lows are known to occur in other regions as well and the results of a pilot project on the occurrence of polar lows around Greenland will be reported on in Section 3.

Detailed case studies of polar lows development are relatively few because of lack of data. One relatively well documented development from December 1982 in the region around Bear Island in the Northeastern part of the Norwegian Sea has been used for validation purposes for the numerical experiments carried out as part of the project. A short description of this particular development is presented in Section 4.

Satellite images are an indispensable tool for polar low research and were used extensively in the study of the Bear Island development referred to above. In most studies so far, however, only imagery from polar orbiting satellites has been used since most polar lows develop at so high latitudes that data from geostationary satellites have been considered of little value. Some polar lows which develop relatively far South can, however, be studied by means of data from geostationary satellites, as demonstrated in a recent study (Rasmussen and Purdom, 1992). This study of a polar low development over the Labrador Sea between Southern Greenland and the coast of Labrador demonstrates, that in certain cases, dependent on the position of the satellite subpoint relative to the polar low, it is possible to compute the near surface wind field in detail as far as 65°N by a cloud tracking technique using high resolution images from geostationary satellites.

As indicated above, the study of polar lows dynamics and development is hindered by the lack of sufficient "in situ" data. To overcome this difficulty several approaches were attempted including the use of diagnostic models based on different form of the so-called omega equations. The results of these experiments are described in Section 5.1.

The idea of CISK (Conditional Instability of the Second Kind) and its importance for the formation and development of polar lows has played an important role in the on-going debate on polar lows since the end of the seventies (Rasmussen 1977, 1979, and Oekland 1977), (for an excellent discussion see van Delden 1989 a,b). As part of the project a comparison between the so-called "Free Ride balance" (Fraedrich and McBride, 1989) and a linear CISK model was carried out (Pedersen, 1991), and is described in Section 5.2.

For reasons indicated above much research of the detailed processes involved in the formation of polar lows must rely on the use of high resolution numerical models, which as stressed by Nordeng (1987) are powerful tools for such studies. As part of this study we made use of the High Resolution Limited Area Model (HIRLAM) developed by a joint Nordic / Dutch project and the Regional Atmospheric Modelling System (RAMS) developed at the Colorado State University by the Cotton - Pielke group. The results of these numerical experiments are described in Section 5.3, followed by a discussion and concluding remarks in Section 6.

## 2. BACKGROUND

### 2.1 A general description

Our knowledge of polar lows is of relatively recent origin and only 10 to 15 years ago most meteorologists were unaware of their existence. Satellite images like Fig. 2.01 demonstrate, however, that polar lows exist as phenomena in their own right. Going through the meteorological literature very little can be found about polar lows prior to Harrold and Browning's 1969 paper "The polar low as a baroclinic disturbance". What can be found shows that before 1969 the polar low was considered as a mainly non-frontal, convectively driven system. Harrold and Browning's paper marked the beginning of a debate about the structure and nature of the polar low. In their paper they concluded that the polar low is basically a baroclinic wave of short wavelength. This point of view was challenged by Scandinavian meteorologists, Rasmussen (1977, 1979) and Oekland (1977), who both supported the older point of view that polar lows were driven by deep convection, and that baroclinic instability played a minor role for many polar low developments. Both authors made use of the theory of Conditional Instability of the Second Kind (CISK) known from tropical meteorology studies, and much of the following years debate was concentrated upon which of these basic mechanisms, i.e. baroclinic instability or CISK were predominant for polar low developments. In particular Rasmussen and Oekland demonstrated, that even over ocean regions as far North as the Norwegian and the Barents Sea sufficient energy in form of latent and sensible heat was available to drive "convective" type polar lows.

Many of the original points of dispute between the "baroclinic" and the "convective" point of view have now been solved in that way, that we actually can think of a whole "spectrum" of polar lows, stretching from purely baroclinic systems to systems completely or almost so driven by convection. Polar lows typically form in regions where many forcing mechanisms are effective, and it is not surprising that they appear in so many forms. Many form for example very close to the

ice-edges in the arctic regions, along which shallow baroclinic zones often are observed. Baroclinic instability therefore must be expected to play an important role for some polar low developments, especially during their early stage of formation. Other polar lows which form in deep unstable air masses are much more influenced by convection.

Because of the many types of polar lows observed it is difficult to give a short and concise definition which covers all relevant aspects of the phenomenon. A useful definition, which in most but not all respects is similar to the definition proposed by Businger and Reed (1989), and which reflects the most basic observations sounds: "A polar low is a small-scale synoptic or sub-synoptic cyclone that forms in the cold air masses poleward of the main baroclinic zone and/or major secondary fronts. It will often be of convective nature, but baroclinic effects may be important as well". The proposed definition (Rasmussen, 1989) includes beside "real" polar lows of the convective type, comma clouds, baroclinic polar lows, as well as hybrid types.

Polar lows have been observed to form at many places at especially the Northern hemisphere, including the Pacific (Ninomiya, 1989), the Gulf of Alaska (Businger, 1987), and the Davis Strait and the Labrador Sea (Rasmussen and Purdom, 1992). However, the best known and one of the most active genesis area for polar lows is probably the Norwegian Sea (and the Barents Sea). These waters are often affected by cyclonic outbreaks of very cold air masses from ice and snow covered regions farther North, which, combined with the relative high sea surface temperatures in the region often results in the formation of polar lows. Because of strong sensible and latent heat fluxes in this particular region with a sea surface temperature reaching 6 to 8 °C even in the winter months, the originally very stable air masses often become conditionally unstable. Following this, deep convection may develop which in many cases result in the formation of polar lows as reflected in the statistics by Wilhelmsen (1985).

Since the present work partly has been focused on polar lows developments around Greenland a pilot study of the occurrence of polar lows around Greenland was carried out, based mainly on a subjective evaluation of satellite images, supported by conventional synoptic data. The use of a combination of synoptic data, satellite images and conceptual models quite often (but not always) makes possible a reliable description of the basic mechanisms involved in a particular polar low formation. The result of this pilot study demonstrates that polar lows occur quite frequently along all parts of the Greenland coast except the very Northerly parts where the sea is permanently frozen. Also the pilot study demonstrates the strong local forcing involved in most polar low developments in the region. It is because of the special local forcing factors that it is reasonable to talk for example of "Labrador Polar Lows", or "Davis Strait Polar Lows". Although these two types of lows develop in regions close to each other the lows nevertheless are quite different.

### 3. POLAR LOWS AROUND GREENLAND

West of the genesis regions for polar lows in the Bear Island region, i.e. over the Northeast Greenland Sea (see Fig. 3.01) and close to the extended pack ice region along the Northeast Greenland coast the sea surface temperature is low. Close to the ice edge the temperature of the water will be maintained at a constant -1.7 °C

due to the presence of ice which forms and melts at this temperature. Because of this (and for other reasons as well) the frequency of polar lows is relatively small in this region. Also the general type of polar lows observed is different from the ones seen farther East near Bear Island.

It is interesting to compare the conditions along the coast of Greenland with the conditions around the antarctic continent. Although the area of Antarctica is around six times that of Greenland and the height of the ice cap somewhat larger significant similarities in meteorological conditions might be expected. Significant differences may be expected as well. While the interior part of Antarctica is little affected by synoptic low pressure systems, large parts of the Greenland ice cap quite often are "ventilated" by large scale cyclonic systems. Strangely enough very little meteorological research has been directly aimed at the conditions over and around Greenland, and the consequences of this enormous ice cap for the regional weather. On the other hand much interest has been focused upon the meteorological conditions around Antarctica in the last 20 years or more, resulting in a relatively good knowledge about the conditions in this region. One of the most interesting features of Antarctic weather is the so-called drainage winds occurring over the interior part of the continent and the associated fall or katabatic winds which are found in the coastal regions. For a recent discussions of these phenomena see for example Parish and Weadler (1991) and Parish and Bromwich (1991).

It has been hypothesized (Parish and Bromwich, 1986) that fall winds along the coast of Antarctica might lead to the formation of polar lows and similar fall winds along the Greenland coast sometimes plays an important role for the formation of polar lows. Fig. 3.02 shows the topography of Greenland as well as some characteristic streamlines for drainage and katabatic flows (Rasmussen L., 1989). While the drainage flows over the gently sloping interior icefield can be considered as being in quasi-geostrophic balance with only weak to moderate winds speeds, the katabatic winds in the coastal regions are much more intense and more closely aligned with the fall line. Like in Antarctica these strong fall winds will be topographically channelled as indicated on Fig. 3.02. A region where the topography as well as the streamlines shown on Fig. 3.02 indicate that strong outflow is possible is found around Angmagssalik at South East Greenland, and actually small scale polar lows have been observed to form in this particular region as shown on Fig. 3.03. Another, although less pronounced region of outflow is found around Danmarks Havn in North East Greenland near 77°N. However, as pointed out by Rasmussen L. (1989) the climate in this region is extremely cold, and katabatic winds descending from the interior ice cap only rarely reach the surface.

In certain cases, however, when other forcing mechanism contribute, polar lows are observed to form in the coastal areas even in this region. In connection with the passage of synoptic scale frontal waves over Greenland from West to East, a strong upper level flow will be established over the ice cap. In these circumstances strong vertical stretching will take place along the East Greenland coast which contribute to low level cyclogenesis. Satellite images from such situations do show cases of induced low level cyclonic circulations which occasionally develop into polar lows. A likely example of such a development is briefly discussed in the following.



On November 15, 1987 a "wave train" consisting of three lows/troughs occurred within a reverse shear (the thermal wind in this case is opposite to the surface wind) baroclinic zone stretching from Novaya Zemlya to the Baffin Bay (Fig. 3.04) far North of the polar front. Formations of polar lows on reverse shear zones are quite common further South over the Norwegian Sea, but are seldom observed so far North as in this case. On the following day, November 16, a rather intense small scale polar low had developed in an unusual position Northeast of Danmarks Havn, over the pack ice (Fig. 3.05) and could still be observed the following day (Fig. 3.06). It is hypothesized that the low reached its relatively strong intensity partly due to vertical stretching of air descending from the ice cap.

Studies from Antarctica (Parish and Bromwich, 1986) and Greenland (Rasmussen L., 1989) have shown, that fall winds, channelled by the topography, show a warm "katabatic signature" on the infrared satellite images. Satellite images from 16th November 1987 when the polar low was best developed show such a "katabatic signature" in the Danmarks Havn-region.

Although the temperature of katabatic winds increase due to adiabatic compression as the flow descends the steep slopes in the coastal region, these winds nevertheless are believed to be negatively buoyant throughout their descent. The puzzling feature that they are accompanied by simultaneously satellite observations of a warm thermal-infrared "katabatic signature" has been explained to be a consequence of strong vertical mixing within the boundary layer (see Parish and Bromwich, 1986).

Southwest of Cape Farewell a genesis region for polar low developments has recently been identified over the Labrador Sea (Rasmussen and Purdom, 1992). Here as elsewhere the genesis region seems to be linked to the local orography. A characteristic example of a polar low over the Labrador Sea is shown in Fig. 3.07. The formation of this low is connected with an outbreak of extremely cold arctic air. The development took place in the central part of the cold air dome permitting deep convection to develop.

Polar lows also have been observed to form quite frequently further North in the Davis Strait and in the Southern part of the Baffin Bay. As usual these lows form over water, although a few examples have been observed which originated over land. The "Davis Strait lows" of which an example has been shown in Fig. 3.08 often form in connection with the passage of a major baroclinic wave further South near Cape Farewell. Also in this case katabatic flows from the interior Greenland may play an important role for the polar low formation.

#### 4. AN OBSERVATIONAL CASE STUDY

As pointed out in Section 2 the formation and structure of some (most) polar lows is very complex. Phenomena on different horizontal scales interact in a manner not very well understood but convection and baroclinic instability are both important. While some developments including predominantly baroclinic cases have been successfully simulated by numerical models (Nordeng, 1987, Nordeng and Rasmussen 1992), then on the other hand others where convection seems to be the primary driving mechanism still present serious problems for the models (and the modellers). Because polar lows invariably develop in data sparse regions only very few well documented cases can be found in the literature. For the present investigation the December 1982-case first discussed by Rasmussen (1985a,b) was

chosen as the subject for numerical experiments with the HIRLAM and RAMS. Some additional studies of December 1982-case were carried out as part of this project and will be presented in the following (for a more detailed discussion see Rasmussen 1985a,b, 1989, and Rasmussen et al., 1991).

#### 4.1 The initial polar low formation (the baroclinic phase)

In Rasmussen (1985a), in the following referred to as R85, it was shown that the Bear Island polar low originated from an upper level cold core vortex whose origin could be traced Eastward as far as Novaya Zemlya. Fig. 4.01 shows the sea ice boundaries and sea surface temperatures in December 1982. The geographical locations mentioned in the text is shown in Fig. 3.01. A satellite mosaic-picture from around 1300 UTC December 12, 1982 shows the first polar low (A) in the incipient stage just West of Bear Island (Fig. 4.02). East of Scandinavia (seen in the middle of the picture) the two arrows marked B indicate the polar front. Apart from the clouds associated with polar low A relatively few high clouds are seen over the arctic region North of 70 N. Fig. 4.02 illustrates in a striking way how polar lows in the Bear Island region can develop far North of the main baroclinic zone, i.e. the polar front.

Fig 4.03. gives a detailed view of the low and its surroundings. The Eastern part of the relatively high clouds West of Bear Island associated with the upper level disturbance form a comma which merges with another region of upper level clouds farther West. At low levels very cold air is streaming out from the ice edge stretching from West of Svalbard to Bear Island. Somewhat modified air which can be traced back to the region between Northern Svalbard and Northeast Greenland, can be seen farther West. As the low level disturbance develops close to the ice very cold air masses are drawn into the circulation and advected in a Southerly direction. Subsequently a sharp arctic front with deep convection develops at the leading edge of the shallow cold air outbreak. Before the onset of deep convection the ascent around the incipient polar low is dynamically forced, and both upper level differential vorticity advection as well as low level thermal advection are likely to be important. The development therefore is baroclinic. The radiosonde ascent from Bear Island 12 UTC, 12 December (R85, Fig. 9a) close to the time of the satellite image (Fig. 4.03) confirms that the clouds associated with the comma are due to stable ascent, and that free convection from the surface is very unlikely at this time.

In the following hours the disturbance seen on Fig. 4.03 developed into the impressive cloud spiral seen on Fig. 4.04. The disturbance, however, was still mainly confined to upper levels and only a weak trough was discernible at the surface (see R85).

A problem highly relevant to researchers and operational meteorologists is, that the cloud vortex associated with the developing polar low and seen on Fig. 4.04 does not fit at all into any of the conceptual models normally applied for developing cyclones. The formation of the cloud vortex is best understood as the result of an upper level IPV-anomaly as briefly discussed in Section 5.3.

## 4.2 The convective phase (phase 2)

Between December 13, 1500 UTC and 1800 UTC the wind at weather ship AMI (71.5 N, 19 E) increased from 10 to 15 m/s without any significant change in the surface pressure. At 1740 UTC a satellite image (not shown) showed convective cells close to the center of a rather weak synoptic scale surface low resulting from the baroclinic processes discussed above, and a little West of AMI. These cells were situated in a region where the sea surface temperature was as high as 8 °C. The increased wind at weather ship AMI may be explained as the response of an increased pressure gradient caused by pressure falls on a very small horizontal scale associated with the observed strong localized convection in the center of the synoptic scale low. The convective cell observed in the central region of the low mark the starting point of the convective development leading to the formation of an intense subsynoptic vortex in the evening on December 13, 1982. A very similar development in the Mediterranean was discussed by Rasmussen and Zick (1987).

An intense vortex/polar low is seen on the surface maps from December 14, 0000 (Fig. 4.05) and 0300 UTC (the whole sequence of surface maps from the period was shown in R85). A satellite image close to that time, i.e. from 0419 UTC is shown in Fig. 4.06. The horizontal scale of this low as defined by the closed 990 hPa-isobar is around 500 km, i.e. similar to the scale of the baroclinic disturbance discussed in the preceding. An analysis of the data shows, however, that the development during this phase (phase two) is dominated by the formation of a phenomenon on a much smaller horizontal scale. Already the observations from AMI at 1800 UTC, December 13 and the satellite images from 1740 UTC and 1921 UTC indicate, that disturbances on the mesoscale were embedded in the synoptic scale circulation. In the following we will discuss this part of the development in more detail making use of satellite images and observations from AMI which were not available for the study reported in R85.

Before the start of phase 2 the vertical lapse rate in the region of the polar low development was approximately given by a "modified" Bear Island sounding. The modified sounding was based on the 1200 UTC Bear Island sounding from December 13 (Fig. 4.08), but assuming a surface based well mixed neutral layer with a (constant) potential temperature corresponding to the surface temperature measured at AMI, i.e.  $\theta = 272$  K up to around 850 hPa. The low level neutral layer in the modified sounding is caused by strong sensible heat fluxes at the surface, and the sounding is representative for the vertical stratification just prior to the formation of the intense vortex. (Emanuel and Rotunno (1989) used a similar modified sounding for their "Hot, Dry-case"). After the onset of the deep intense convection the vertical stratification in the central region of the low corresponds approximately to the moist adiabat  $\theta_w = 274$  K.

During the passage of polar low A at AMI around midnight between December 13 and 14 the value of  $\theta_w$  increased significantly as seen from Fig 4.07. This increase was partly due to an increase in the temperature and partly to an increase in the dew point. The relatively small decrease in surface pressure ( $p_s$ ) had little effect. (Ooyama (1969) mentions that for tropical cyclones a sharp decrease in  $p_s$  may rise  $\theta_w$  (and  $\theta_s$ ) significantly, and in this way "boost" the surface air shortly before it ascends into the warm core). The increase in the surface value of  $\theta_w$  is extremely

important for the potential for deep convection in the vortex. This is seen from Fig. 4.08 where curve III shows moist adiabatic ascent corresponding to the maximum  $\theta_w$  value (274 K) measured at AMI during the passage of the polar low.

By integrating the hydrostatic equation from the surface to H, the level of the tropopause, we find the following expression for the pressure decrement  $\Delta p_0$  at the surface due to an increase  $\Delta T$  in the mean temperature.

$$\Delta p_0 = \frac{g H p_0 \Delta T}{R T^2} \cong 4 \Delta T \quad (4.3.01)$$

By inspection of Fig. 4.08 we find that  $\Delta T \sim 3.5^\circ\text{C}$  which corresponds to a pressure fall  $\Delta p_0 \sim 14$  hPa. This is in fairly good agreement with the total pressure fall observed at AMI between 1800 and 2400 UTC December 13, 1982 and justify the assumption of a nearly moist adiabatic stratification in the cloud filled central region of the low where incidently no "eye" was observed. This mechanism of forming a warm core through the replacement of an unsaturated column of air with a cloud with a higher mean temperature is among the three different physical mechanisms mentioned by Anthes (1982, p 74-75) which may be responsible for the tropospheric warming necessary to produce a hurricane from a weak disturbance.

After the initial formation of the vortex a little West of AMI, it moved in an East to South-Easterly direction and the central region passed just over or very close to AMI. The mean wind velocity and pressure as function of time during the passage of the center are shown in Fig. 4.09. By means of the observed translation velocity of the vortex we can transform the time-axis into the equivalent length scale also shown on the figure. The distance between the wind-maxima on Fig. 4.09 is seen to be only around 100 km. The mean values of the wind velocity (10 minute mean-values) shown in Fig. 4.09 reach about 23 m/s. The instantaneous values and the wind directions are missing (except at the three-hourly synoptimes). Based on measurements from a similar vortex passing Bear Island on December 15, 1982 (see Section 4.2.2) we may assume, that the wind velocity in the (frequent) gusts may reach values as high as 40 m/s. Based on the variation of the surface pressure at AMI we might define the horizontal scale for the vortex by B-B shown on Fig. 4.09. This corresponds to a horizontal scale around 175 km.

At the beginning of phase two when rapid pressure falls set in, the general appearance of the satellite images undergo a complete change. The satellite image (Fig. 4.06) shows, that the synoptic scale low is in fact, at that time, a conglomerate of several subsynoptic/mesoscale phenomena, of which the most important is a tight vortex associated with the large convective cell near the center of the synoptic disturbance.

Emanuel (1983) points out that "Both linear and nonlinear studies have shown that baroclinic instability has a finite horizontal scale proportional to the deformation radius  $NH/f$ , while convective and symmetric instability seek very small scales". The striking predominance of convective clouds, the small horizontal scale of the central vortex, and the rapid, localized large pressure falls all indicate that convection is the driving mechanism. The formation of the tight vortex at the surface may be seen as the result of a rapid spin-up of vorticity associated with the pre-existing "large-scale" low due to localized deep convection in the central

region of the low. A very similar mode of formation of a tight subsynoptic vortex in a homogeneous but unstable air mass was as already mentioned observed in the Mediterranean development discussed by Rasmussen and Zick (1987).

#### 4.2.1 The formation and development of arctic instability lows C and C\*

After the spin-up process in the central region of the previously formed low, the resulting vortex (vortex A) can be followed for about 18 hours. Beginning around December 14, 1045 UTC, another subsynoptic disturbance, low C, develops around 73 N, 21 E, and later on, around midnight between the 14th and the 15th, a third mesoscale vortex C\* forms close to C. C\* rapidly takes over as the dominant one, while the "old" vortex C moves further Southwards under decay. C as well as C\* are true mesoscale phenomena with a horizontal scale even less than that of vortex A. Nevertheless they show a well defined horizontal structure with diminutive eye-like features. C and C\* both form in a region of vigorous convection close to the boundary between the shallow cold air to the West and the warmer unstable air mass to the East (see Fig. 4.10).

In Fig. 4.10 we actually can observe a whole "polar low-family" along the shallow arctic frontal zone analogous to the well known extratropical cyclone-family, with C in its decaying, C\* in its mature, and E in its developing stage. The term arctic instability low has sometimes although not very often been used synonymously with "polar lows". The term invokes convection is active and may be a good alternative name for this kind of very small vortices of convective nature. Vortices of the nature described here have not so far been discussed in the literature.

The center of C\* fortuitously passes very close to Bear Island around 1500 UTC December 15, 1982. Fig. 4.11 shows the instantaneous surface wind velocity, and Fig. 4.12 the surface pressure during the passage of C\*. Fig. 4.13 shows the 10 minutes mean wind and the surface pressure together. Provided the wind is caused by an (approximately) axisymmetric vortex (see Fig. 4.14) the wind shows an almost linear variation from the center where the velocity is very small to the region of maximum velocity around 25 km away corresponding to a core in solid rotation. The wind is very gusty and the ratio between the peak gust values and the mean wind is around 1.5 or a little higher. Altogether the measurements reveal a tight, symmetric vortex of "medium" intensity and of a surprisingly small horizontal scale around 150 km corresponding to B-B on Fig. 4.13. Note that the horizontal distance between the wind maxima is only around 75 km. Using the values of  $\Delta p$  and  $r$  corresponding to the distance from the center to the radius of maximum mean wind, i.e.  $\Delta p \sim 3$  hPa and  $r = 35$  km, we find that the gradient wind, is  $\sim 13$  m/s, in agreement with the observed wind. This fact together with other evidence indicate that balanced motion indeed occurs even at these very small horizontal scales and over a considerable time period as well.

Vortex C\* can, by means of satellite images, be followed on its track Westwards until it finally decays after "icefall" on the pack-ice at the coast of Northeast Greenland on December 16. Fig. 4.15 shows vortex C\* before the icefall at 0354 UTC December 16. Compared to 1400 UTC December 15 (Fig. 4.14) the structure has changed considerably and now resembles a baroclinic system of a very small scale. The high level cirrus close to the center are wrapped around the center and at low levels cold air from the pack ice has been drawn into the circulation.

## 5. METHODS OF ANALYSIS AND RESULTS

### 5.1 Diagnostic studies by means of different versions of the omega equation

The development of most atmospheric disturbances is well reflected in their fields of vertical velocity, and diagnostic studies based on the so called "omega-equations" can be found many places in the meteorological literature. One of the advantages of using an omega-equation is that the effect of the different forcing mechanisms on the development of the disturbance can easily be isolated.

In this work different versions of the omega-equation were applied in a diagnostic study of a polar low development to investigate if it is feasible to identify which forcing mechanisms are of primary importance.

The synoptic situation during the polar low development in mid December 1982 has been described in Section 4. The initial development is connected with an upper level cold core vortex (or positive IPV anomaly see Section 5.3.1.2) moving Southwards from the Svalbard region. Fig. 5.01 shows an analysis of the situation at 0000 UTC on December 13, 1982. During the next 24 hours the polar low moves toward Southeast and develops into a tight vortex with a surface pressure of 980 hPa. However, only the initial phase where baroclinic effects dominated was considered.

The data for this part of our study are based on an initialized analysis for December 13 at 0000 UTC, 1982. The data were originally produced by the HIRLAM group using the HIRLAM Base Line model for simulation of the polar low development with the PSU-NCAR limited area model Aakjær (1987).

#### 5.1.1 The models

We consider a hydrostatic and Boussinesq atmosphere on a polar stereographic f-plane. As vertical coordinate the pseudo height introduced by Hoskins and Bretherton (1972) is applied.

The models use 13 vertical levels and a 21 by 21 horizontal grid using grid distances of respectively 667 m and 200 km for the vertical and horizontal direction.

Traditionally the adiabatic forcing in the quasi-geostrophic omega-equation, QGO, has been described by two terms. One is the vertical derivative of vorticity advection, (AVO), and the other the Laplacian of the thermal advection, (ATH).

With the approximations mentioned above the adiabatic omega-equation can be written as

$$N^2 \nabla^2 w + f^2 \frac{\partial^2 w}{\partial z^2} = f \frac{\partial}{\partial z} (\bar{V}_s \cdot \nabla \zeta_s) - \frac{g}{\theta_0} \nabla^2 (\bar{V}_s \cdot \nabla \theta) \quad (5.1.01)$$

AVO                      ATH

This formulation has the drawback that AVO and ATH have a common and possibly significant part, (ACA),

$$\begin{aligned} f\vec{V} \cdot \nabla \frac{\partial \zeta}{\partial z} \\ \text{ACA} \end{aligned} \quad (5.1.02)$$

which cancels. Hoskins et al. (1978) showed that this problem is avoided if the  $\bar{Q}$  concept is used.

The solution to the omega-equation can be split up into three parts associated with the lower boundary condition ( $w_{EQG}$ ), the vorticity forcing ( $w_V$ ), and the thermal forcing ( $w_T$ ), respectively.

$$\begin{aligned} N^2 \nabla^2 w_{EQG} + f^2 \frac{\partial^2 w_{EQG}}{\partial z^2} &= 0 \\ N^2 \nabla^2 w_V + f^2 \frac{\partial^2 w_V}{\partial z^2} &= AVO \\ N^2 \nabla^2 w_T + f^2 \frac{\partial^2 w_T}{\partial z^2} &= ATH \end{aligned} \quad (5.1.03)$$

$w_V$  and  $w_T$  vanish at the lower boundary where  $w_{EQG}$  is given by Ekman-pumping.

The semi-geostrophic omega-equation, (SGO), is derived in two steps. First the geostrophic momentum approximation, (GMA), is made and then a coordinate and variable transformation as described by Hoskins (1975) and Hoskins and Draghici (1977) is performed.

The GMA is based on the assumption that the Rossby number

$$R_o = \frac{|d\vec{V}/dt|}{|f\vec{V}|} \quad (5.1.04)$$

is small. This is also the basic assumption behind the quasi-geostrophic approximation. However, the approach differs in the evaluation of the ratio between the rate of change of momentum and the Coriolis force. The quasi-geostrophic approximation applies horizontally uniform velocity and length scales giving the constraint  $V/L < f$ . In the GMA the ratio is considered separately for the direction along and perpendicular to the movement of an air parcel giving rise to two criteria for the smallness of the Rossby number

$$\frac{1}{V} \frac{dV}{dt} < f, \quad \frac{V}{r} < f \quad (5.1.05)$$

where  $V$  is the velocity and  $r$  the radius of curvature for an air parcel. These criteria, based on the Lagrangian view that the magnitude and direction of the momentum

of an air parcel must change little during the time  $f$ , are weaker than the Eulerian criterion used for the quasi-geostrophic approximation.

A consequence of the less restrictive criteria in the GMA is that the horizontal advection by the ageostrophic velocity is retained. The advected quantities like momentum and vorticity, though, are still represented by their geostrophic values.

Following Hoskins and Draghici (1977) the semi-geostrophic version of the omega-equation becomes

$$\nabla^2(q_* w^*) + f^2 \frac{\partial^2 w^*}{\partial Z^2} = 2 \nabla \cdot \bar{Q} \quad (5.1.06)$$

with the geostrophic potential vorticity,  $q_*$ ,  $w^*$  and  $\bar{Q}$  given by

$$q_* = (f + \zeta_*) \frac{\partial \theta}{\partial Z}; \quad w^* = \frac{f}{f + \zeta_*} w; \quad \bar{Q} = -\frac{g}{\theta_0} \left( \frac{\partial \bar{V}_x}{\partial X} \nabla \theta, \frac{\partial \bar{V}_y}{\partial Y} \nabla \theta \right) \quad (5.1.07)$$

Results from the semi-geostrophic model presented in the following are obtained as follows. With potential temperature, geopotential and geostrophic wind given in the physical space a transformation to the semi-geostrophic space is performed. Using a modified Barnes procedure as described by Maddox (1980) the data are interpolated to a regular grid. The omega-equation is solved in the semi-geostrophic space and the results presented in physical space.

To solve the omega-equation the vertical velocity must be specified at the boundaries of the model domain. The lower boundary is assumed to coincide with the top of the planetary boundary layer, (PBL), and  $w$  is given by the Ekman-pumping. At the top and the lateral boundaries  $w = 0$  is assumed.

The classic Ekman-pumping is obtained by matching quasi-geostrophic dynamics with that of the Ekman-layer. This yields

$$w_{EQG} = \frac{1}{2} \left( \frac{2K}{f} \right)^{\frac{1}{2}} \zeta_* \quad (5.1.08)$$

which is used as the lower boundary condition for the QGO.

Wu and Blumen (1982) derived an Ekman-pumping formula consistent with the GMA by incorporating this approximation in the Ekman-layer dynamics

$$w_{EGM} = \frac{1}{2} \left( \frac{2K}{f} \right)^{\frac{1}{2}} \left\{ \underbrace{\zeta_*}_{w_{EQG}} - \underbrace{\frac{1}{4f} \bar{V}_* \cdot \nabla \zeta_*}_{w_{ISA}} - \underbrace{\frac{3}{4f} \bar{k} \cdot \nabla \times (\bar{V}_* \zeta_*)}_{w_{CRO}} \right\} \quad (5.1.09)$$

Here as in Wu and Blumen (1982) the effect of ageostrophic divergence at the top of the PBL is assumed to be negligible. The term,  $w_{EQG}$ , corresponds to the quasi-geostrophic Ekman-pumping, (5.1.08), and is related to the divergence of the viscous stress. The advection of geostrophic vorticity expressed by the second



term,  $w_{ISA}$ , accounts for the effect of the isallobar wind in the boundary layer. Finally, the last term,  $w_{CRO}$ , is associated with the cross isobar flow which is needed to balance the viscous stress.

### 5.1.2 Forcing in the quasi-geostrophic omega-equation

In connection with the study of polar lows in the region near Bear Island it is appealing to express the forcing in the conventional way as shown in Eq. (5.1.01). The contrast between the cold ice pack and the relatively warm Norwegian current gives rise to marked differences in the temperature at low levels (see Fig. 4.01). Thus, the ATH term can be expected to be significant at the lower levels. At upper levels the AVO term can be expected to be dominant as the development is associated with a Southward moving upper level vortex.

Figure 5.02 shows a cross section of the vertical velocity fields associated with the different terms expressing the adiabatic forcing. In the vicinity of the polar low ATH dominates AVO practically everywhere. The figure shows that ACA can be significant giving contributions that equals or even exceeds the total magnitude of the ATH and AVO terms.

That the thermal forcing dominates vorticity forcing at upper levels in the vicinity of the low is somewhat surprising. Generally it is expected that ATH is most significant at low levels and AVO at higher levels, see for example Reed (1985).

The fact that ATH does not produce significant velocities at low levels is probably connected with the vertical resolution in model. The lowest level where ATH is evaluated corresponds to 1.334 km.

To get an idea of the effect of the thermal forcing in the lowest part of the atmosphere a version of the model without Ekman-pumping has been tested. In this case the lower boundary is placed at the surface with  $w = 0$  so that the AVO and ATH forcing can be included at the 667 m level. The result (not shown) does not vary much from that obtained previously, except, of course, for the lack of the Ekman-pumping contribution. Along the ice edge North of the polar low where most of the baroclinicity is confined below 1 km ATH still does not give rise to the largest vertical velocities at low levels, partly because the geostrophic wind is nearly aligned with the isotherms at this time. Satellite images and observations, however, indicates the presence of shallow frontal structures over the sea which may yield ATH forcing. These features are not present in this HIRLAM analysis.

Anyway, it is somewhat misleading to talk of the forcing as being dominated by thermal or vorticity effects in this case. As noted earlier the cancellation term which contributes to both the thermal and the vorticity forcing constitute a major part of both of them.

### 5.1.3 Semi-geostrophic diagnostics

The polar low considered here has a scale of  $\sim 500$  km and application of the quasi-geostrophic approximation on phenomena on this scale may be doubtful. Especially if the ageostrophic horizontal advection is of importance use of the more general GMA, might give differing results.

It has not been possible to check directly if criteria (5.1.05) is fulfilled as the constraints are expressed in a Lagrangian frame of reference and only data from one analysis were available for the study. Of the two criteria in (5.1.05) the curvature term is most apt of being violated. However, since the development takes place North of 70 N  $f$  is relatively large. Using this high value of  $f$  and the curvature of the isohypes to evaluate  $r$  (instead of the curvature of the trajectory for an air parcel) we do not find a violation in the vicinity of the polar low.

The solution to the SGO is shown in Fig. 5.03(1) for the same cross section as in Fig. 5.02. A comparison with the quasi-geostrophic solution (Fig. 5.02(1)) reveals a few qualitative differences. Most notably the SGO yields a stronger updraft at lower and a weaker at higher levels around the polar low.

As noted in Section 5.1.1 the Ekman-pumping used for the SGO, Eq. (5.1.09), includes two additional terms. Wu and Blumen (1982) found for an idealised, steady, axisymmetric circular vortex that the magnitude of  $w_{EGM}$  was larger in anti-cyclones and smaller in cyclones compared to  $w_{EQG}$ . The difference according to their Fig. 3 ranging from 0 to about 60% depending on the Rossby number and distance from the centre of the vortex. This tendency of a reduced upward motion in a cyclonic region is also found here. However, the magnitude is less than 0.1 % near the polar low. Actually, the largest values found in this case for  $w_{ISA}$  and  $w_{CRO}$  are  $-6 \cdot 10^{-5}$  cm/s and  $-4 \cdot 10^{-4}$  cm/s respectively. They are associated with a major low East of the Kola Peninsula where  $w_{EQG} \approx 4$  cm/s. Consequently the difference between the SGO and QGO solutions cannot be ascribed to the change in the Ekman-pumping formulation but must primarily be associated with the effect of the ageostrophic horizontal advection.

Blumen and Wu (1983) studied the effect of an Ekman-layer on baroclinic instability including the effect of ageostrophic divergence ( $w_{DIV}$ ) at the top of the PBL in the Ekman-pumping. They found that  $w_{DIV}$  had an amplitude of approximately half the value of  $w_{ISA}$  and  $w_{CRO}$ . As these terms yields insignificant contributions to  $w_{EGM}$  in this case our negligence of  $w_{DIV}$  seems justified.

Figure 5.03(1) shows that the adiabatic forcing produces ascent in the region of the incipient polar low, but only of a modest intensity. However, this forced ascent may help to organise the convection. Already at 0250 UTC a satellite image (see Rasmussen (1985b) Fig. 4) shows intense convection and it is during the next 12 to 21 hours that the polar low develops into a tight vortex at the surface.

To get an estimate of the potential influence of diabatic heating through latent heat release some preliminary tests have been made. Diabatic forcing is incorporated in the omega-equation through an additional term on the right hand side of Eq. (5.1.06) giving

$$\nabla^2(q, w^*) + f^2 \frac{\partial^2 w^*}{\partial Z^2} = 2 \nabla \cdot \bar{Q} + \frac{\varepsilon}{\theta_0} \nabla^2 \left( \frac{H \theta}{C_p T} \right) \quad (5.1.10)$$

where  $H$  is the diabatic heating rate.

To get an estimate of  $H$  we assume that the diabatic forcing is controlled by the Ekman-pumping. If  $w_{EGM} \leq 0$  no diabatic forcing is applied. In areas with  $w_{EGM} > 0$  it is assumed that all the water vapour pumped from the PBL into the free atmosphere is condensed within a vertical column heating it. The last assumption is not strictly valid as some of the heat released will be dispersed by gravity waves (e.g. Frank (1983)). Observations at ship AMI, a little to the South East of the polar low at 0000 UTC December 13, show mixing ratios of 2 g/kg increasing to 3 g/kg as the polar low passes later on. A value of 2 g/kg is used here. Over land and/or ice this value may be too large and a land/sea mask is included in the calculation of  $H$  so the mixing ratio can be reduced there.

The vertical distribution of latent heat release in polar lows is not well known. Analysis of an explosively deepening cyclone by Liou and Elsberry (1987) shows that strong diabatic heating at 600 - 700 hPa is of major importance for that development. Though polar lows and the type of cyclone analysed by Liou and Elsberry differ in many ways, we choose a similar distribution with 75% in the 502 - 737 hPa layer and the rest distributed evenly in the remainder of the troposphere, i.e. in the two layers 880 - 737 hPa and 502 - 407 hPa. Further we assume  $H$  is zero over land.

Figure 5.03(2) shows the result. It is seen that the upper part of the ascent region in the polar low has intensified. The region of ascent to the North of the polar low has practically not changed as no diabatic forcing is applied over the ice. Additional tests have been made including diabatic forcing over land. The polar low, situated over water, does not exhibit any changes, whereas the Northern ascent region intensifies with the local diabatic forcing.

Increasing the water vapour content to 3 g/kg yields an increase in the middle and upper part of the polar low updraft. This is seen in Fig. 5.03(3) showing that the solution is rather sensitive to the strength of the diabatic forcing.

Testing different vertical distributions of  $H$  yields only small changes in the updraft associated with the polar low. Generally the updraft intensifies most at the level of maximum heating. This intensification, though, is less pronounced with the maximum in the lowest part of the troposphere.

#### 5.1.4 Concluding remarks

Diagnostic studies of a polar low have been made by a quasi geostrophic and a semi geostrophic version of the omega equation based on an analysis produced by the HIRLAM Base Line model.

In the QGO the thermal forcing dominates the vorticity forcing at upper levels in the vicinity of the low. At this stage of the polar low development the thermal forcing at low levels is not strong. The latter may be due to inadequacies in the treatment of the lowest part of the atmosphere in the analysis used here.

The part which cancels between the ATH and AVO terms can be large and locally exceed the individual terms. This makes the interpretation of the forcing in terms of thermal and vorticity effects uncertain and calls for caution when trying to interpret the ATH and AVO terms as the effect of individual mechanisms.

Application of the SGO yields results which differ from the QGO solution. The SGO produces an updraft which is stronger at lower levels and weaker at upper levels in the polar low region. The difference must primarily be ascribed to the inclusion of ageostrophic horizontal advection in the SGO.

The difference between the Ekman-pumping based on quasi-geostrophic theory and that based on the GMA is negligible in this case. The difference never exceeding the order of  $10^{-4}$ .

The total adiabatic forcing produces only modest ascent in the polar low region. This may, however, be conducive for the organization of the convection and the subsequent development of the polar low.

Diabatic forcing controlled by the Ekman-pumping and the mixing ratio in the PBL intensifies the vertical velocity field in the polar low region. Tests show that the intensification at the polar low is more sensitive to variations in the mixing ratio than the vertical distribution of  $H$ .

The diabatic forcing has a localised effect on the vertical velocity field in the sense that inclusion of diabatic forcing over land affects the field there, but practically not in the polar low region over the sea.

The results obtained by means of the relatively simple omega-equations described above are supplementary to the results which can be obtained by means of a full primitive equations model. It should be remembered, however, that in order to use the diagnostic omega-equations, suitable initial data must be available, and for many purposes these data can only be obtained from a primitive equations model. For this reason (as well as several others) the diagnostic work with the omega-equation models was limited to the experiments discussed above. Further details are given in Pedersen (1988, 1989).

## 5.2 CISK versus "Free Ride"

In a recent paper Fraedrich and McBride (1989) have compared the physical mechanism of the Free Ride balance to that of CISK (Conditional Instability of the Second Kind) as formulated in the two layer model by Charney and Eliassen (1964). From the linear perturbation analyses they conclude that the two assumptions are essentially identical in the region where the Free Ride assumption is valid. The CISK model used in the comparison exhibits a constant growth rate in the limit of small scale perturbations. Further, this growth rate is identical to the one obtained under the Free Ride assumption.

The purpose of this work is to investigate the relation between the Free Ride and CISK assumptions in a more general framework than the Charney and Eliassen (1964) 2-layer model. To this end we will apply analytic models showing that Free Ride and CISK are not identical but that the Free Ride assumption constitute a special case of CISK. In general the solutions have qualitatively different characteristics in the small scale limit. The similarity between the solutions obtained by Fraedrich and McBride (1989) is valid for that specific formulation of the layer model but is not present in general.

As will be seen from the following the CISK growth rate has a short wave cut-off, i.e. the growth rate will approach a value of infinite damping (or amplification) in the small scale limit except for the special case where the heating profile ( $\eta$ ) is required to be unity at the top of the boundary layer. The short wave cut-off in linear CISK have been studied by Chang and Williams (1974) and Pedersen and Rasmussen (1985) where it is shown that the characteristics of the growth rate in a layer model depends on the staggering of variables and equations, and that a CISK model should exhibit a short wave cut-off.

In the Free Ride it is assumed that the thermodynamic equation can be expressed as a balance between the diabatic heating and the adiabatic cooling, i.e. the local change with time of the temperature is assumed to be small compared to those two terms, in convective regions. As we will be looking at linearized models we have ignored the advection term. This balance can be thought of in two ways either as a local constraint (e.g., Chang 1973, Holton 1972) or an integral constraint (e.g. Frank 1980) where the balance is considered for an atmospheric column. The latter interpretation can also be regarded as a necessary (though not sufficient) condition for the local constraint. We will be considering both the local and the integrated Free Ride.

In Section 5.2.1 a general solution to the linearized CISK problem will be presented. In Section 5.2.2 we look at the integrated Free Ride assumption in the context of the CISK solution. Section 5.2.3 contains the comparison of the CISK solution to those of the Free Ride assumptions. Section 5.2.4 compare the local and the integrated Free Ride balance within CISK while Section 5.2.5 gives the conclusions.

### 5.2.1 A general solution to CISK

In this Section we will present a general solution to the linearized CISK problem following a procedure provided by W. H. Schubert (private communication).

As the basic assumptions we apply the quasi-geostrophic approximation on an  $f$ -plane and linearize about a basic state of rest. Under these conditions the vorticity and thermodynamic equations are given by

$$\frac{\partial}{\partial t} \nabla^2 \phi = f^2 \frac{\partial \omega}{\partial p} \quad (5.2.01)$$

$$\frac{\partial}{\partial t} \frac{\partial \phi}{\partial p} + S \omega = -\frac{RQ}{pc_p} \quad (5.2.02)$$

where  $Q$  is the diabatic heating in  $J/(kg \ s)$  and the static stability,  $S$ , is given by

$$S = -\frac{R}{p} \left( \frac{p}{p_0} \right)^{R/c_p} \frac{\partial \bar{\theta}}{\partial p}$$

with the rest of the symbols having their usual meaning. We will in the following assume  $S$  to attain a constant value throughout the atmosphere.

We let the diabatic heating in (5.2.02) be controlled by the Ekman pumping so that all the latent heat which is induced from the boundary layer into the free atmosphere in the form of water vapour is assumed to be liberated within the atmospheric column. Further, we will let the heating be unconditional to facilitate the analytic treatment. This indicates that aside from diabatic heating of the atmosphere over areas with ascent at the top of the Ekman layer a fictitious diabatic cooling is introduced in areas with descent.

Specifying  $Q$  as

$$Q(p) = -Lq_B r(p) \omega_B$$

the requirement that all latent heat is released within the column into which it is pumped gives the following constraint on  $r(p)$  (an as yet unspecified function which describes the vertical distribution of the diabatic heating)

$$\int_0^{p_B} r(p') dp' = 1 \quad (5.2.03)$$

For consistency with the notation of Fraedrich and McBride (1989) we introduce the non-dimensional parameter  $\eta$  defined by

$$\eta(p) = \frac{RLq_B r(p)}{Sc_p p} \quad (5.2.04)$$

so that the thermodynamic Eq. (5.2.02) becomes

$$\frac{\partial}{\partial t} \frac{\partial \phi}{\partial p} + S \omega = S \eta \omega_B \quad (5.2.05)$$

The Ekman pumping is given by

$$\omega_B = -\frac{p_B}{f} K_E \zeta_B \quad (5.2.06)$$

with

$$K_E = \frac{\rho g}{p_B} \sqrt{\frac{Kf}{2}}$$

where  $K$  is the kinematic coefficient of eddy viscosity and  $\zeta_B$  is the geostrophic vorticity.

From (5.2.01) and (5.2.05) we get the  $\omega$ -equation

$$f^2 \frac{\partial^2 \omega}{\partial p^2} + S \nabla^2 \omega = S \eta(p) \nabla^2 \omega_B \quad (5.2.07)$$

Assuming perturbations of the form

$$\omega(x, p, t) = \hat{\omega}(p) e^{i\alpha t} \cos\left(\frac{2\pi}{l} x\right)$$

and letting

$$\kappa^2 = \frac{S}{f^2} \left( \frac{2\pi}{l} \right)^2 \quad (5.2.08)$$

we get the general solution for the growth rate in linear CISK models

$$\sigma_{CI} = -\frac{p_B K_E \kappa}{\sinh(\kappa p_B)} + p_B K_E \kappa^2 \int_0^{p_s} \frac{\sinh(\kappa p')}{\sinh(\kappa p_B)} (\eta(p') - 1) dp' \quad (5.2.09)$$

It is seen that the second term on the right hand side of (5.2.09) is responsible for the short wave cut-off in the growth rate, the term essentially being proportional to  $\kappa$  given by (5.2.08). It is also seen that the cut-off can turn into a blow-up depending on the structure of  $\eta(p)$  as noted by Pedersen and Rasmussen (1985).

### 5.2.2 CISK and integrated Free Ride

To look at the integrated Free Ride assumption in connection with CISK we consider the integrated form of the thermodynamic Eq. (5.2.05)

$$\frac{1}{S \omega_B} \int_0^{p_s} \underbrace{\sigma \frac{d\phi}{dp'}}_A dp' + \int_0^{p_s} \underbrace{\frac{\omega}{\omega_B}}_B dp' = \int_0^{p_s} \underbrace{\eta(p')}_C dp' \quad (5.2.10)$$

and the Free Ride assumption says that the term A is small compared to B and C, i.e.

$$\int_0^{p_s} \frac{\omega}{\omega_B} dp' \sim \int_0^{p_s} \eta(p') dp' \quad (5.2.11)$$

In this section we will study how the general solution obtained in the previous section relates to this assumption.

For the term A we get

$$\begin{aligned} A: & \frac{1}{\kappa} \left\{ \frac{1}{\sinh(\kappa p_B)} - \frac{1}{\tanh(\kappa p_B)} \right\} + \\ & \frac{E}{\kappa^2 + (\pi(p_1 - p_s))^2} \left\{ \kappa \left( \frac{1}{\tanh(\kappa p_B)} - \frac{1}{\sinh(\kappa p_B)} \right) \sin \left( \frac{p_1 - p_B}{p_1 - p_s} \pi \right) + \right. \\ & \left. \frac{\pi}{p_1 - p_s} \left( \cos \left( \frac{p_1 - p_B}{p_1 - p_s} \pi \right) + \frac{\sinh(\kappa p_s)}{\sinh(\kappa p_B)} + \frac{\sinh(\kappa(p_B - p_s))}{\sinh(\kappa p_B)} \right) \right\} \end{aligned} \quad (5.2.12)$$

We cannot, however, determine the relation between the terms A, B and C in (5.2.10) without specifying the heating profile  $\eta(p)$ . So as to evaluate the Free Ride assumption for the CISK solution we will specify  $\eta(p)$  as

$$\eta(p) = \begin{cases} E \sin\left(\frac{p_1 - p}{p_1 - p_*} \pi\right) & ; p_B \geq p \geq p_* \\ 0 & ; p_* \geq p \geq 0 \end{cases} \quad (5.2.13)$$

where  $p_1 \geq p_B$  and  $p_*$  is a level above which no diabatic heating takes place. From (5.2.04) and (5.2.05) we get

$$E = \frac{RLq_B}{Sc_p} \left( \left( \frac{p_1 - p_*}{\pi} \right)^2 \sin\left(\frac{p_1 - p_B}{p_1 - p_*} \pi\right) + \frac{p_1 - p_*}{\pi} \left( p_B \cos\left(\frac{p_1 - p_B}{p_1 - p_*} \pi\right) + p_* \right) \right)^{-1}$$

while (5.2.11) and (5.2.13) yields

$$C: E \left( \frac{\pi}{p_1 - p_*} \right)^{-1} \left( \cos\left(\frac{p_1 - p_B}{p_1 - p_*} \pi\right) + 1 \right) \quad (5.2.14)$$

In the small scale limit ( $l \rightarrow 0$ ) we have from (5.2.08) that  $\kappa \rightarrow \infty$ . Application of this in (5.2.12) gives

$$\lim_{\kappa \rightarrow \infty} A = 0 \quad (5.2.15)$$

where as (5.2.14) shows that the C term for a given heating profile and  $q_B$  is constant (independent of  $\kappa$ ). This shows that the CISK assumption with the  $\eta$ -profile (5.2.13) satisfy the integrated Free Ride assumption in the small scale limit ( $|A| \ll C$ ). We believe this to be a general result.

Figure 5.04 shows a comparison of the terms A, B and C as a function of the perturbation wave length. For the data used (see the figure legend) the magnitude of A does not exceed 7% of that of C for perturbation wave lengths smaller than the Rossby deformation radius ( $R_d = (p_B - p_*)\sqrt{S/f}$ ) showing that the CISK assumption for this heating profile satisfy the integrated Free Ride assumption not only in the small scale limit but also for perturbation scales up to  $R_d$ . It should be noted that the magnitude of A depends on  $\eta$  and other  $\eta$ -profiles can give larger values for the A/C-ratio at  $R_d$  while the term A still adhere to (5.2.15).

### 5.2.3 Free Ride and CISK

In the previous section it is shown that the CISK assumption fulfils the Free Ride assumption in the small scale limit. In this section we will study whether the opposite also holds, i.e. does the Free Ride assumption lead to the same solution as the CISK assumption. For this purpose we will employ the same  $\eta$ -profile as in Section 5.2.2.



### 5.2.3.1 Integrated Free Ride

From (5.2.01) we get

$$\omega = -\left(\frac{2\pi}{l}\right)^2 \frac{\sigma}{f^2} \int_0^p \phi(p') dp',$$

whereby the Free Ride assumption (5.2.11) together with (5.2.06) becomes

$$\sigma_{FR1} \int_0^{p_B} \int_0^{p'} \phi(p'') dp'' dp' + p_B K_E \phi_B \int_0^{p_B} \eta(p') dp' = 0 \quad (5.2.16)$$

A solution is given by

$$A \sin\left(\frac{p_1 - p}{p_1 - p_*} \pi\right) + B \cos\left(\frac{p_1 - p}{p_1 - p_*} \pi\right) \quad ; \quad p_B \geq p \geq p_*$$

$$\phi_{FR1}(p) = \quad (5.2.17)$$

$$C \cosh(ap) \quad ; \quad p_* \geq p \geq 0$$

where  $a$  is a scaling factor used to facilitate the numerical evaluation of the terms. Even though this is a solution for (5.2.16) with the heating profile used it is not evident that it is a unique solution. However, as (5.2.17) becomes identical to the "local Free Ride" solution if we impose the constraint  $\eta(p_B) = 1$  (see Section 5.2.3.2) it is a consistent choice.

Imposing the constraint that  $\phi$  must be continuous at  $p_*$ ; The vertical derivative of  $\phi$  must be continuous at  $p_*$  and the vertical derivative of  $\phi$  must vanish at  $p = 0$  the growth rate follows from the (5.2.16) and (5.2.17)

$$\begin{aligned} \sigma_{FR1} = & -E p_B K_E \phi_B \left(\frac{\pi}{p_1 - p_*}\right)^{-1} \left(\cos\left(\frac{p_1 - p_B}{p_1 - p_*} \pi\right) + 1\right) \\ & \left\{ \frac{C}{a} \left( \frac{\cosh(ap_*) - 1}{a} + (p_B - p_*) \sinh(ap_*) \right) + \right. \\ & A \left(\frac{\pi}{p_1 - p_*}\right)^{-1} \left( p_B - p_* - \left(\frac{\pi}{p_1 - p_*}\right)^{-1} \sin\left(\frac{p_1 - p_B}{p_1 - p_*} \pi\right) \right) - \\ & \left. B \left(\frac{\pi}{p_1 - p_*}\right)^{-2} \left(\cos\left(\frac{p_1 - p_B}{p_1 - p_*} \pi\right) + 1\right) \right\}^{-1} \end{aligned} \quad (5.2.18)$$

showing that the integrated Free Ride growth rate is independent of  $\kappa$ , i.e. scale independent in agreement with the result obtained by Fraedrich and McBride (1989).

For comparison with (5.2.18) we present the corresponding expression for the CISK solution.

$$\sigma_{CI} = -p_B K_E \kappa \left\{ \frac{1}{\tanh(\kappa p_B)} - \frac{\kappa^2}{\kappa^2 + (\pi/(p_1 - p_*))^2 \tanh(\kappa p_B)} - \frac{\eta(p_B)}{\kappa^2 + (\pi/(p_1 - p_*))^2 p_1 - p_*} \left( \cos\left(\frac{p_1 - p_B}{p_1 - p_*} \pi\right) + \frac{\sinh(\kappa p_*)}{\sinh(\kappa p_B)} \right) \right\} \quad (5.2.19)$$

Figure 5.05 show the growth rate for the integrated Free Ride and the CISK solutions when the heating profile (5.2.13) is used together with the parameters cited in the legend of Figure 5.04. The short wave cut-off is evident for the CISK solution which has the largest growth rate for perturbations with a scale comparable to the Rossby deformation radius.

It is apparent from the figure (as well as the equations presented above) that the integrated Free Ride and CISK solutions differ both qualitatively and quantitatively.

### 5.2.3.2 Local Free Ride

Until now we have interpreted the Free Ride assumption as an integral constraint. As mentioned in the introduction in applications of the Free Ride the balance between the diabatic heating and adiabatic cooling have also been applied locally. In this case the Free Ride assumption yields

$$\omega(p) = \eta(p) \omega_B \quad (5.2.20)$$

where by the function  $\eta$  describes the vertical  $\omega$ -profile.

From (5.2.20) we get the constraint

$$\eta(p_B) = E \sin\left(\frac{p_1 - p_B}{p_1 - p_*} \pi\right) = 1 \quad (5.2.21)$$

on  $\eta$  which together with (5.2.03) yields a constraint on  $p_1$ .

For simplicity we let  $p_* = 0$  in (5.2.13) and then get the growth rate

$$\sigma_{FR, \kappa} = p_B K_E E \frac{\pi}{p_1} \cos\left(\frac{p_1 - p_B}{p_1} \pi\right)$$

The solution (5.2.17) collapses to the same solution for  $p_* = 0$ , i.e. the local and integrated Free Ride becomes identical when the constraint (5.2.21) is applied.

Figure 5.06 shows the growth rates in this case and we note that the CISK solution has lost the cut-off, actually having the same growth rate in the small scale limit as the Free Ride. From (5.2.19) we see that in the small scale limit ( $\kappa \rightarrow \infty$ ) the first two terms on the right hand side cancel as  $\eta(p_B) = 1$ . The last term ( $p_* = 0$ ) becomes

$$\lim_{\kappa \rightarrow \infty} \sigma_{CI} = p_B K_E E \frac{\pi}{p_1} \cos\left(\frac{p_1 - p_B}{p_1} \pi\right) \quad (5.2.22)$$

Thus in the special case of  $\eta(p_B) = 1$  the CISK solution "degenerate" into something that is comparable to the Free Ride in the small scale limit - for all other values of  $\eta(p_B)$  the CISK solution will have either a cut-off or a blow-up of the growth rate in the small scale limit.

#### 5.2.4 Local and integrated balance in CISK

Since the solution for the CISK assumption approach that of the Free Ride in the small scale limit if we impose the constraint  $\eta(p_B) = 1$  it is of interest to see how well the local balance is fulfilled for the CISK solution. From Section 3 we have the thermodynamic equation given as

$$\underbrace{-\frac{1}{\kappa^2} \frac{d^2 \omega / \omega_B}{dp^2}}_A + \underbrace{\frac{\omega}{\omega_B}}_B = \underbrace{\eta(p)}_C \quad (5.2.23)$$

and we will look at the ratio  $A/C$  as a measure of the error in assuming the local balance. In Fig. 5.07  $|A/C|$  is expressed in % (the ratio is set to zero at  $p = 0$  hPa since  $\eta(0) = 0$ ) and it is seen that the adherence of the CISK solution to the local balance is within an order of magnitude for nearly all perturbations smaller than  $R_d$ .

Next we turn to the more general CISK solution, i.e. we do not require  $\eta(p_B) = 1$ , and Fig. 5.08a shows  $|A/C|$  for the example considered in Section 5.2.3.1 (again we have set the ratio to zero when  $\eta(p) = 0$ ). We note that the local balance breaks down severely at the top and bottom of the diabatic heating region. This is partly due to the fact that  $\eta(p)$  becomes zero at these boundaries.

If we extend the diabatic heating region to the top of the atmosphere as in the study of the local balance in Section 5.2.3.2 we see that the  $|A/C|$  - ratio (see Fig. 5.08b) resembles Fig. 5.07 remarkably well except in the lowest 1 to 2 hundred hPa where the local balance breaks down. This feature has a striking resemblance to the results obtained by Fingerhut (1978) who gets an  $|A/C|$  - ratio (from his Table 2) of 1600 % at the 876 hPa level! Further, the relative distribution of  $A$  (see Fig. 5.09) is in agreement with his results showing fairly large negative values at the bottom (since we have  $\eta(p_B) = 0$  we get  $A(p_B) = -1$  from (5.2.23)) with smaller positive values higher up in the atmosphere resulting in the overall small value of the integrated  $A$  - term (ref. Fig. 5.04).

So the general CISK solution not only adhere to the integrated Free Ride but also to the local Free Ride in the major part of the atmosphere for perturbation scales smaller than  $R_d$ . Further, the region where the CISK solution deviates significantly from the local balance coincides with the region where diagnostic studies based on observations indicates a break down of the assumption of a local balance.

### 5.2.5 Conclusions

A general analytic solution to the linearized CISK problem has been presented showing the scale dependence of the growth rate, specifically that a cut-off/blow-up takes place in the small scale limit in general.

With application of a specific heating profile the CISK assumption yields a solution which also satisfy the integrated Free Ride assumption for perturbation scales up to the Rossby deformation radius. We believe this to be a general result in the small scale limit where as the A/C ratio in (5.2.10) for perturbation scales near  $R_d$  may be larger depending on the specific heating profile  $\eta$ .

The solution to the Free Ride assumption in an analytic model exhibit a growth rate that is scale independent whether we interpret the Free Ride as an integral constraint or a local balance. The latter yields the constraint  $\eta(p_B) = 1$  and for this special case the integrated and local Free Ride becomes identical. Further, the CISK solution becomes identical to this 'unified' Free Ride solution in the small scale limit.

From the above we conclude with respect to the small scale limit that:

- I) If interpreted as a local balance which essentially fixes the vertical  $\omega$ -profile the Free Ride is a subset of CISK (specified as solutions which satisfy  $\eta(p_B) = 1$ ).
- II) If interpreted as an integral constraint (not requiring  $\eta(p_B) = 1$ ) the Free Ride differ qualitatively from the CISK solution even though the latter does exhibit a balance between the diabatic heating and adiabatic cooling for an atmospheric column.
- III) The CISK solution adhere to the integrated Free Ride in general and the local balance for the major part of the atmosphere for perturbation scales smaller than the Rossby deformation radius. That the local balance breaks down in the lowest part of the atmosphere appears to be in accordance with the results obtained by Fingerhut (1978).

II) indicate that the specification of the integral constraint alone is not sufficient to determine a unique solution and I) and III) that the constraint  $\eta(p_B) = 1$  is not necessary to obtain the basic balance of the local Free Ride assumption - keeping in mind that diagnostics based on observations indicate that the local balance is not fulfilled at the lowest levels of the atmosphere.

### 5.3 Numerical modelling studies

In this Section we describe the work done with two primitive equation models during the project. The HIRLAM model has been used primarily to obtain data for an IPV analysis and initial data for the RAMS model through a 4-dimensional data assimilation. The RAMS model has been used to simulate the December 13 - 14, 1982 Bear Island development described in Section 4.

### 5.3.1 The HIRLAM model

To obtain an objective 4-dimensional data set describing the development of the 1982 Bear Island polar low episode we have performed a data assimilation using the HIRLAM (High Resolution Limited Area Model) Level I. A complete description of the model system which is the result of a joint Nordic / Dutch project is given in Machenhauer (1988) and here we will only comment on aspects directly connected with the data assimilation.

Figure 5.10 shows the geographical extend of the domain which have 92 grid points in the East-West direction and 85 in the North-South direction. A rotated latitude-longitude grid is applied having grid distance of 0.5 degrees. In the vertical 16 levels are used and convection is parameterized using a Kuo type scheme.

As initial and boundary data for the model we use initialized analysis fields from the ECMWF (European Center for Medium range Weather Forecasts) model.

In the HIRLAM model the surface temperature on solid surfaces (land and ice) is a predicted quantity whereas climatological values are used for the sea surface temperature. This presents a problem as both the observed sea surface temperature and sea-ice extend deviated significantly from the climatological values in December 1982. To avoid starting the data assimilation with erroneous surface fluxes which may be crucial for the development of polar lows, the sea surface temperature and the sea-ice extent was subjectively analysed from maps produced by the Norwegian Meteorological Institute and the US Navy and substituted in the climatology file for the HIRLAM model.

#### 5.3.1.1 Data assimilation

The data assimilation was started at 00 UTC on December 9, 1982 as a "cold start" from the ECMWF analysis and ran until 00 UTC on December 14, 1982.

The data assimilation cycle was 6 hours and performed in the following way. Starting out with a first guess field (initially an ECMWF analysis) all available observations in the ECMWF archive were used as input to the analysis model. The observations include ordinary surface observations, ships, bouys, radio soundings, pilots, satem and air-reps.

The analysis model then adjust the first guess field towards the observation producing an uninitialized analysis. This in turn is initialized using a normal mode procedure to obtain a more balanced field. With this initialized analysis as input the forecast model is run for 6 hours producing a new first guess field - after which a new cycle can begin.

Figure 5.11 shows the uninitialized analysis valid at 00 UTC December 14 and Fig. 4.05 the corresponding subjective analysis. It is evident that the HIRLAM data assimilation system was not able to analyse the relatively small-scale polar low.

Figure 5.12 shows a comparison of the analysed MSL pressure with observations at 00 UTC December 13 ~~before~~ the formation of the polar low. At this time we see a quite good agreement between the model and the subjective analysis. In the following analyses the trough is filled somewhat in connection with the

North-Eastward movement of the synoptic low South-Southeast of Novaya Zemlaya. Observations, on the other hand, show a general but small pressure drop in the region of interest.

To get a more direct comparison between the MSL pressure predicted by the model and observations, Fig. 5.13 shows time series for the four stations indicated on Fig. 5.12. In general - if we exclude AMI for the moment - the analyses are within 1 hPa of the observations. Only the North-Eastward moving trough connected with the major low near Novaya Zemlaya is not deep enough at Hopen, and at 18 UTC December 12 there is a slight miss at North Kvaloy. Concerning AMI it is evident that the model misses the development altogether, and the predicted and observed values start to deviate significantly already early on December 13.

If we look at the low level wind field as indicated by the cloud streets on the satellite image from December 12 (Fig. 4.03) we have a Northerly flow over the sea East of Greenland and an Easterly flow on the West side of Svalbard. South-East of Svalbard the flow is North-Easterly. For comparison the wind field on the 965 hPa surface in the corresponding analysis is given in Fig. 5.14 showing that the structure of the flow is represented quite well.

There is, however, a marked difference between the analysis and the observations when we consider the temperature field at low levels (not shown). The air coming out over the sea from the ice-pack is several degrees warmer than the observed temperature. For instance at Hopen the model temperature is some 5 K too high. It seems to be a general problem throughout the data assimilation that the model gives too high temperatures over the sea-ice.

If we look at the 500 hPa level a cold low is situated East of Svalbard at 12 UTC December 12 (Fig. 5.15). This low moves to the South-Southwest filling a little while the  $-44^{\circ}\text{C}$  region expands somewhat. Only at the end of the period does the temperature rise again. For comparison with observations Fig. 5.16 shows time series of the 500 hPa height for the three stations indicated on Fig. 5.15. Up to 12 UTC December 13 the analysed heights are within 2 dm of the observed values. The temperature at 500 hPa corresponds to within 1 K with the observations throughout the 48 hour period considered here.

Comparing the vertical temperature profile in the model with the observation at Bear Island at 12 UTC December 12 shows significant differences (Fig. 5.17). The stability differs with the model being too warm in the 350 - 750 hPa layer and too cold in the 850 hPa region. Looking at the winds it is quite obvious that the assimilation deviates from the observations. According to the subjective analysis (Fig. 5.18) a cold low is situated West of Bear Island. Figure 5.19 shows the 500 to 1000 hPa thickness field from the assimilation with wind arrows representing the observed 500 to 1000 hPa thermal wind. It is apparent that the assimilation has not captured the cold low West of Bear Island having more of a thermal ridge in that region. As the observed low moves Southward during the next 24 hours the assimilation instead exhibits a large scale thermal trough South West of Svalbard (Fig. 5.20).

From the above we conclude that the assimilation model yields a good analysis when we consider the synoptic scales but misses the important mesoscale upper level cold low West.

The analysis model does not reject the observations from AMI during the assimilation. However, as the analysis scheme has a build in confidence in the first guess field it is not capable of making the more than 10 hPa adjustment as required near AMI at 00 UTC December 14. The difference between the first guess field and the uninitialized analysis amount therefore only to about 1.5 hPa in this case.

Figure 5.21a shows the 6 hour prognosis of the 1000 hPa geopotential height and temperature field which was part of the first guess for the analysis shown in Fig. 5.11. Comparison of the two figures together with the observations in Fig. 4.05, which were included in the analysis, highlights the confidence of the analysis scheme in the first guess field in data sparse regions.

The fact that the first guess field is so far off (compare Figs. 4.05 and 5.21a) shows that the forecast model has some problems handling this development. To study this a little closer we look at the behaviour of the model during the first 6 - 12 hours of the convective phase of the development.

Figure 5.21b shows the 6 hour pressure tendency between 18 UTC December 13 and 00 UTC December 14. The large pressure tendencies near Novaya Zemlaya are associated with the synoptic scale low travelling East. More interesting from our point of view is the region with fairly large pressure falls of up to 2.5 hPa to the West of Bear Island where moderate pressure rises were simulated during the previous 6 hour period. The region is situated a little North-West of where the observed polar low developed indicating that the model experiences some cyclogenesis in the area of interest.

During the period from 12 UTC December 13 to 00 UTC December 14 the upper level cold low moves towards South-West passing the ice edge near Bear Island around 18 UTC. This triggers the Kuo scheme in the model producing a 6 hour accumulated convective precipitation in the region of pressure falls (Fig. 5.22) which is more than double the amount during the previous 6 hour period. Also in the following hours when the upper low moves towards the South-West the convective scheme keeps triggering convection in the same place just off the ice edge, whereas only little convection triggered below the upper low.

According to the observations the formation of the intense polar low at the surface took place around midnight between December 13 and 14, 1982. The HIRLAM model, however, for some reason was not able to handle this part of the development, but blew up during the assimilation cycle from 00 UTC to 06 UTC December 14. This numerical breakdown has not been investigated further.

### 5.3.1.2 IPV analysis

The polar low development which culminated early on December 14, 1982 was associated with an upper level low which moved Southward from Svalbard out over the ice border (see Section 4.1 and Fig. 5.18). In many cases the quasi-geostrophic omega-equation has proved to be a useful tool for understanding some phases/aspects of polar low developments as for example the role of initial baroclinic forcing through differential vorticity advection. However, a reliable, detailed analysis of the development by means of the omega-equation was not possible in this case, because of the small scales involved and the lack of data on these scales.

An alternative way to understand the dynamics of the developing polar low which partly overcome the difficulties mentioned above, is to apply the idea of potential vorticity (Kleinschmidt, 1957 and Hoskins et al., 1985). As pointed out by Reed (1991) the paper by Hoskins et al. (1985) "has stimulated widespread interest lately in "IPV thinking" and has lead to its application in diagnostic studies of observed cases of cyclogenesis". In the following we will show that prior to the surface development of polar low "A" an upper-level IPV anomaly of fairly large horizontal scale and of substantial magnitude can be observed to have advanced into the region. The development started when the upper level IPV anomaly became superimposed upon the surface "surrogate PV" (Reed, 1991) connected with surface baroclinicity along the ice-edge region and the region of strong sensible/latent heating South of Bear Island.

The use of the IPV-concept highlights the importance of the "solitary" upper-level disturbance and its associated vertical motion field which resulted in the cloud spiral seen on Fig. 4.04 at a time when neither observations nor model simulations showed any significant surface development.

In this section we will study this (baroclinic) part of the development in the light of an IPV (Isentropic Potential Vorticity) analysis. As the upper level disturbance had a horizontal scale of only a few hundred kilometers this important feature was not correctly analyzed during the assimilation, which affected the subsequent analysis to some degree (See Section 5.3.1.1). Therefore, although we feel very confident in the analysis on a scale somewhat larger than the upper level disturbance certain discrepancies between the simulation and the observations should be expected on the (small) subsynoptic scale. Especially the model must be expected to underestimate the strength of the IPV-anomalies and, to some extent, to displace the centers of the anomalies relative to the observed positions.

The IPV diagnosis Figure 5.23 shows the 290 K IPV fields in PV units (see Hoskins et al. 1985) over a 36 hour period. The 290 K isentropic surface is situated near the tropopause level (around 350 hPa) in the Svalbard region during this period. The large positive IPV anomaly, 3 to 4 PV units, initially situated East and North-East of Svalbard at 0000 UTC December 12, 1982 is seen to expand horizontally while it moves Southward during the next 36 hours. The IPV anomaly develops two local maxima during the period with one taking a Southerly course towards Bear Island where it triggers the polar low development. The other maximum which follows a track North and West of Svalbard does not give rise to any development, a point we will return to later. The contrasts around Svalbard between the open and partly or wholly ice covered sea produce a sharp but shallow baroclinic zone near the ice-edge. Fig. 5.24 shows the temperature at the 995 hPa surface. The shallow baroclinic zone associated with the ice-boundary shows up clearly, stretching from Greenland to the North-Western Svalbard and from Svalbard towards Bear Island and Eastwards.

The track of the Eastern of the two anomalies (EA) passes the baroclinic zone a little Southeast of Svalbard. This scenario bears a great resemblance to the "cyclogenesis thought experiment" of Hoskins et al. 1985 in their Section 6e. Following Hoskins et al. we can describe the dynamics of the first part of the development as follows: The Eastern center, EA, of the upper level positive IPV anomaly moves Southwards from the Svalbard region towards the ice-edge and the associated low level baroclinic zone. The low level cyclonic circulation induced by the IPV anomaly induces a wave in the baroclinic field, which then constitutes



a low level IPV anomaly. This low level IPV in turn induces its own cyclonic circulation (ref. Fig. 21, in Hoskins et al., 1985). The cyclonic flows induced by the upper and lower IPV anomaly will reinforce each other and start a spin-up process. This spin-up process, however, will only be possible if the cyclonic flow induced by the upper level IPV anomaly can penetrate sufficiently deep down into the troposphere. The vertical scale for this penetration is the Rossby height (ref. Hoskins et al., 1985) defined by

$$H = \frac{fL}{N}$$

In our case the value of the Rossby height in the vicinity of the IPV anomaly is around 5 km (for a horizontal scale of the flow,  $L = 500$  km) throughout the period of interest, showing the potential for the upper level IPV anomaly to interact and participate in a spin-up process.

Reed (1991) in his discussion of a case of explosive cyclogenesis points out how a positive "surrogate" IPV anomaly conducive to the production of low pressure was created near the low center by a Northward advance of a tongue of warm air (a positive surface potential temperature anomaly may, according to Bretherton (1966), be regarded as a "surrogate" potential vorticity anomaly). In Reed's case the anomaly was entirely produced by temperature advection, and air-sea interaction made no contribution to the formation of the anomaly. In the present case both advection as well as surface heat transfer from the relatively warm sea surface South of Bear Island are bound to be important.

Upper-air IPV anomalies moving relative to the lower layers are characterized by ascent and vortex stretching ahead of the anomaly, and descent and vortex shrinking behind (Hoskins et al., 1985). In our case the upper-level IPV anomaly can be observed through the formation of the very noticeable cloud spiral (Fig. 4.04), before any significant development can be observed at the surface. Although baroclinic processes play an important role for the development, the cloud field in this case is strikingly different from that normally corresponding to a small baroclinic wave.

As mentioned earlier and shown on Figs. 5.23 actually two IPV maxima (EA and WA) moved out over the (warm) sea, but only EA resulted in a polar low development. The Western anomaly, WA, passed North, then West of Svalbard (Fig. 5.23d). WA did not, however, initiate any significant low-level disturbances as it entered the region free of ice between Svalbard and the Northeastern part of Greenland. The sea surface temperature in this region is fairly low and, as seen from Fig. 4.03, shallow and very cold air masses, originating from the surrounding ice/snow covered regions, completely covered the region down to about 70 N. There was therefore virtually no possibility in this environment for the establishment of a low-level IPV anomaly which could have led to a development corresponding to that observed further East. On the other hand low-level baroclinic systems sometimes do form in the "triangle" formed by Svalbard, Northeast Greenland and 70 N. Such developments may occur in the low-level baroclinic zone situated at the ice edge at the coast of Northeast Greenland, as well as further East nearer to Svalbard. However, these developments are relatively rare and almost never result in the formation of significant polar lows.

The reduced stability beneath the upper level IPV anomaly facilitates convection and if the air is moist enough the associated latent heat release will act to redistribute the potential vorticity in the vertical. Above the region of maximum heating the potential vorticity will be diminished whereas it will be increased below. This redistribution, of course, is important for the dynamics of the ensuing development. However, since this "convective" part of the development following the initial baroclinic phase is not satisfactorily reproduced in our numerical simulation we will not go further into this problem. (For a general discussion see Hoskins et al., 1985 and Nordeng and Rasmussen, 1992).

As a result of the baroclinic development described a (surface) low of moderate intensity (polar low "A") was formed between Bear Island and Northern Norway with a central pressure around 990 hPa (see R85 Fig. 7). The horizontal scale of the low was around 500km corresponding to the local Rossby deformation radius.

### 5.3.2 The RAMS model

In this Section we will describe the results obtained using the Colorado State University Regional Atmospheric Modelling System (RAMS) which kindly has been made available by Professors Cotton and Pielke<sup>1</sup>. A detailed description of the entire model system will not be attempted here, but the specific modifications made to the model for application in polar regions will be mentioned.

The basic 3-dimensional non-hydrostatic cloud / mesoscale model is described by Tripoli and Cotton (1982) and Tripoli (1986). It is a grid point model using a sigma-z coordinate in the vertical with the option of using in principle an unlimited number of nested grids. The grid nesting is two-way interactive so that developments taking place in a nested grid is communicated back to the coarser grid.

Diffusion is parameterized using deformation and stability dependent exchange coefficients in a first order eddy viscosity approach (Tremback, 1990).

As the top boundary condition a lid is used and at the lateral boundaries the Klemp and Wilhelmson (1978) radiative boundary condition is applied.

Radiative processes are parameterized as given by Chen and Cotton (1983). This parameterization includes long and short wave radiation though the latter is of little importance for the runs referred to here due to the polar night. The scheme takes the effect of condensate into account aside from water vapour, ozone and carbon dioxide.

Convection is represented either in parameterized form or is given explicitly depending on grid spacing and / or options chosen. The parameterized form is a modified Kuo - type given by Tremback (1990). The version used here does not differ from Tremback (1990) except for the adjustment to an arctic environment of parameters related specifically to convection over the central US. The convection is treated explicitly when the grid spacing is small enough and the RAMS cloud microphysics module (Flatau et al., 1989) is employed. When the cloud microphysics is activated in general only pristine ice crystals and aggregates are considered as the atmosphere is too cold or the vertical velocities too small for

---

<sup>1</sup> During a 9 month stay at CSU by the second author.

"wet" hydrometeors like rain or hail to occur during the simulations. To specify the slope of the Gamma distribution assumed for aggregates values are taken from Kikuchi et al. (1982).

The lower boundary of the model is divided into three classes: Land, sea and sea-ice with a given fraction of each grid box being sea and the remainder either land or sea-ice. Temperature and humidity are forecasted for land areas following Tremback and Kessler (1985) and for sea-ice as described below. In open sea areas the temperature is held constant. Surface layer fluxes are parameterized after Louis (1979).

Experience with the HIRLAM model (see Section 5.3.1) showed that application of a soil model to simulate conditions over sea-ice is problematic so it was decided to implement a sea-ice model in the RAMS to avoid that problem. The aim has not been to forecast changes in the sea-ice thickness or extent but to obtain more realistic temperature conditions over the sea-ice. The model implemented follows in general Semtner (1976) with a 2-layer sea-ice model with a snow layer on top. The temperature profile within the snow and ice is determined applying a one-dimensional heat equation with separate heat conduction and specific capacity applied for the two constituents. At the lower boundary the temperature is held fixed at the melting point while an energy balance is used at the upper boundary. The energy balance is made up of the contributions from the heat flux coming up through the snow, the radiative surface fluxes (again the short wave contribution is negligible due to the polar night) and the sensible and latent heat fluxes. The balance is solved by iteration and convergence is fast.

As the RAMS could be run either in a latitude / longitude or plain cartesian grid and neither of these was amenable to represent large regions near the pole, the model was reformulated to apply a generalized polar stereographic projection. The generalized projection being defined as a normal polar stereographic projection with the projection plane being tangent to the Earth with the contact point at the center of the model domain.

#### 5.3.2.1 Simulation of the December 13 - 14, 1982 Bear Island case

For this simulation we applied two grids nested inside the coarsest grid. The base grid (grid 1) having 51 by 51 grid points horizontally with a grid distance of 50 km. In the vertical we have 30 levels in all three grids reaching about 80 hPa. Inside grid 1 we have a nested grid (grid 2) with a 50 by 50 point horizontal grid. The nest ratio is 2, i.e. the grid distance is half that of grid 1. Grid 3 is nested inside grid 2 also with a nest ratio of 2 in the horizontal having 60 by 60 points in the horizontal. Figure 5.25 shows the geographical extent and position of the three grids.

The initial data valid at 12 UTC December 13, 1982 are taken from the HIRLAM data assimilation interpolated to the RAMS grid number 1 (see Fig. 5.26). This grid is then run for 2 hours. Following this the two nested grids are turned on together with the microphysics. The Kuo - type parameterization is used on grid 1 and 2 but not on grid 3 having a grid distance of 12.5 km.

The MSL pressure after 12 hours of integration is shown in Fig. 5.27 for all three grids evidencing the efficiency of the two-way nesting. We note that a pressure drop of up to 5 hPa has taken place in the region of interest and a 989 hPa low is situated a little North East of the actual development (ref. polar low A in Fig. 4.05). The pressure field shown in Fig. 5.27 represents fairly well the surface pressure prior to the convective development. The reason for the discrepancy between the model runs and the observed fields is partly connected to the problem of a correct representation of the convection and partly to the problem of representing small scale phenomena in the models.

As shown in Section 4 convection becomes a dominant feature during the final deepening stage of the polar low. However, as evident from Fig. 5.28 the convective parameterization is only triggered in the trough region along the West coast of Northern Norway (see Fig. 5.27a) whereas no convection takes place in the region of the polar low. This result also holds for grid 2.

Figure 5.29 shows the lifting condensation level (LCL) for air at the lowest model level after 12 hours integration. Over the sea areas this level is rather constantly located about 600 m. Over the Norwegian mountains, Svalbard and North East Greenland at the upper left corner the level is situated somewhat higher due to the elevated terrain. Thus the low level air is fairly humid. Figure 5.30 shows the depth of the layer between the LCL and the equilibrium temperature level (ETL) for a moist parcel ascending from the LCL. This measure of the potential for convection exhibit a maximum depth of 3600 - 3800 m in the trough region immediately West of the Norwegian coast, whereas the depth is less than half that in the remaining part of the domain. Thus any convection away from the trough region will be fairly shallow.

In order that the convective parameterization can be triggered in the model the available buoyant energy (ABE) must be positive. The available buoyant energy is represented as the difference between the virtual potential temperature of a moist parcel ascent and the environment divided by the environment virtual potential temperature integrated in the vertical from the LCL to the ETL. Figure 5.31 show the ABE and it is seen that only in the trough region West of Northern Norway do we have significant positive ABE values where as we have small negative values in the polar low region. So even though the LCL - ETL depth (Fig. 5.30) shows the potential for shallow convection, this cannot be realised due to the low ABE values away from the trough region West of Northern Norway.

If we look at the resolved precipitation defined as precipitation released through the microphysical processes (Fig. 5.32a) we note that the highest precipitation amounts are again associated with the trough region West of Northern Norway. Further, we see general precipitation over the open sea with local maxima between Svalbard and Northeast Greenland and along the sea-ice border Southeast of Svalbard. In grid 3 we see the same result with maximum precipitation at the sea-ice boundary Southeast of Svalbard and light precipitation elsewhere (Fig. 5.32b). Comparing Fig. 5.32a and Fig. 5.33 we see that the major part of the precipitation is in the form of aggregates, i.e. hydrometeors generated by collection amongst pristine ice-crystals. Taking the ABE result into account it is not surprising that the resolved microphysics, e.g. in grid 3, do not give rise to the simulation of deep convection.

Comparison of a model sounding with that from Bear Island at 00 UTC December 14, 1982 (Fig. 5.34) shows that deep convection (through the entire troposphere) actually is possible if the surface air gets a relatively small boost of latent and sensible heat from the sea surface. Note that Bear Island and the corresponding model sounding is situated within the sea-ice near the ice-edge why the inversion is sharper here than over the open sea, however, the boundary layer is still capped by a relatively strong inversion over the open sea. Figure 5.35 shows that the surface flux of sensible heat over the open sea attains values of 20 to 60 W/m<sup>2</sup> in general and locally values of 100 to 160 W/m<sup>2</sup> are found. For the latent heat flux (Fig. 5.36) the values over the open sea typically lies in the 20 to 40 W/m<sup>2</sup> range. These values are much lower than expected from bulk formula computation based on observations, and also appear low compared with measurements during cold air out-breaks over the Atlantic from the North American continent, where values for the combined sensible and latent heat flux on the order 1100 W/m<sup>2</sup> have been measured (Grossman and Betts, 1990).

Even though our surface fluxes of sensible and latent heat appear low we do not think this is an indication of an erroneous treatment of the surface fluxes in the RAMS. Figure 5.37 show the wind in the lowest model level in grid 3 and we see generally light winds except close to the sea-ice boundary South of Svalbard where we also find the largest surface fluxes (Fig. 5.35b and 5.36b). It is thus possible, that somewhat stronger winds will increase the surface fluxes sufficiently to allow the deep convection to develop.

From the above we conclude that the "model environment" in the vicinity of the polar low development deviated from the conditions in the real atmosphere. Satellite images (e.g. Fig. 4.04 and 4.06) showed extensive convection in regions where no or very little convection was forecasted in the model simulations. Another reason for the failure of the numerical models to simulate the polar low development is the absence of the upper level mesoscale vortex which is evident in the observations but is missing in the HIRLAM data assimilation (ref. Section 5.3.1.1).

### 5.3.2.2 Simulation of an arctic boundary layer front

In this Section we will give a description of an arctic boundary layer front as simulated by the RAMS. These shallow baroclinic zones, often less than one kilometer deep, associated with very cold air flowing off the ice have been connected with the formation of polar lows, e.g. Fett (1989). Differential heating from the surface probably play a role in the maintenance of these fronts and two cases have been documented by aircraft data (Shapiro and Fedor, 1989 and Shapiro et al., 1989).

For this simulation we use the same coarse grid as in Section 5.3.2.1 with 51 by 51 grid points in the horizontal and a grid distance of 50 km. In the vertical we have 30 levels in all three grids reaching about 80 hPa. Inside grid 1 we have nested grid 2 with a 59 by 59 point horizontal grid. The nest ratio is 3. Grid 3 is nested inside grid 2 also with a nest ratio of 3 in the horizontal having 71 by 71 points in the horizontal. Finally, grid 4 is nested inside grid 3 with a ratio of 4 having 70 by 70 points in the horizontal. For the description of the boundary layer front, however, we will only refer to results from grid 3 which have a grid distance of

5.5 km in the horizontal. Figure 5.38 shows the geographical extent and position of the four grids. Only the explicit microphysics is applied in grid 3 with no use of the convective parameterization.

We will concentrate on the region South to South East of Svalbard where we see a sharp low level baroclinic zone after 8 hours of integration as evidenced in Fig. 5.39. In the following we will be presenting cross sections along the line AA in Fig. 5.39. Figure 5.40 shows the potential temperature in the AA cross section. It is seen that the boundary layer thickness is at most 800 m over the open sea with a stratification very close to neutral. A little seaward of the ice-sea interface the boundary layer front reaches the sea surface. Above the boundary layer the temperature profile is fairly homogeneous horizontally. Figure 5.41 shows the potential temperature gradient along the line AA (positive towards the North West in Fig. 5.39) and exhibit only large values where the boundary layer front reaches the sea surface.

Figure 5.42 shows for the cross section AA the wind component perpendicular to the vertical plane defined by the line AA in Fig. 5.39 (positive towards the North East), i.e. the wind nearly parallel to the sea-ice boundary. A low level jet reaching 14 m/s is found on the cold side of the boundary layer front in agreement with the observations of Shapiro et al., 1989 (SAL). The wind decreases in accordance with the thermal wind as we go higher up in the atmosphere and it is interesting to see whether this along-front wind component is in geostrophic balance. Figure 5.43 shows the a-geostrophic along-front wind component, i.e. perpendicular to the line AA in Fig. 5.39. It is seen to be relatively small in general except for the lowest part of the boundary layer where friction slows down the wind in the vicinity of the boundary layer front which is in agreement with SAL. At the top of the boundary layer front a region of slightly super geostrophic wind is found, a result not reported by SAL.

If we look at the cross-frontal wind component (positive towards the Northwest) Fig. 5.44 shows an off ice component on the cold side of the boundary layer front and an on ice component at the top. Figure 5.45 shows that for the cross frontal flow the ageostrophic component is significant not only at the lowest level of the boundary layer due to friction, but generally. Again a result which compare well with SAL. To complete the cross frontal flow description Fig. 5.46 gives the vertical velocity along the line AA showing together with Fig. 5.44 that a direct circulation is established in the boundary layer frontal region.

Shapiro and Fedor (1989) found high potential vorticity values ( $2 - 3 \cdot 10^{-7} \text{ K s}^{-1} \text{ Pa}^{-1}$ ) in the stably stratified boundary layer inversion ascribing this to the formation of high potential vorticity air through radiative cooling over the ice. When the air moves out over the sea the sensible heat flux from the relatively warm sea will erode the potential vorticity from below through decreased stability at the lowest levels. Figure 5.47 shows the same qualitative structure with potential vorticity values of  $1 \text{ to } 2 \cdot 10^{-7} \text{ K s}^{-1} \text{ Pa}^{-1}$ .

As mentioned in the beginning of this Section the vorticity associated with the boundary layer front is seen as a potentially important feature in relation to the formation of polar lows. Figure 5.48 a) - c) shows the relative vorticity at levels close to 300, 800 and 1400 m height. It is seen that the highest values reaching  $3.5 \cdot 10^{-4} \text{ s}^{-1}$  is found in a narrow zone at the top of the boundary layer front whereas the relative vorticity is weaker and more homogeneous below and especially above that level.

In this Section we have compared the features of a simulated boundary layer front with observations from an aircraft. Even though it is two different situations we see good general agreement between the simulation and the observations. These boundary layer fronts are a quasi-permanent feature in the Greenland and Norwegian Seas and can as shown above, be simulated well by numerical models. If the models can treat the upper level disturbances correctly (which in general will mean analyse the feature) successful forecasts of polar low developments associated with the interaction between upper level disturbances and boundary layer fronts should be possible.

### 5.3.2.3 Representation of clouds in the RAMS

One of the reasons for using the RAMS to simulate the polar low development is the possibility of using an explicit treatment of the cloud microphysics. Emanuel and Rotunno (1989) using an axisymmetric model including explicit treatment of the moist processes showed the potential for simulating the deepening of polar lows through non-baroclinic forcing. Also Zhang (1989) showed the importance of including explicit treatment of the moist processes in the simulation of mesoscale systems where convection plays an important role.

As described in the previous Sections the RAMS simulations performed have not produced any significant explicitly resolved convective clouds. In general the magnitude of the vertical velocities have been on the order of 5 cm/s at the most in the region of interest which is well below what is expected in convective clouds. Still the simulations have produced clouds and precipitation as described in Section 5.3.2.1.

Figure 5.49a shows a three dimensional plot of the pristine ice-crystal concentration for grid 3 (see Fig. 5.25) after 12 hours in the simulation described in Section 5.3.2.1. We note that extensive coverage exist in the boundary layer and a deep cloud of pristine ice is situated in the North Eastern corner of the grid. This deep cloud is being blown to the West by the wind partly resembling a cirrus cloud. Looking at the concentration of aggregates (Fig. 5.49b) we see more or less the same picture with extensive coverage in the boundary layer and in the South Western corner the depth of the aggregate cloud is somewhat increased in connection with the trough West of Northern Norway. Along the boundary layer front (in the North Eastern part of the grid) described in Section 5.3.2.2 we see the aggregate cloud extend even higher up to 3 - 4 km in connection with the frontal convergence.

It has not been possible to evaluate the ability of the microphysical model to simulate arctic convection as the simulations performed so far have not included any intense convective systems. The lack of convection seems to be associated with the thermal structure of the model atmosphere which as noted before is not conducive for convection and not the formulation of the explicit cloud microphysics.

## 6. CONCLUDING REMARKS

In this report we have described the results of a project on polar lows in the (Northeast) Greenland Sea and adjacent regions.

For a better understanding of the processes involved in polar low formation particularly in the Northeast Greenland Sea-region an accompanying study was carried out concerning the occurrence and structure of polar lows along the total Greenland coast line. This study has shown, that polar lows occur everywhere along the Greenland coastline except in the very Northerly parts where the sea is permanently frozen. The nature of the polar lows differs very much from place to place depending on the local dominant forcing factors. An example of a hitherto unknown type of polar lows in the Greenland region is the "Angmagssalik polar low" which forms off the coast of Southeast Greenland near Angmagssalik, probably due to vortex stretching associated with a descending flow from the Greenland ice cap. Generally the polar lows in the Northeast Greenland Sea are more baroclinic than their counterpart farther towards the East in the Bear Island region, but occasionally convective systems are observed in the Fram Strait region between Svalbard and North East Greenland. Unfortunately, it was not possible to carry out a statistical investigation of the occurrence of polar lows, their structure and dynamics in the North East Greenland Sea region as part of the project, mainly because of the problems of acquiring the necessary satellite data for such a task. It can be tentatively concluded, however, that quite intense polar lows of the baroclinic type as well as of the "convective type" occasionally develop in this region, although, as expected, more rarely than further East over the "warm" Norwegian current.

The continued observational study of the polar low outbreak from 12 to 16 December 1982 in the Bear Island region has revealed the complex nature of the formation of polar lows on scales as small as around 100 km.

In order to overcome the problems associated with the lack of sufficient data especially on the mesoscale, different approaches were attempted to obtain the best possible understanding of the dynamics and structure of the polar lows in the region. These attempts included the formulation of different diagnostic "omega-equation models" including a semi-geostrophic version in order to account for the small horizontal scale of most polar lows. One of the advantages of using the (linear) omega-equations (and actually the primary reason for using these equations in part of the project) is, of course, that the effect of the different forcing mechanisms can easily be isolated. After some work with these models it was concluded, however, that it would be more beneficial to concentrate the efforts on the use of the full primitive equation models.

The idea of CISK traditionally has played an important role in the on-going debate on the nature of polar lows, and both authors have previously contributed to this debate. It was decided therefore, as part of the project to investigate the connection between the new "Free Ride" - theory and CISK.

The main effort of the project was concentrated on a numerical simulation of the polar low episode (or "outbreak") in the Bear Island region from December 12 to December 16, 1982. The polar low developments which were observed during this outbreak have been notoriously difficult to tackle for numerical models and modelers. Several (unpublished) unsuccessful attempts to simulate the initial developments from December 12 to 14 have been carried out, but so far without success. In the present work we made use of two highly sophisticated models, i.e. the HIRLAM and RAMS. Unfortunately, already in the data assimilation process serious problems arose when the important upper level vortex which triggered the initial polar low formation was "smoothed" away as part of the analysis



process. This problem was intimately connected with the inability of the model to forecast this vortex for which reason it was not included in the first guess field. Other serious problems were associated with the way that convection is represented and simulated in the models.

The formation of the initial baroclinic disturbance which served as a precursor for the subsequent formation of a convective type of polar low, was moderately well simulated by the models, although the exact position and strength could not be reproduced, probably because of the problems associated with the representation of small scale phenomena in the HIRLAM. We were not able successfully to simulate the subsequent development of the convective polar lows. The reasons for this are many among which the most important are the problems with small horizontal scales and the way convection is handled in the models.

Supplementary to the work described above we carried out an IPV analysis showing, that the formation of the baroclinic polar low in a qualitative way could be understood by using the now very popular "IPV-thinking".

Many polar low formations in the region are closely connected to the existence of a low level "arctic boundary layer front" along the ice edge. As part of our work we have demonstrated that the RAMS simulation of these fronts in general is in agreement with recent observational results.

## 7. ACKNOWLEDGMENTS

Ref. Section 5.1 we would like to thank the HIRLAM group for providing the analysis used for this study and Wayne Schubert for bringing the works by R. Wu and W. Blumen to our attention. The computing was performed at the Danish Meteorological Institute.

Ref. Section 5.2 we thank Wayne Schubert for his interest in and encouragement of this work and Aksel Wiin-Nielsen for numerous fruitful discussions on the nature of the CISK and Free Ride assumptions.

Ref. Section 5.3 we thank the HIRLAM group and Professor W.R. Cotton for making respectively the HIRLAM and RAMS available for this study. The work was partially supported by the National Center for Supercomputing Applications (USA) under Grant ATM890019N and utilized the CRAY-2 system at the National Center for Supercomputing Applications, University of Illinois at Urbana - Champaign. Acknowledgement is made to the National Center for Atmospheric Research (USA), which is sponsored by the National Science Foundation, as well as the Danish Meteorological Institute for allocating computing time for this study.

## 8. REFERENCES

- Aakjær, P. D., 1987: Polar lows passing Denmark. Ph.D. Thesis, University of Copenhagen.
- Anthes, R.A., 1982: Tropical cyclones. Their evolution, structure and effects. *Am. Meteor. Soc.*, 208 pp.
- Blumen, W., and Wu R., 1933: Baroclinic instability and frontogenesis with Ekman boundary layer dynamics incorporating the geostrophic momentum approximation. *J. Atmos. Sciences*, 40, 2630-2637.
- Bretherton, F., 1966: Critical layer instability in baroclinic flow. *J. Atmos. Sci.*, 36, 1925 - 1933.
- Businger, S., 1987: The synoptic climatology of polar low outbreaks. *Tellus* 37A, 419-432.
- Businger, S. and Reed, R.J. 1989: Polar Lows. In *Polar and Arctic Lows*, Twitchell P.F., Rasmussen E.A. and Davidson K.L. (Eds.), A. Deepak Publishing, Hampton, Virginia, USA, 3 - 46.
- Chang, C.P., 1973: A dynamical model of the intertropical convergence zone. *J. Atmos. Sci.*, 30, 190 - 212.
- Chang, C.P. and Williams, R.T., 1974: On the short wave cut-off of CISK. *J. Atmos. Sci.*, 21, 68 - 75.
- Charney, J.G. and Eliassen, A., 1964: On the growth of the hurricane depression. *J. Atmos. Sci.*, 21, 68 - 75.
- Chen, C. and Cotton, W.R., 1983: A one-dimensional simulation of the stratocumulus-capped mixed layer, *Boundary-Layer Meteorol.*, 25, 289 - 321.
- Emanuel, K.A. and Rotunno, R., 1989: Polar lows as arctic cyclones. *Polar and Arctic Lows*, Twitchell, P.F., E.A. Rasmussen and K.L. Davidson (Eds.), A. Deepak, Hampton, Virginia, p 141 - 154.
- Emanuel, K.A., 1983: On the dynamical definition(s) of "mesoscale". *Mesoscale meteorology - theory, observations and models*, (Eds. D. K. Lilly and T. Gal-Chen) Dordrecht-Boston, D. Reidel Publishing Co., 1-11.
- Fett, R.W., 1989: Polar low development associated with boundary layer fronts in the Greenland, Norwegian and Barents Seas. *Polar and Arctic Lows*, Twitchell, P.F., E.A. Rasmussen and K.L. Davidson (Eds.), A. Deepak, Hampton Virginia, p 313 - 330.
- Fingerhut, W. A., 1978: A numerical model of a diurnally varying tropical cloud cluster disturbance. *Mon. Wea. Rev.*, 106, 255 - 264.
- Flatau, P.J., Tripoli, G.J., Verlinde, J. and Cotton, W.R., 1989: The CSU-RAMS cloud microphysics module: General theory and code documentation. Department of Atmospheric Science, Colorado State University. Atmospheric Science paper No. 451, 88 pp.
- Fraedrich, K. and McBride, J.L., 1989: The physical mechanism of CISK and the Free Ride balance. *J. Atmos. Sci.*, 46, 2642 - 2648.
- Frank, W.M., 1980: Modulations of the net tropospheric temperature during GATE. *J. Atmos. Sci.*, 37, 1056 - 1064.
- Frank, W.M., 1983: The cumulus parameterization problem. *Mon. Wea. Review*, 111, 1859-1871.
- Grossman, R.L. and Betts, A.K., 1990: Air-sea interaction during an extreme cold air outbreak from the Eastern coast of the United States. *Mon. Wea. Rev.*, 118, 324 - 342.
- Harrold, J.W. and Browning, K.A., 1969: The polar low as a baroclinic disturbance. *Quart. J. Roy. Soc.*, 95, 710 - 723.

- Holton, J.R., 1972: An introduction to dynamic meteorology. Academic Press, 319 pp.
- Hoskins, B.J., 1975: The geostrophic momentum approximation and the semi-geostrophic equations. *J. Atmos. Sciences*, 32, 233-242.
- Hoskins, B.J., and Bretherton, F., 1972: Atmospheric frontogenesis models: Mathematical formulation and solution. *J. Atmos. Sciences*, 29, 11-37.
- Hoskins, B.J., and Draghici, I., 1977: The forcing of ageostrophic motion according to the semi-geostrophic equations in an isotropic coordinate model. *J. Atmos. Sciences*, 34, 1859-1867.
- Hoskins, B.J., Draghici, I. and Davies, H.C., 1978: A new look at the omega equation. *Quart. J. Roy. Meteor. Society*, 104, 31-38.
- Hoskins, B., McIntyre, M.E. and Robertson, A.W., 1985: On the use and significance of isentropic potential vorticity maps. *Quart. J. Roy. Meteorol. Soc.*, 111, 877-946.
- Kikuchi, K., Tsuboya, S., Sato, N., Asuma, Y., Takeda, T., and Fujiyoshi, Y., 1982: Observation of wintertime clouds and precipitation in the arctic Canada (POLEX-North). Part 2: Characteristic properties of precipitation particles. *J. Meteor. Soc. Japan*, 60, 1215 - 1225.
- Kleinschmidt, E., 1957: In "Dynamic Meteorology " by Eliassen, A. and Kleinschmidt, E., *Handbuch der Physik*, 48, 112-129.
- Klemp, J.B. and R.B. Wilhelmson, 1978: The simulation of three-dimensional convective storm dynamics. *J. Atmos. Sci.*, 35, 1070 - 1096.
- Liou, C-S., and Elsberry, R.L., 1987: Heat budgets of analyses and forecasts of an explosively deepening maritime cyclone. *Mon. Wea. Review*, 115, 1809-1824.
- Louis, J.F., 1979: A parametric model of vertical eddy fluxes in the atmosphere. *Boundary-Layer Meteorol.*, 17, 187 - 202.
- Machenhauer, B. (Ed.), 1988: HIRLAM Final Report. HIRLAM Technical Report No. 5, Copenhagen December 1988, 116 pp. Available from the Danish Meteorological Institute, Lyngbyvej 100, DK-2100 Copenhagen E, Denmark.
- Maddox, R.A., 1980: An objective technique for separating macroscale and mesoscale features in meteorological data. *Mon. Wea. Review*, 108, 1108-1121.
- Mak, M., 1981: An inquiry on the nature of CISK. Part I. *Tellus*, 33, 531 - 537.
- Ninomiya, K., 1989: Polar / Comma-cloud lows over the Japan Sea and the Northwestern Pacific in winter. *J. Meteorol. Soc. Japan*, 67, 83 - 97.
- Nordeng, T-E. 1987: The effect of vertical slantwise convection on the simulation of polar lows. *Tellus*, 39A, 354 - 375.
- Nordeng, T-E. and Rasmussen, E.A., 1992: A most beautiful polar low. A case study of a polar low development in the Bear Island region. Accepted for publication by *Tellus*.
- Oekland, H., 1977: On the intensification of small-scale cyclones formed in very cold air masses heated by the ocean. Institute rep. series, No. 26, University of Oslo, Institutt for Geofysik.
- Ooyama, K. 1969: Numerical simulation of the life cycle of tropical cyclones. *J. Atmos. Sci.*, 26, 3-40.
- Parish, T.R. and Bromwich, D.H., 1986: The inversion wind pattern over West Antarctica. *Mon. Wea. Rev.*, 114, 849 - 860.
- Parish, T.R. and Bromwich, D.H., 1991: Continental-scale simulation of the Antarctic katabatic wind region. *J. Climate*, 4, 135 - 146.

- Parish, T.R. and Weadler, G., 1991: The katabatic wind regime at Adelie Land, Antarctica. *Intern. J. Clim.*, 11, 97 - 107.
- Pedersen, T.S., 1988: On the primary forcing mechanism during a polar low development in the Svalbard region. *Palmen Memorial Symposium on extratropical cyclones*, AMS, p 157-160.
- Pedersen, T.S., 1989: On the effect of using different formulations for the forcing in the omega-equation applied to polar lows. *Polar and Arctic Lows*. Twitchell, E.A. Rasmussen and K.L. Davidson (Eds.), A. Deepak, Hampton Virginia, p 233-246.
- Pedersen, T.S., 1991: A comparison of the Free Ride and CISK assumptions. *J. Atmos. Sci.*, 48, 1813 - 1821.
- Pedersen, T.S. and Rasmussen, E.A., 1985: On the cut-off problem in linear CISK-models. *Tellus*, 37A, 394 - 402.
- Rasmussen, E.A., 1977: The polar low as a CISK phenomenon. Rep. No. 6. University of Copenhagen, Institute for Theoretical Meteorology.
- Rasmussen, E.A., 1979: The polar low as an extratropical CISK - disturbance. *Quart. J. Roy. Meteor. Soc.*, 105, 531 - 549.
- Rasmussen, E.A., 1985a: A polar low development over the Barents Sea. Technical Report No. 7, The Norwegian Polar Lows Project, 42 pp.
- Rasmussen, E.A., 1985b: A case study of a polar low development over the Barents Sea. *Tellus*, 37A, 407-418.
- Rasmussen, E.A., 1989: A comparative study of tropical cyclones and polar lows. *Polar and Arctic Lows*, Twitchell, P.F., E.A. Rasmussen and K.L. Davidson (Eds.), A. Deepak, Hampton Virginia, p 47 - 80.
- Rasmussen, E.A. and Zick, C., 1987: A subsynoptic vortex over the Mediterranean with some resemblance to polar lows. *Tellus*, 39A, 408-425.
- Rasmussen, E.A. and Purdom, J.F., 1992: Investigation of a polar low using geostationary satellite data. Manuscript to be presented at Sixth Conference on Satellite Meteorology and Oceanography, January 5-10, 1992, Atlanta.
- Rasmussen, E.A., Pedersen, T.S., Pedersen, L.T. and Turner, J., 1991: Polar lows and arctic instability lows in the Bear Island region. Accepted for publication by *Tellus*.
- Rasmussen, L., 1989: Greenland winds and satellite imagery. *Vejret - Special Issue in English*, N.W. Nielsen (Ed.), 32 - 37. Available from the Danish Meteorological Society.
- Reed, R.J., 1985: Baroclinic instability as a mechanism for polar low formation. In *Proceedings of The International Conference on Polar Lows*, Oslo, Norway, 141-149.
- Reed, R.J., 1991: Cyclogenesis from a potential vorticity perspective. Preprints from the first international conference on winter storms, New Orleans, LA., Jan 14 - 18, 1991, 436 pp.
- Semtner, A.J., 1976: A model for the thermodynamic growth of sea ice in numerical investigations of climate. *J. Phys. Oceanogr.*, 6, 379 - 389.
- Shapiro, M.A. and Fedor, L.S., 1989: A case study of an ice-edge boundary layer front and polar low development over the Norwegian Seas. *Polar and Arctic Lows*. Twitchell, P.F., E.A. Rasmussen and K.L. Davidson (Eds.), A. Deepak, Hampton Virginia, p 257 - 277.
- Shapiro, M.A., Hampel, T. and Fedor, L.S., 1989: Research aircraft observations of an arctic front over the Barents Sea. *Polar and Arctic Lows*. Twitchell, P.F., E.A. Rasmussen and K.L. Davidson (Eds.), A. Deepak, Hampton Virginia, p 279 - 289.

- Trembach, C.J., 1990: Numerical simulation of a mesoscale Convective complex: Model development and numerical results. Department of Atmospheric Science, Colorado State University. Atmospheric Science paper No. 465, 247 pp.
- Trembach, C.J. and Kessler, R., 1985: A surface temperature and moisture parameterization for use in mesoscale models. Preprints, 7th Conference on Numerical Weather Prediction, 17-20 June 1985, Montreal, Canada, AMS.
- Tripoli, G.J., 1986: A numerical investigation of an orogenic mesoscale convective system. Department of Atmospheric Science, Colorado State University. Atmospheric Science paper No. 401, 290 pp.
- Tripoli, G.J. and Cotton, W.R., 1982: The Colorado State University three-dimensional cloud / mesoscale model - 1982. Part I: General theoretical framework and sensitivity experiments. *J. de Rech. Atmos.*, 16, 185 - 220.
- Twitchell, P.F. and Fett, R., 1988: Small high-latitude ocean storms. Port and ocean engineering under arctic conditions. Vol. III, The Geophysical Institute, University of Alaska, Fairbanks.
- Twitchell, P.F., Rasmussen, E.A. and Davidson, K.L. (Eds.), 1989: "Polar and Arctic Lows", A. Deepak Publishing, Hampton, Virginia, USA, 421 pp
- van Delden, A., 1989a: On the deepening and filling of balanced cyclones by diabatic heating. *Meteorol. Atmos. Phys.*, 41, 127 - 145.
- van Delden, A., 1989b: Gradient wind adjustment, CISK, and the growth of polar lows by diabatic heating. In *Polar and Arctic Lows*, Twitchell P.F., Rasmussen E.A. and Davidson K.L. (Eds.), A. Deepak Publishing, Hampton, Virginia, USA, 109 - 130.
- Wadhams, P., 1981: The ice cover in the Greenland and Norwegian Seas. *Reviews of Geophysics and Space Physics*, 19, 345 - 393.
- Wilhelmsen, K., 1985: Climatological study of gale producing polar lows near Norway. *Tellus*, 37A, 451 - 459.
- Wu, R., and Blumen, W., 1982: An analysis of Ekman boundary layer dynamics incorporating the geostrophic momentum approximation. *J. Atmos. Sciences*, 40, 1774-1782.
- Zhang, D-L., 1989: The effect of parameterized ice microphysics on the simulation of vortex circulation with a mesoscale hydrostatic model. *Tellus*, 41A, 132 - 147.

## 9. FIGURE LEGENDS

Figure 2.01 NOAA-9 infrared satellite image 0418 UTC, February 27, 1987. Photograph Department of Electrical Engineering and Electronics, University of Dundee.

Figure 3.01 Map showing the geography of the region together with the climatological ice boundary (solid line stretching from West of Iceland to Novaya Zemlaya) for the month of December (after Wadhams 1981).

Figure 3.02 Streamlines for the katabatic flow from the Greenland ice cap. After Rasmussen (1989, L.).

Figure 3.03 TIROS infrared satellite image 11.35 UTC, Marts 12, 1981 showing polar low (indicated by arrow) at Angmagssalik, South East Greenland.

Figure 3.04 German Weather Service Analyses November 15, 1987.  
a) 500 hPa height (solid, 40 dm increment) and temperature (dashed, 4 °C increment). Valid 00 UTC.  
b) Mean sea level pressure (5 hPa increment). Valid 06 UTC.

Figure 3.05 German Weather Service Analyses November 16, 1987.  
a) 500 hPa height (solid, 40 dm increment) and temperature (dashed, 4 °C increment). Valid 00 UTC.  
b) Mean sea level pressure (5 hPa increment). Valid 06 UTC.

Figure 3.06 German Weather Service Analyses November 17, 1987.  
a) 500 hPa height (solid, 40 dm increment) and temperature (dashed, 4 °C increment). Valid 00 UTC.  
b) Mean sea level pressure (5 hPa increment). Valid 06 UTC.

Figure 3.07 NOAA-11 infrared satellite image 15.11 UTC March 20, 1989 showing a characteristic polar low over the Labrador Sea. Photograph courtesy of Department of Electrical Engineering and Electronics, University of Dundee.

Figure 3.08 NOAA-11 infrared satellite image 15.24 UTC January 18, 1989 showing a "Davis Strait low". Photograph courtesy of Department of Electrical Engineering and Electronics, University of Dundee.

Figure 4.01 Sea ice extend and sea surface temperatures (°C) December 1982.

Figure 4.02 NOAA-mosaic December 12, 1982. The arrow marked A shows the incipient polar low (around 1300 UTC) deep in the cold air mass. The arrows marked B indicate clouds belonging to the polar front. The Scandinavian Peninsula is seen in central part of the picture.

Figure 4.03 NOAA-7 infrared satellite image 1257 UTC December 12, 1982 showing polar low A West of Bear Island ( Bear Island marked by arrow). The ice edge around Svalbard (S) and East of Greenland (G) is indicated by open arrows. Photograph courtesy of Department of Electrical Engineering and Electronics, University of Dundee.

Figure 4.04 NOAA-7 infrared satellite image 0250 UTC December 13, 1982 showing cloud vortex associated with the upper-level disturbance. Svalbard (S) and Northern Scandinavia (N) have been indicated. Photograph courtesy of Department of Electrical Engineering and Electronics, University of Dundee.

Figure 4.05 Surface map 0000 UTC December 14, 1982.

Figure 4.06 NOAA-7 infrared satellite image 0419 UTC December 14, 1982. The approximate position of the center of the vortex (compare Fig. 4.05) has been indicated by "V". A local 'arctic front' at the leading edge of the shallow cold air outbreak West of Bear Island (indicated by open arrow) is shown by the thick dash-dotted line. The shallow cold air mass can easily be identified by the system of well-developed cloud streets. The Western boundary of the warm, modified air mass East of the shallow cold air mass has been indicated W-W-W. The cluster of cumulonimbus clouds marked "C", is situated in the region where vortex C is first observed around 6 hours later at 1045 UTC. Photograph courtesy of Department of Electrical Engineering and Electronics, University of Dundee.

Figure 4.07 Observations from weather ship AMI. The arrow shows the time at which the center of vortex A passes AMI.  
 a) Surface winds in m/s (long barb indicates five m/s) and North "upwards". Sea surface temperature (thin solid line).  
 b) Surface air temperature (thin dashed line), dewpoint temperature (thin solid line), surface wet bulb potential temperature ( $\theta_w$ , thick solid line).

Figure 4.08 Radiosonde ascent (temperature and dew-point) Bear Island 1200 UTC December 13, 1982 (curve I). Curve II shows moist adiabatic ascent of a parcel from the surface with initial temperature and dewpoint as measured at AMI 1200 UTC December 13 corresponding to  $\theta_w = 270$  K. Curve III shows moist adiabatic ascent of a parcel with a much higher surface temperature as measured later on at AMI during disturbed conditions ( $\theta_w = 274$  K). The "modified" Bear Island sounding referred to in the text, is obtained by replacing the stable layer below 860 hPa with a neutral layer  $\theta = 272$  K. Winds are given with North "upwards" and long barbs indicate 5 m/s.

Figure 4.09 Mean wind velocity (ff) in m/s (10 minutes mean) and surface pressure (ppp) from weather ship AMI (71.5 N, 19 E) from 2000 UTC December 13, 1982 to 0600 UTC December 14, 1982.

Figure 4.10 a. NOAA-7 infrared satellite image 0406 UTC December 15, 1982. Arrows marked C, C\* and E show the decaying vortex C, the newly formed vortex C\* and the cumulonimbus cluster which later on developed into vortex E. The shallow cold air mass East of 20°E is clearly indicated by the system of cloud streets and the region of a shallow overcast.  
 b. An enlargement of the region around vortex C\* in Fig. 4.10a. Photograph courtesy of Department of Electrical Engineering and Electronics, University of Dundee.

Figure 4.11 Surface observation from Bear Island during the passage of vortex C\* showing wind velocity in knots. The passage of the "eye" has been marked by an arrow. Time is given in local time, i.e. UTC plus one hour.

Figure 4.12 Barograph record from Bear Island showing surface pressure from 0600 UTC December 13 to December 18, 1982.

Figure 4.13 Mean surface wind velocity ( $\bar{u}$ ) in m/s (10 minutes mean) and surface pressure (ppp) from Bear Island 1100 UTC to 1900 UTC, December 15, 1982.

Figure 4.14 NOAA-7 infrared satellite image 1400 UTC December 15, 1982 showing vortex C\* East of Bear Island (marked by B). The open arrow indicates the upper level outflow. Photograph courtesy of Department of Electrical Engineering and Electronics, University of Dundee.

Figure 4.15 NOAA-7 infrared satellite image 0354 UTC December 16, 1982 showing vortex C\*. Photograph courtesy of Department of Electrical Engineering and Electronics, University of Dundee.

Figure 5.01 HIRLAM analysis for 0000 UTC December 13, 1982. a) MSL pressure in hPa. The x indicates the position of the polar low. b) 530 hPa heights in dm. The thick black line indicates the orientation of the cross section shown in Figs. 3 and 4.

Figure 5.02 Vertical velocity (cm/s) from the QGO with adiabatic forcing. 0000 UTC December 13, 1982 along the cross section indicated on Fig. 5.01. Dash/dot indicates ascent/descent. The arrow identifies the location of the polar low. (1) total forcing, (2) AVO, (3) ATH, (4) ACA.

Figure 5.03 Vertical velocity from the SGO with adiabatic forcing (1), two types of diabatic forcing as described in the text (2) and (3). Conventions and units as in Fig. 5.02.

Figure 5.04 The balance between the terms A, B and C in (5.2.10) for the heating profile (5.2.13) as function of the perturbation wave length. The Rossby deformation radius is indicated on the abscissa. The parameters used are:

$$p_B = 900 \text{ hPa}, p_1 = 900 \text{ hPa}, p_* = 300 \text{ hPa}, q_B = 20 \text{ g/kg}, \rho = 1.2 \text{ kg/m}^3,$$

$$a = 10^{-4} \text{ Pa}^{-1}, L = 2.5 \cdot 10^5 \text{ J/kg}, c_p = 1004 \text{ J/(kg K)}, R = 287 \text{ J/(kg K)}$$

From Charney and Eliassen (1964) we take:

$$K = 10 \text{ m}^2/\text{s}, f = 3.77 \cdot 10^{-5} \text{ s}^{-1}$$

and from Mak (1981) we let:

$$S = 10^{-6} \text{ J/(kg Pa}^2\text{)}$$

Perturbation wave lengths: 25 - 2500 km.

Figure 5.05 Growth rate curves for the integrated Free Ride ( $\sigma_{FR1}$ ) and CISK ( $\sigma_{CI}$ ) as a function of the perturbation wave length. Parameters are chosen as in Fig. 5.04.



Figure 5.06 Growth rate curves for the local Free Ride ( $\sigma_{FR2}$ ) and CISK ( $\sigma_{CI}$ ) as a function of the perturbation wave length. Parameters are chosen as in Fig. 5.04 except for  $p_* = 0 \text{ hPa}$ .

Figure 5.07 Absolute value (%) of the ratio A/C from (5.2.23) in CISK. Parameters are chosen as in Fig. 5.06. Isolines every 1%.

Figure 5.08 Absolute value (%) of the ratio A/C from (5.2.23). Isolines every 1% up to 10%, then every 50% from 50% and upwards.  
a) Parameters as in Fig. 5.04.  
b) Parameters as in Fig. 5.04 except for  $p_* = 0 \text{ hPa}$ .

Figure 5.09 The A term in (5.2.23). Parameters as in Fig. 5.04 except for  $p_* = 0 \text{ hPa}$ .

Figure 5.10 Model domain used in the data assimilation with the HIRLAM system.

Figure 5.11 Uninitialized analysis valid at 00 UTC December 14, 1982.

Figure 5.12 Analyses valid at 00 UTC December 13, 1982. Synop stations referred to in the text: BI Bear Island, H Hopen, AMI weather ship, NK North Kvaloy.  
a) Uninitialized analysis.  
b) Subjective analysis.

Figure 5.13 Time series of MSL pressure at 4 stations indicated on Figure 5.12. Solid line indicate uninitialized analyses and x observations.

Figure 5.14 Uninitialized analysis of wind (stippled lines isotachs) at the 965 hPa level, 12 UTC December 12, 1982.

Figure 5.15 Uninitialized analysis of 500 hPa height (solid lines) and temperature (dashed lines) 12 UTC December 12, 1982. Radio sonde stations referred to in the text: BB Barentsburg, BI Bear Island, BO Bodo.

Figure 5.16 Time series of 500 hPa height at 3 stations indicated on Figure 5.15. Solid line indicate uninitialized analyses and x observations.

Figure 5.17 Vertical soundings 12 UTC December 12, 1982.  
a) Uninitialized analysis.  
b) Observation from Bear Island.

Figure 5.18 500 hPa subjective analysis of the height field 12 UTC December 12, 1982. Contours in dekameters and observations show height, temperature ( $^{\circ}\text{C}$ ) and wind at the 500 hPa level. The observations marked by asterisk are derived from satellite data and taken from maps produced by the National Climatic Center, North Carolina, USA. The track of the upper level low from 00 UTC December 11 to 12 UTC December 12, 1982, is indicated by open squares. After Rasmussen 1985b.

Figure 5.19 Uninitialized analysis of 500-1000 hPa thickness 12 UTC December 12, 1982. Wind arrows show observed values of the thermal wind.

Figure 5.20 Uninitialized analysis of 500-1000 hPa thickness 12 UTC December 13, 1982. Wind arrows show observed values of the thermal wind.

Figure 5.21 a) 6 hour forecast of 1000 hPa geopotential height (solid, 40 m interval) and temperature (dashed, 4 °C interval) valid 00 UTC December 14, 1982.  
b) 6 hour pressure tendency between 18 UTC December 13 and 00 UTC December 14, 1982. Contour interval 0.5 hPa.

Figure 5.22 6 hour accumulated convective precipitation between 18 UTC December 13 and 00 UTC December 14, 1982. Contour interval 0.5 mm.

Figure 5.23 Potential vorticity on the 290 K isentropic surface. Units  $10^{-6} \text{ m}^2 \text{ K s}^{-1} \text{ kg}^{-1}$  with the 2.0 isoline enhanced.  
a) 00 UTC December 12, 1982. Greenland (G), Northern Scandinavia (N) and Svalbard (S) have been indicated.  
b) 12 UTC December 12.  
c) 00 UTC December 13.  
d) 12 UTC December 13. The tracks of the two local IPV maxima (Eastern (EA) and Western (WA)) referred to in text are shown. Stippling indicate the absence of a well defined local maximum. Dots indicate 12 hourly positions.

Figure 5.24 Temperature at the 995 hPa level valid at 12 UTC December 12, 1982

Figure 5.25 Geographical extent and position of the three grids used in the simulation of the December 13 - 14 case.

Figure 5.26 MSL pressure for the initial state of the simulation valid at 12 UTC December 13, 1982.

Figure 5.27 MSL pressure after 12 hours of simulation valid at 00 UTC December 14, 1982.  
a) Grid 1, 2 hPa contour interval. Trough along the West coast of Norway is indicated.  
b) Grid 2, 1 hPa contour interval.  
c) Grid 3, 1 hPa contour interval.

Figure 5.28 12 hour accumulated convective precipitation between 12 UTC, December 13 and 00 UTC, December 14, 1982. (grid 1). Units  $\text{kg/m}^2$ .

Figure 5.29 Lifting Condensation Level for air at 97.6 m valid 00 UTC, December 14, 1982 (after 12 hours integration). Units m.

Figure 5.30 Thickness of the layer between the Lifting Condensation Level and the equilibrium Temperature Level for air at 97.6 m valid 00 UTC, December 14, 1982. Units m.

Figure 5.31 Available Buoyant Energy as defined in text for air at 97.6 m valid 00 UTC, December 14, 1982. Units K m.

Figure 5.32 Total accumulated precipitation from the explicit microphysics between 12 UTC, December 13 and 00 UTC, December 14, 1982. Units  $\text{kg/m}^2$ .  
a) Grid 1.  
b) Grid 3.

Figure 5.33 Total accumulated aggregate precipitation from the explicit microphysics between 12 UTC, December 13 and 00 UTC, December 14, 1982. Units  $\text{kg}/\text{m}^2$ .

Figure 5.34 Temperature profiles 00 UTC December 14, 1982.  
a) Observed sounding from Bear Island.  
b) RAMS sounding

Figure 5.35 Surface sensible heat flux 00 UTC, December 14 (after 12 hours of integration). Units  $\text{w}/\text{m}^2$ .  
a) Grid 1.  
b) Grid 3.

Figure 5.36 Surface latent heat flux 00 UTC, December 14, 1982. Units  $\text{w}/\text{m}^2$ .  
a) Grid 1.  
b) Grid 3.

Figure 5.37 Wind at the 97.6 m level 00 UTC, December 14, 1982 (grid 3). Units  $\text{m}/\text{s}$ .

Figure 5.38 Geographical extent and position of the four grids used in the simulation of the boundary layer front.

Figure 5.39 Potential temperature at the 97.6 m level 20 UTC, December 13, 1982 (after 8 hours of integration) on grid 3. Units  $0.1 \text{ K}$ . AA indicates the cross section referred to in the following figures.

Figure 5.40 Potential temperature in the cross section AA (see Fig. 5.39). Units  $\text{K}$ . Sea ice concentration is indicated at the bottom. The solid line indicates between 50 and 100 % coverage. The hatched area indicates between 10 and 50 % coverage. To the right of "O" the sea is open.

Figure 5.41 Potential temperature gradient along the cross section AA (see Fig. 5.39). Units  $\text{K}/\text{m}$ .

Figure 5.42 Wind perpendicular to the cross section AA (see Fig. 5.39). Units  $\text{m}/\text{s}$ .

Figure 5.43 A-geostrophic wind perpendicular to the cross section AA (see Fig. 5.39). Units  $\text{m}/\text{s}$ .

Figure 5.44 Wind along the cross section AA (see Fig. 5.39). Units  $\text{m}/\text{s}$ .

Figure 5.45 A-geostrophic wind along the cross section AA (see Fig. 5.39). Units  $\text{m}/\text{s}$ .

Figure 5.46 Vertical wind component along the cross section AA (see Fig. 5.39). Units  $\text{cm}/\text{s}$ .

Figure 5.47 Potential vorticity along the cross section AA (see Fig. 5.39). Units  $10^{-8} \text{ K s}^{-1} \text{ Pa}^{-1}$ .

Figure 5.48 Relative vorticity 20 UTC, December 13, 1982. Units  $10^{-5} \text{ s}^{-1}$ .  
a) 307.4 m level.  
b) 791.9 m level.  
c) 1378.2 m level.

Figure 5.49 Three dimensional description of the presence of hydrometers (mixing ratio greater than zero) 00 UTC., December 14, 1982.  
a) Pristine ice-crystals.  
b) Aggregates.

## 11. DISTRIBUTION

Dr. Gary Geenaert, Code 1214  
Office of Naval Research  
800 North Quincy Street  
Arlington, VA 22217-5000  
3 Copies

Grant Administrator  
Office of Naval Research  
Resident Representative  
715 Broadway - 5th Floor  
New York, NY 10003-6896  
1 Copy

Defense Technical Information Center  
Building 5, Cameron Station  
Alexandria, Virginia 22314  
1 Copy

Office of Naval Research  
Code 400R1  
800 North Quincy Street  
Arlington, VA 22217-5000  
12 Copies

Dr. Poul F. Twitchell  
509 Schley Road  
Annapolis, MD 21401  
1 Copy

Professor Aksel Wiin-Nielsen  
Geophysical Institute  
Department of Meteorology  
University of Copenhagen  
Haraldsgade 6  
DK-2200 Copenhagen N  
1 Copy

Director Lars P. Prahm  
The Danish Meteorological Institute  
Lyngbyvej 100  
DK-2100 Copenhagen E  
1 Copy



Fig. 2.01

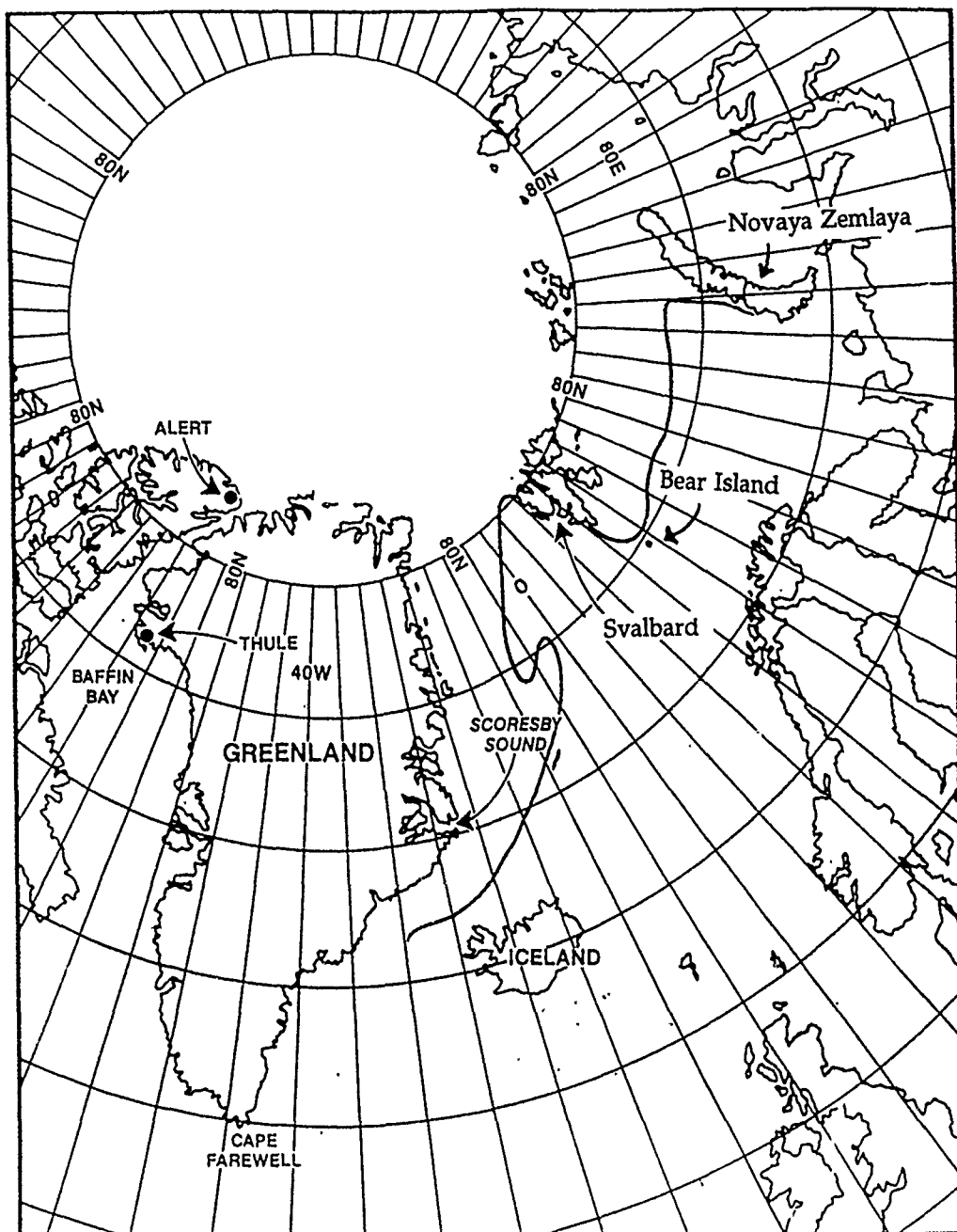


Fig. 3.01

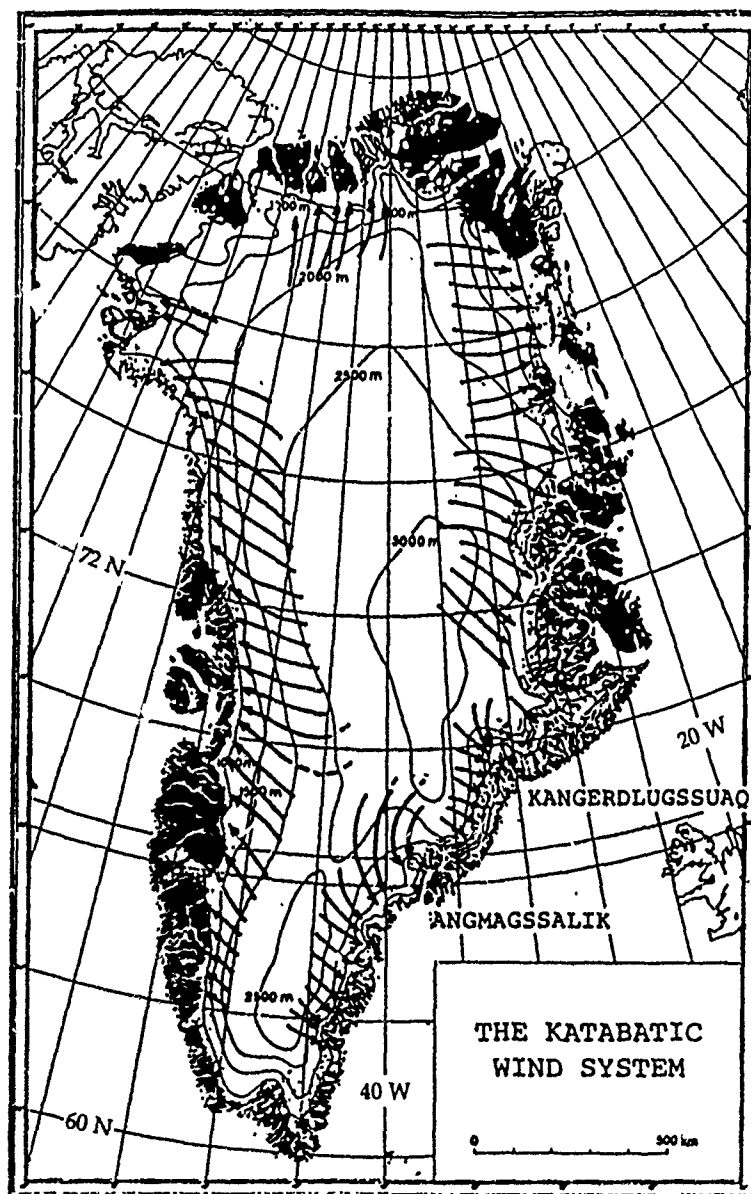


Fig. 3.02

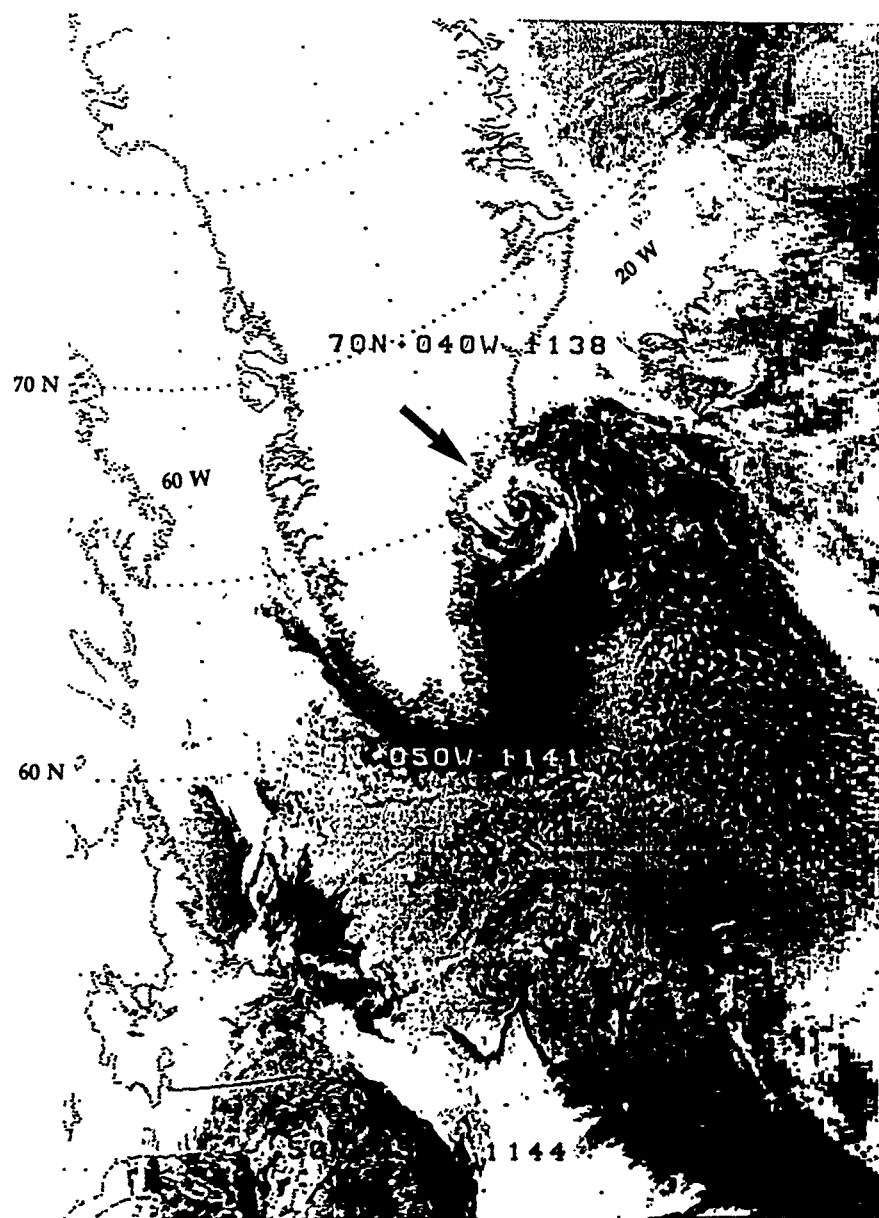
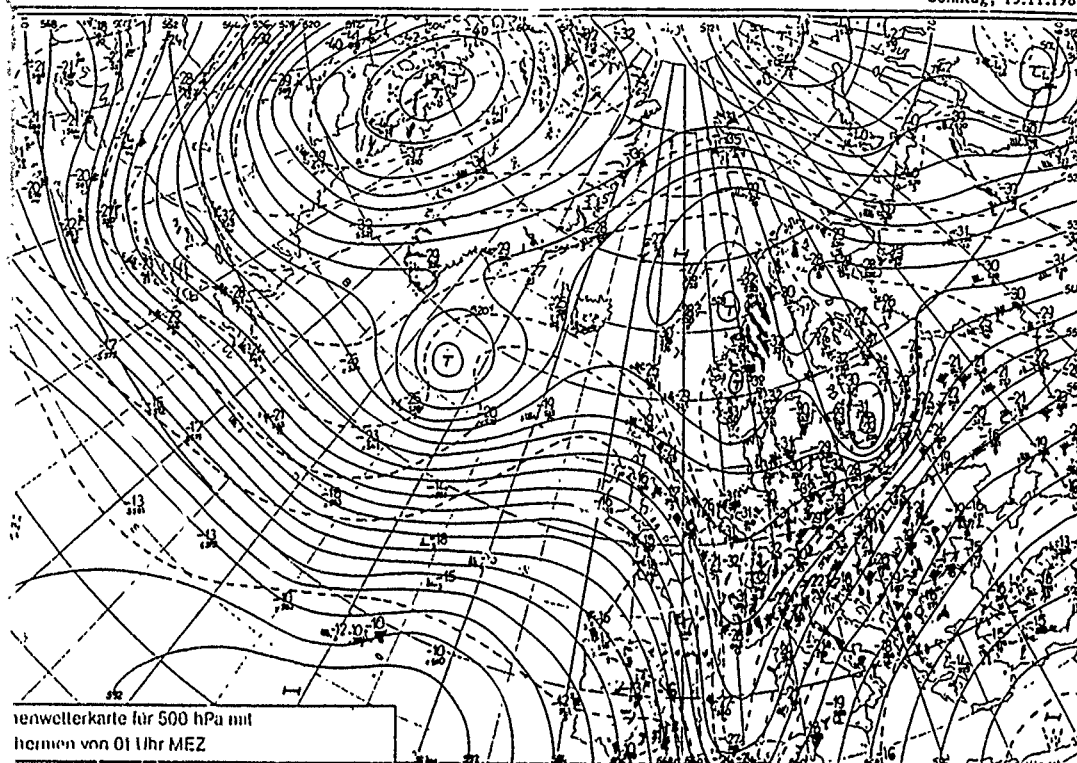


Fig. 3.03

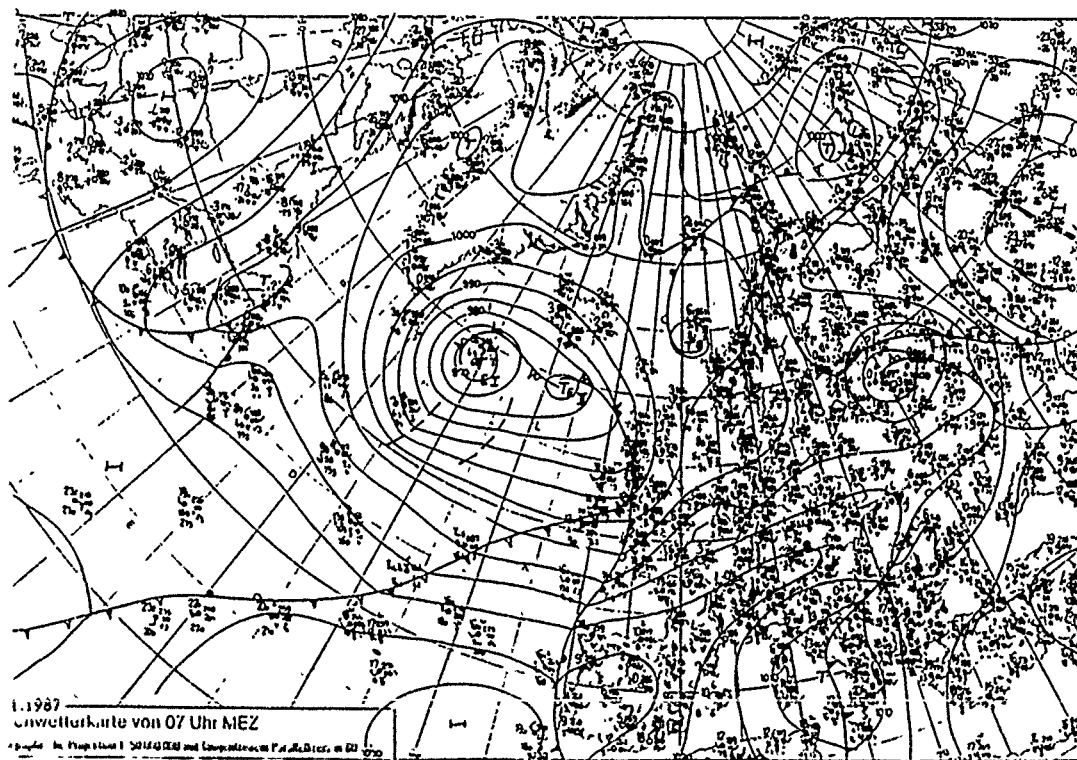


319

Sonntag, 15.11.1987



a)



b)

Fig. 3.04

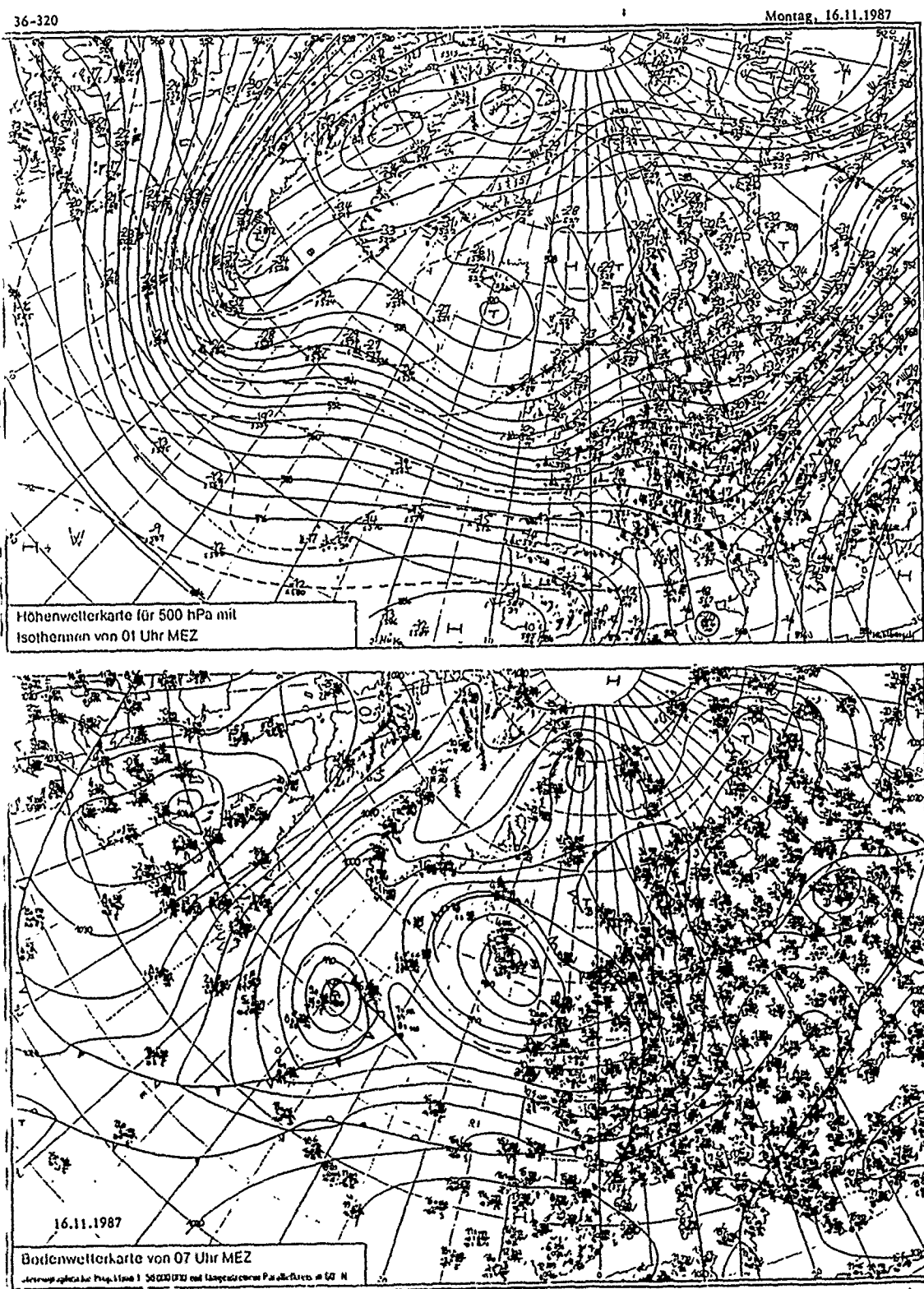
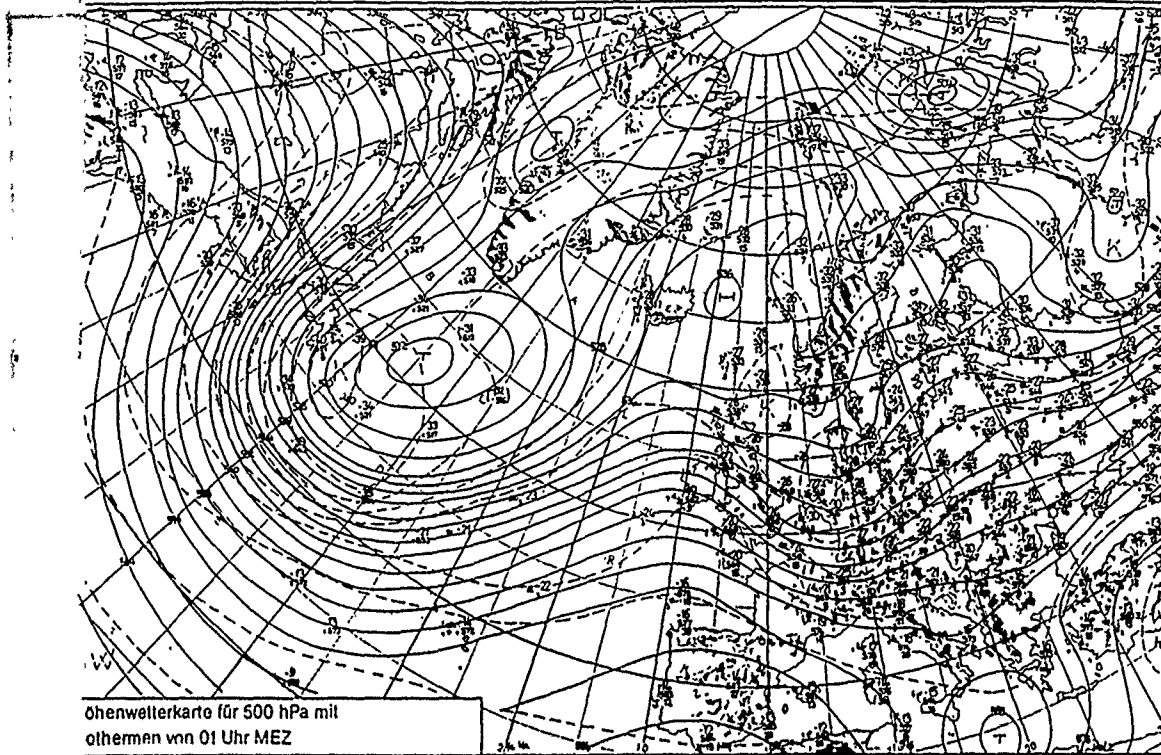
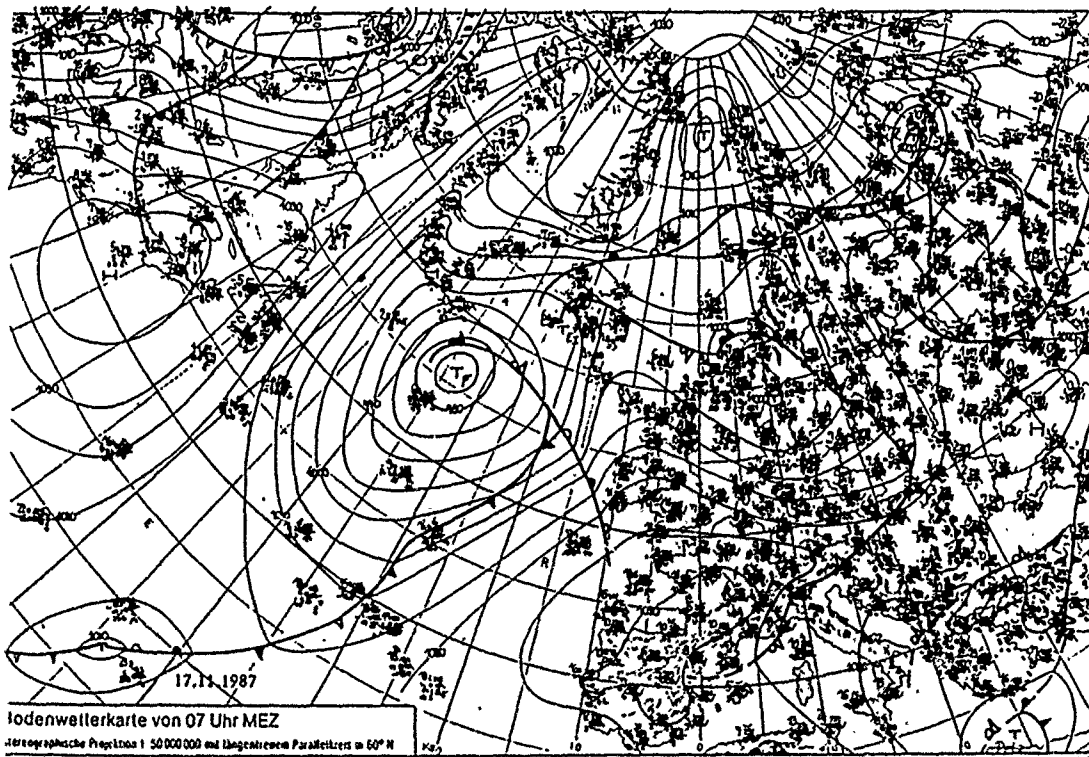


Fig. 3.05



500 hPa  
500 hPa



500 hPa

500 hPa

Fig. 3.06

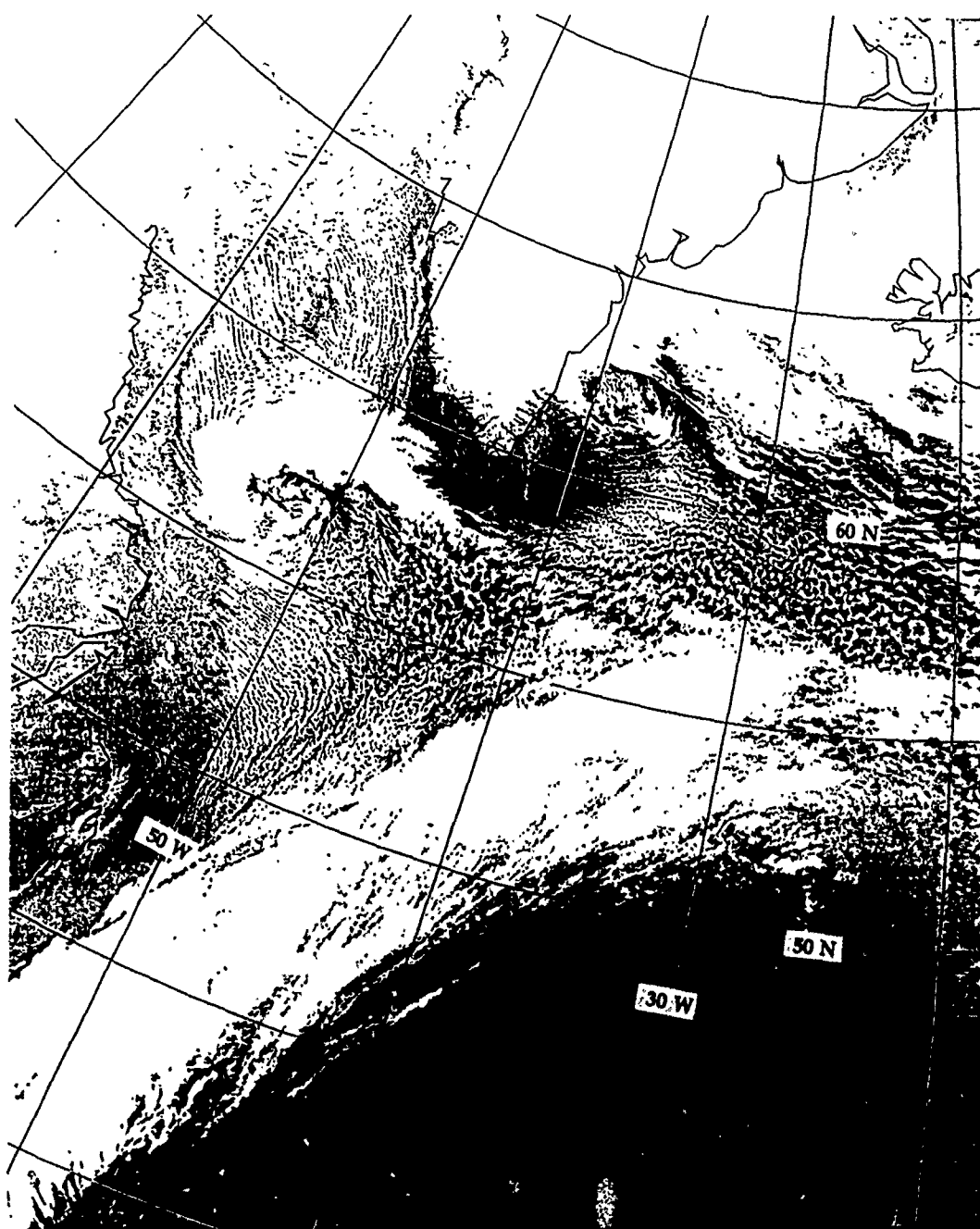


Fig. 3.07



Fig. 3.08

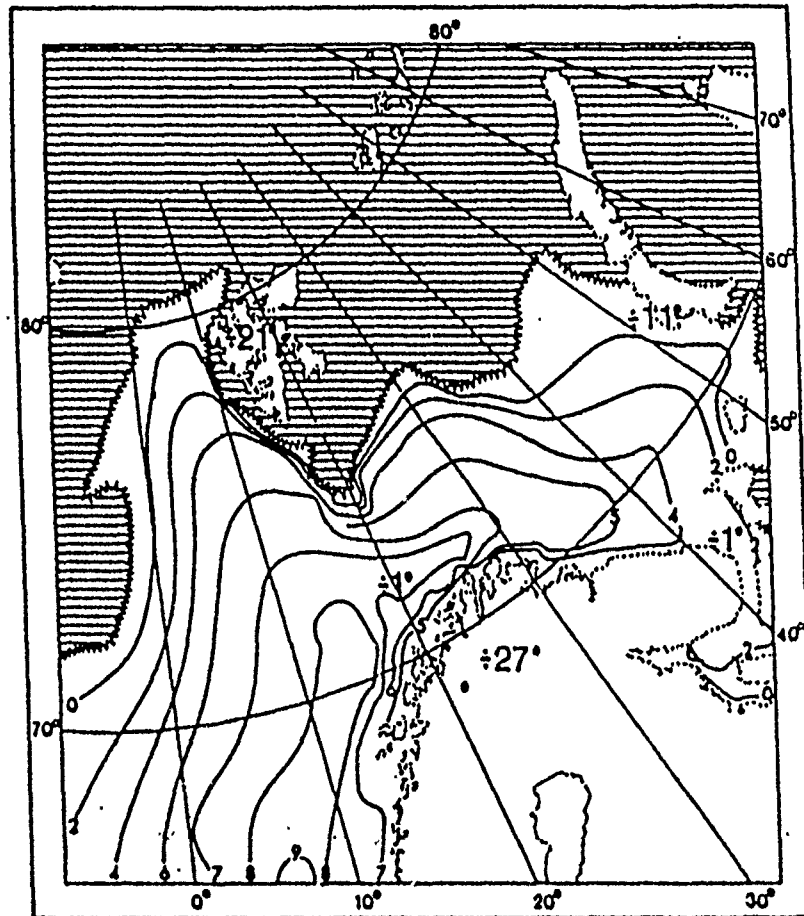


Fig. 4.01



Fig. 4.02



Fig. 4.03





Fig. 4.04





Fig. 4.06

**Fig. 4.07**

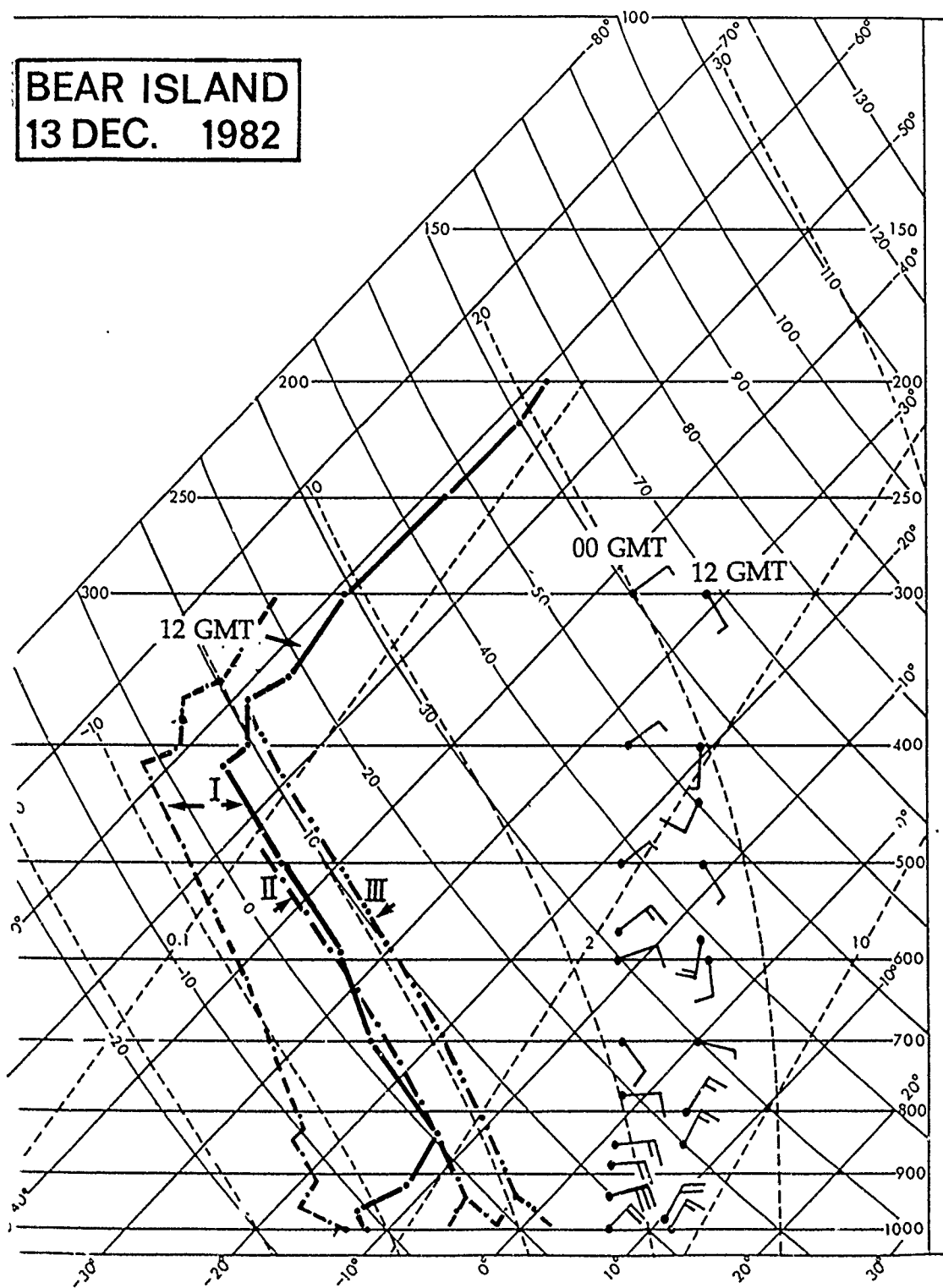


Fig. 4.08

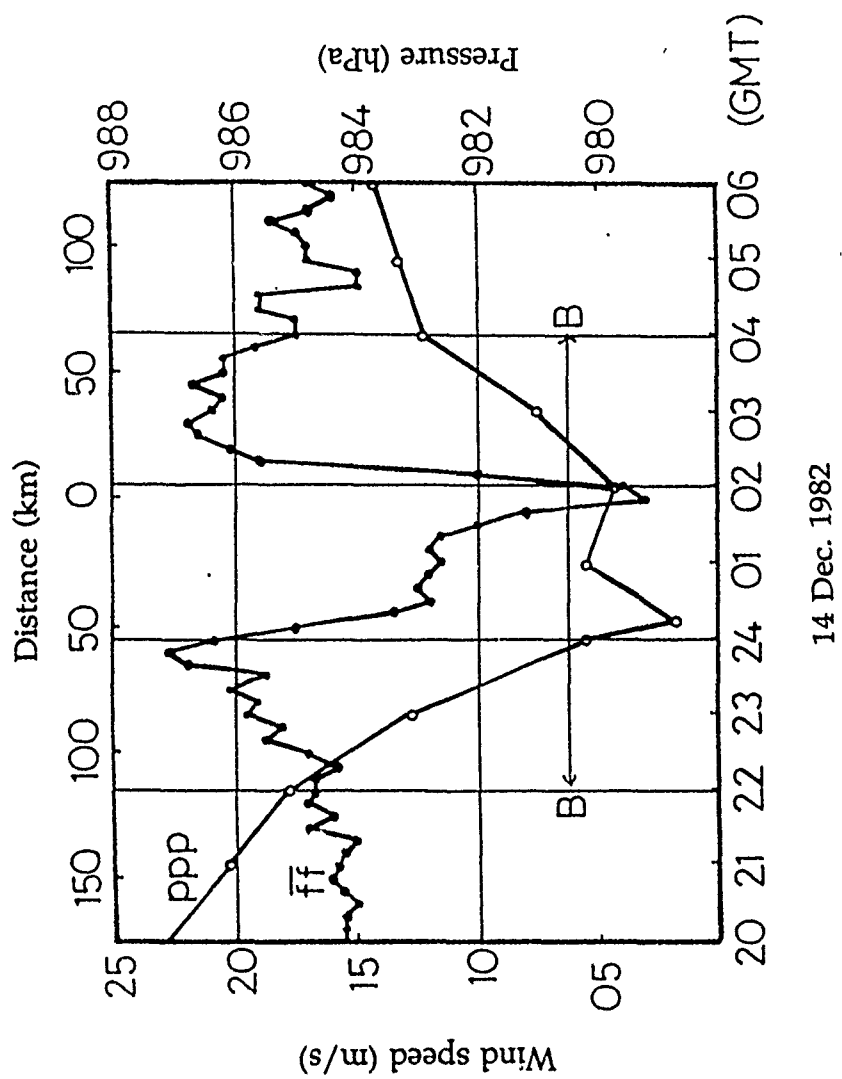


Fig. 4.09



Fig. 4.10a



Fig. 4.10b



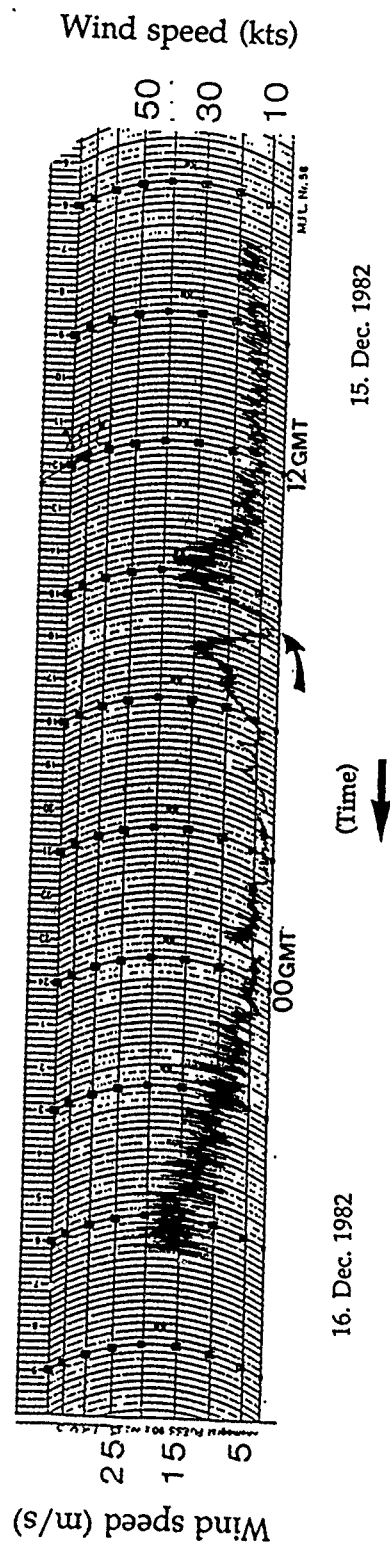


Fig. 4.11



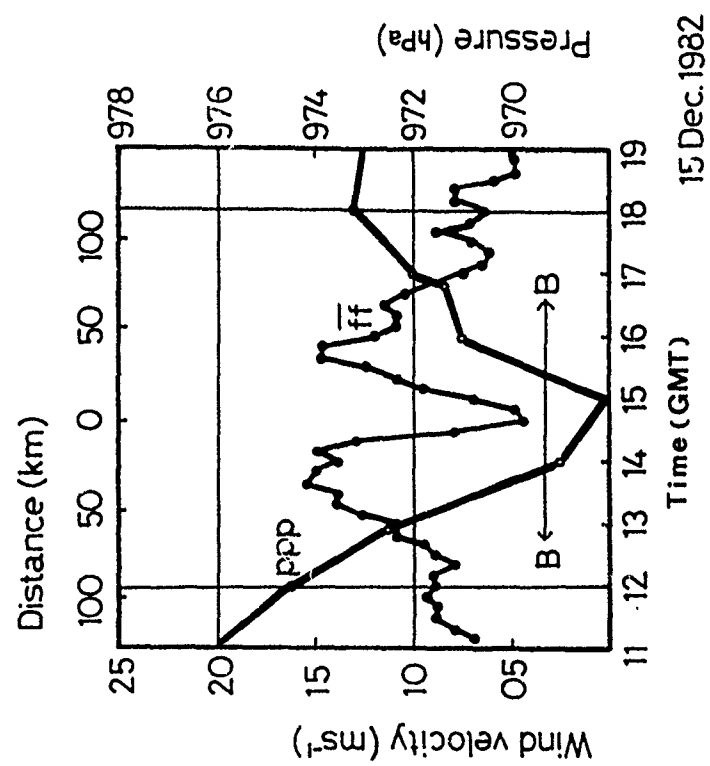


Fig. 4.13



Fig. 4.14



Fig. 4.15

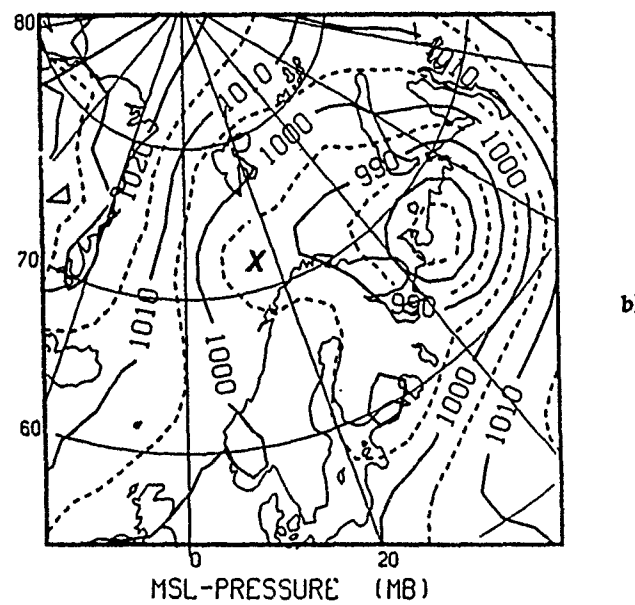
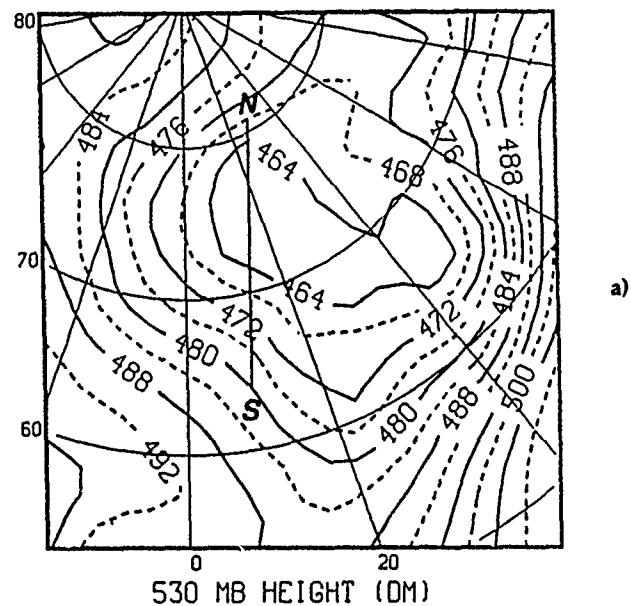


Fig. 5.01

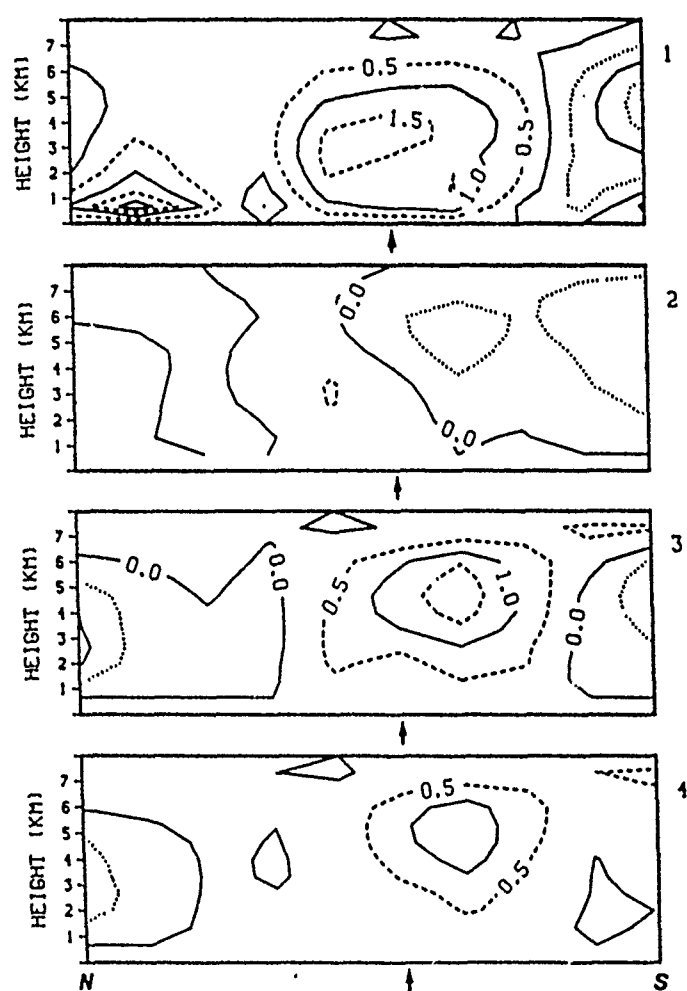


Fig. 5.02

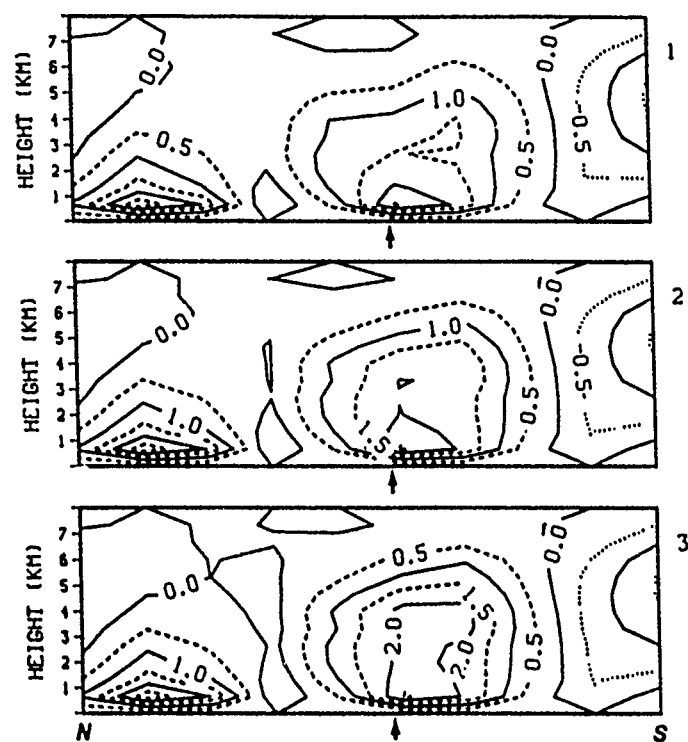


Fig. 5.03



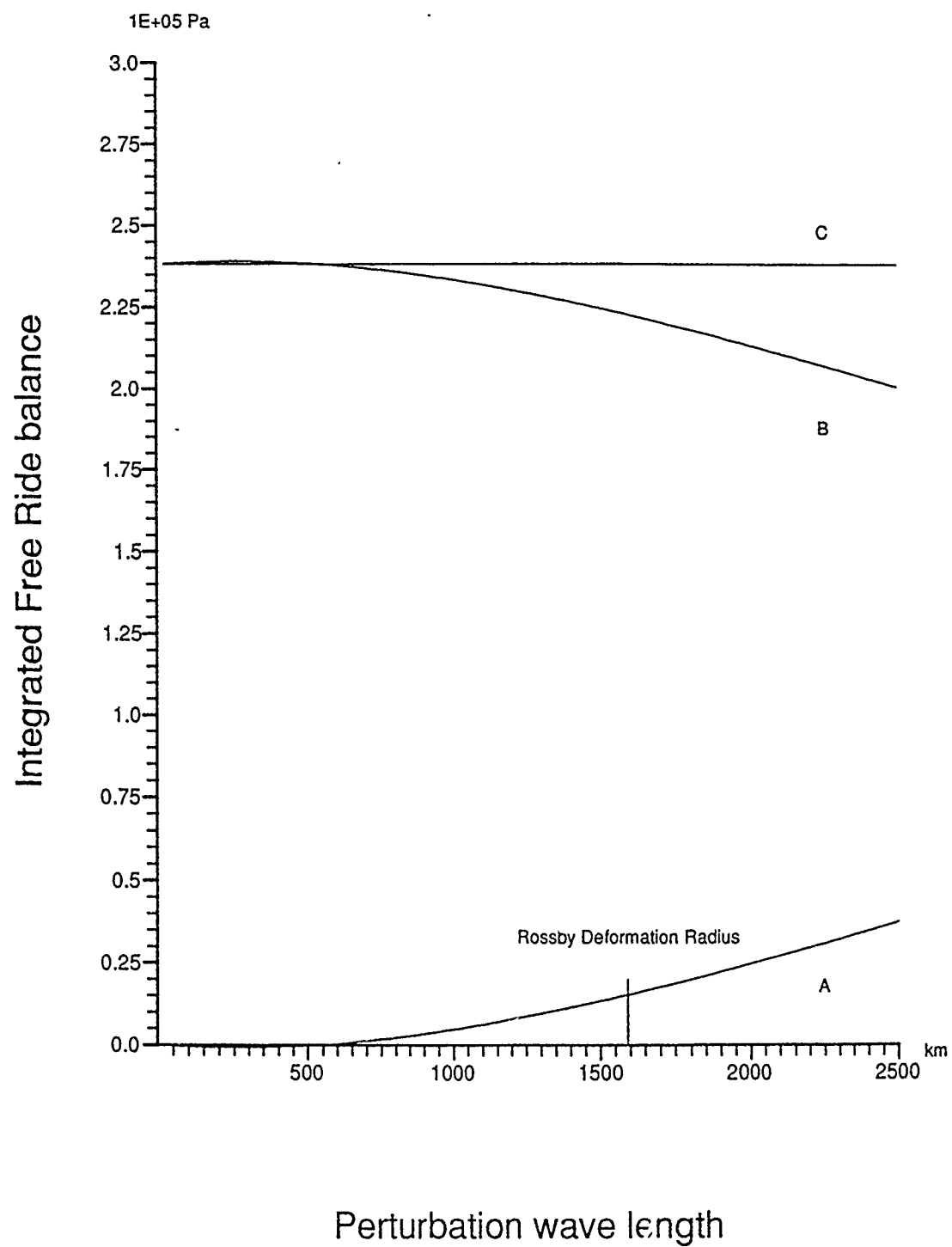


Fig. 5.04

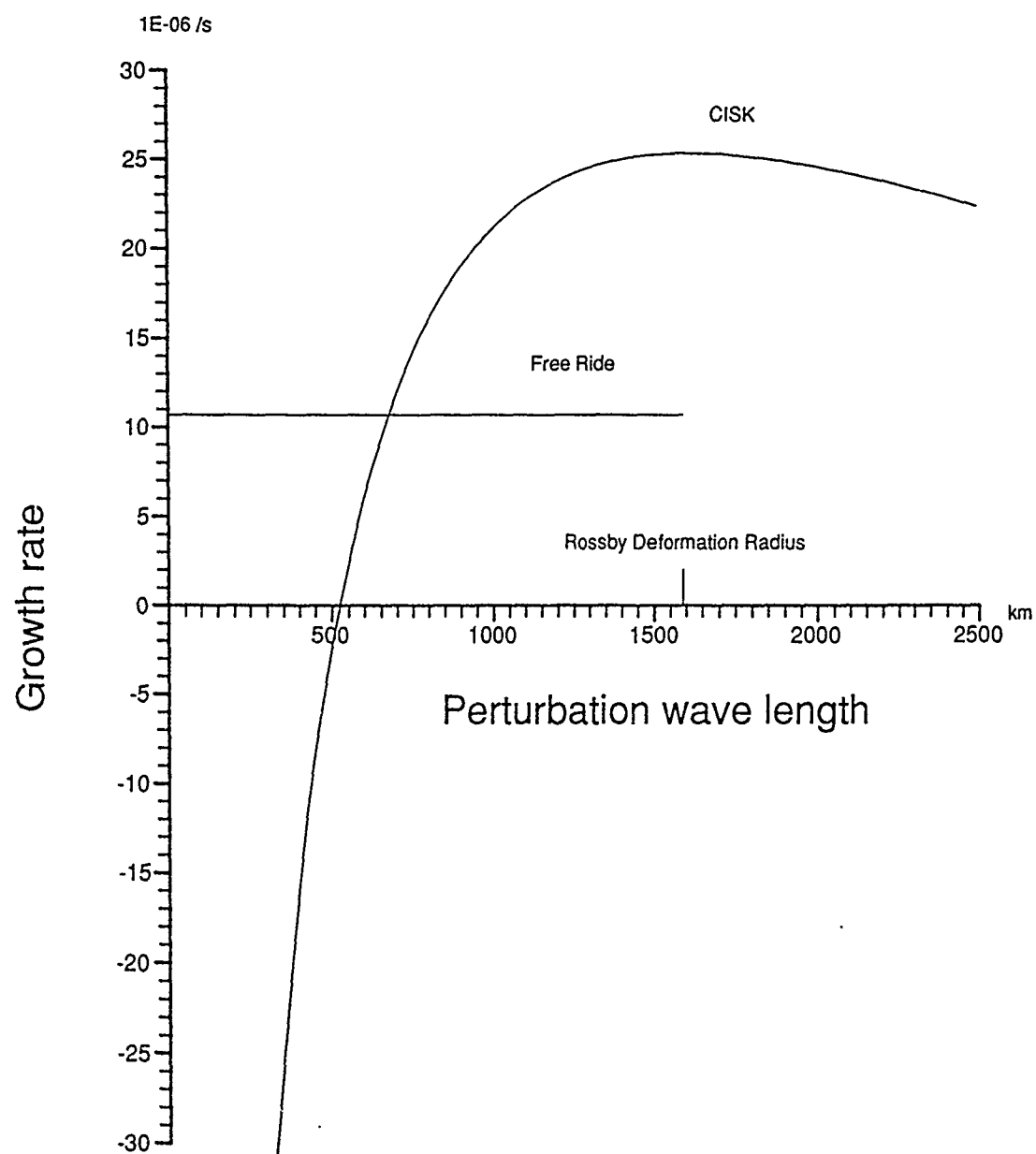


Fig. 5.05

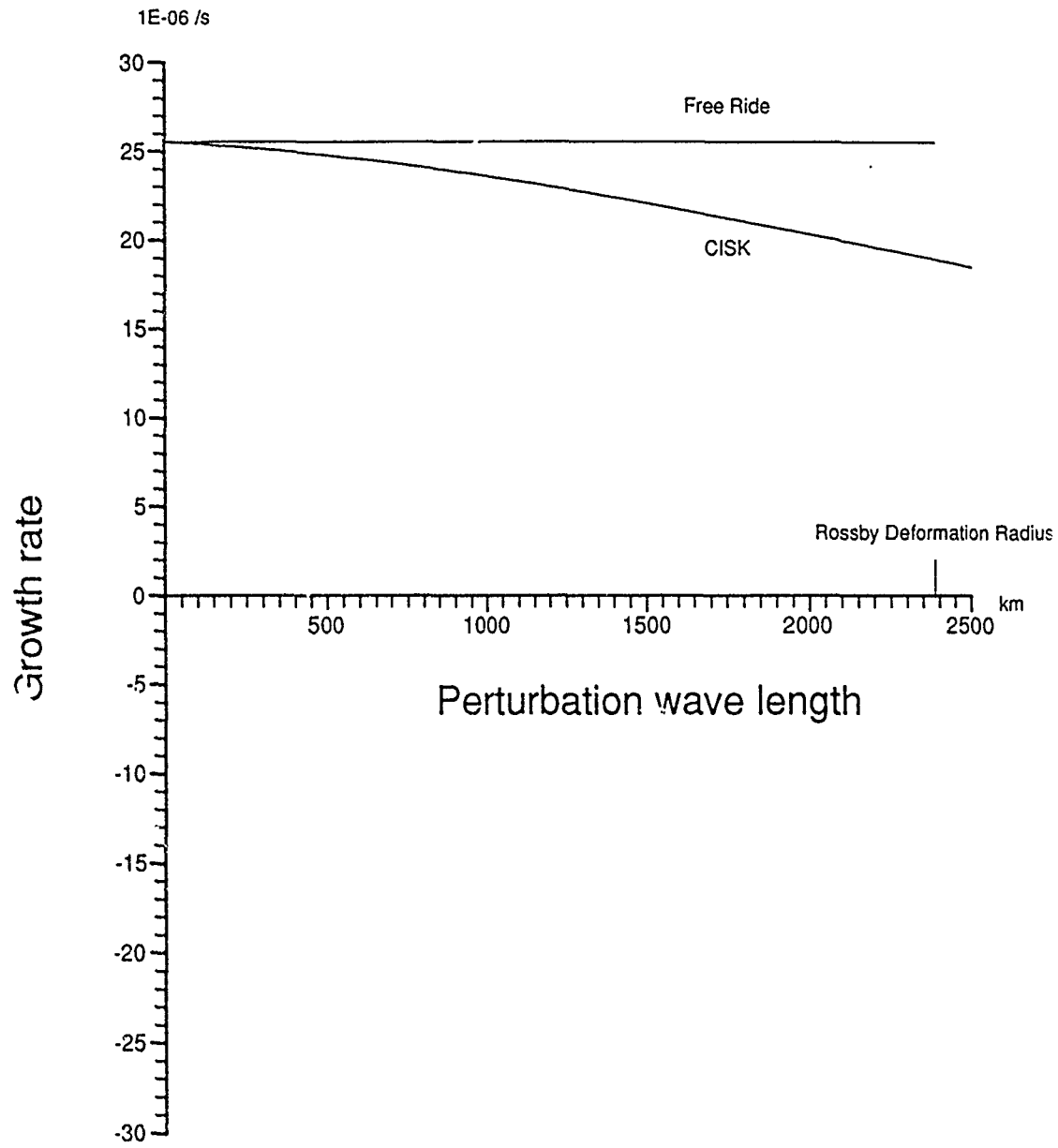
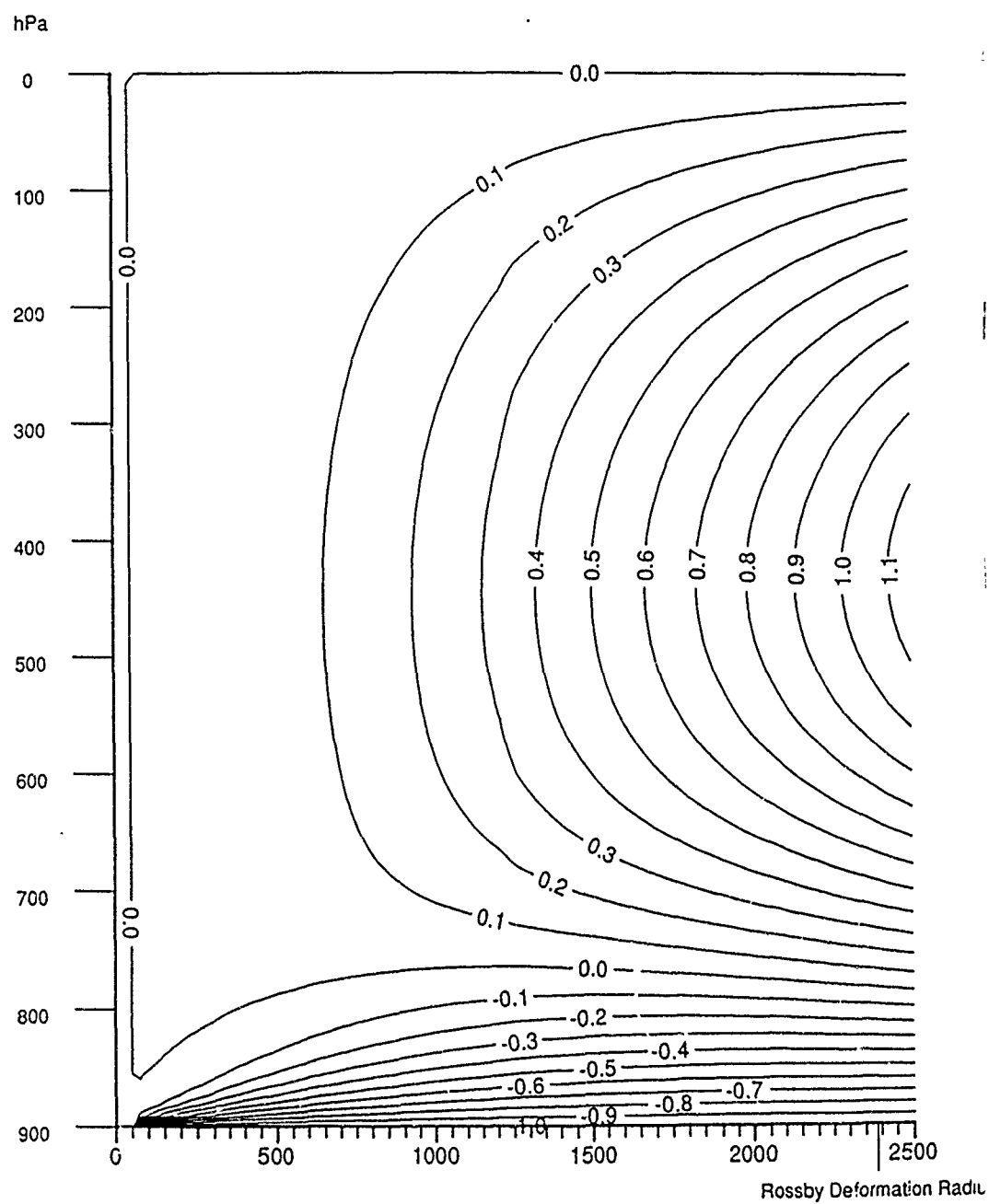
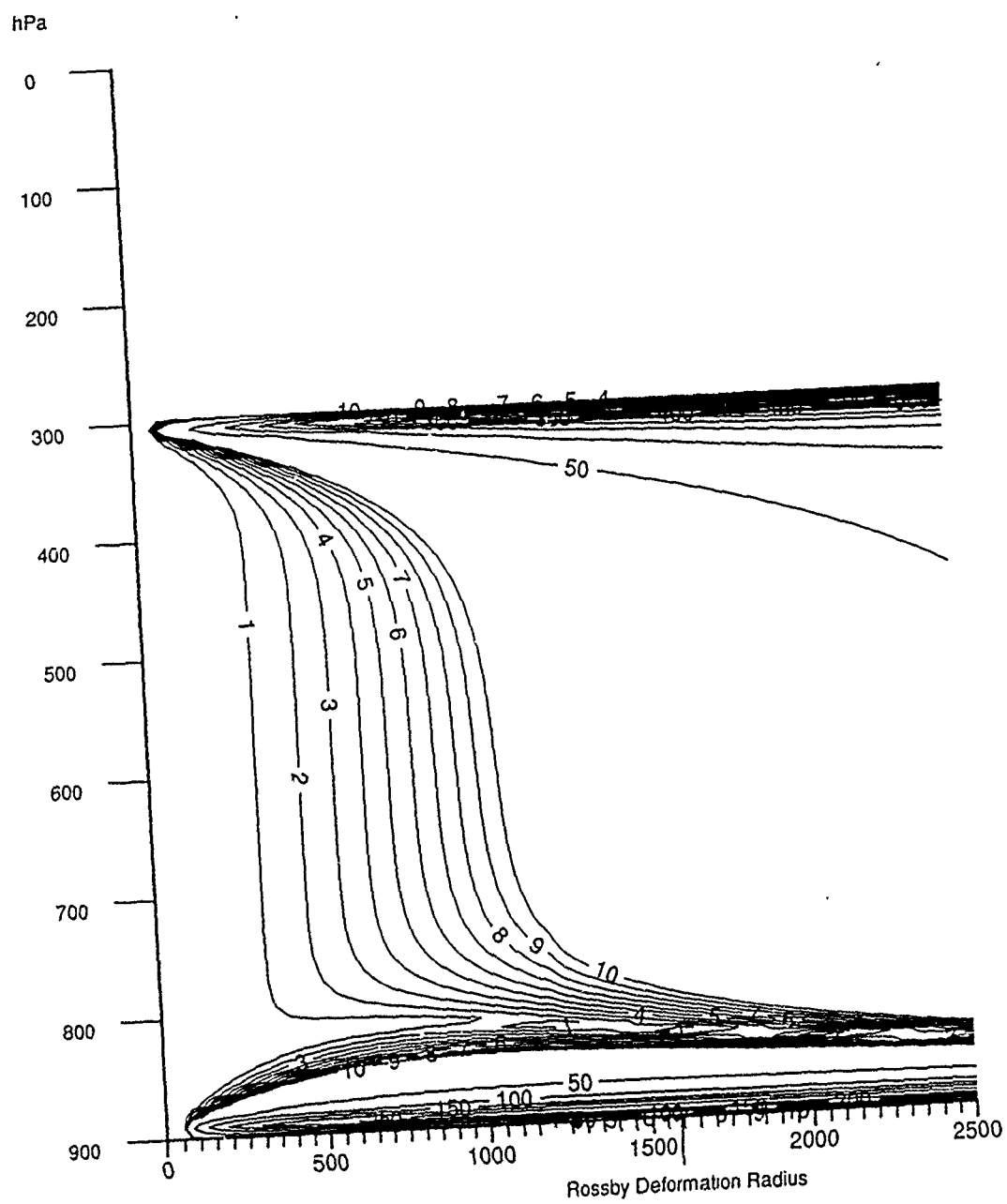


Fig. 5.06



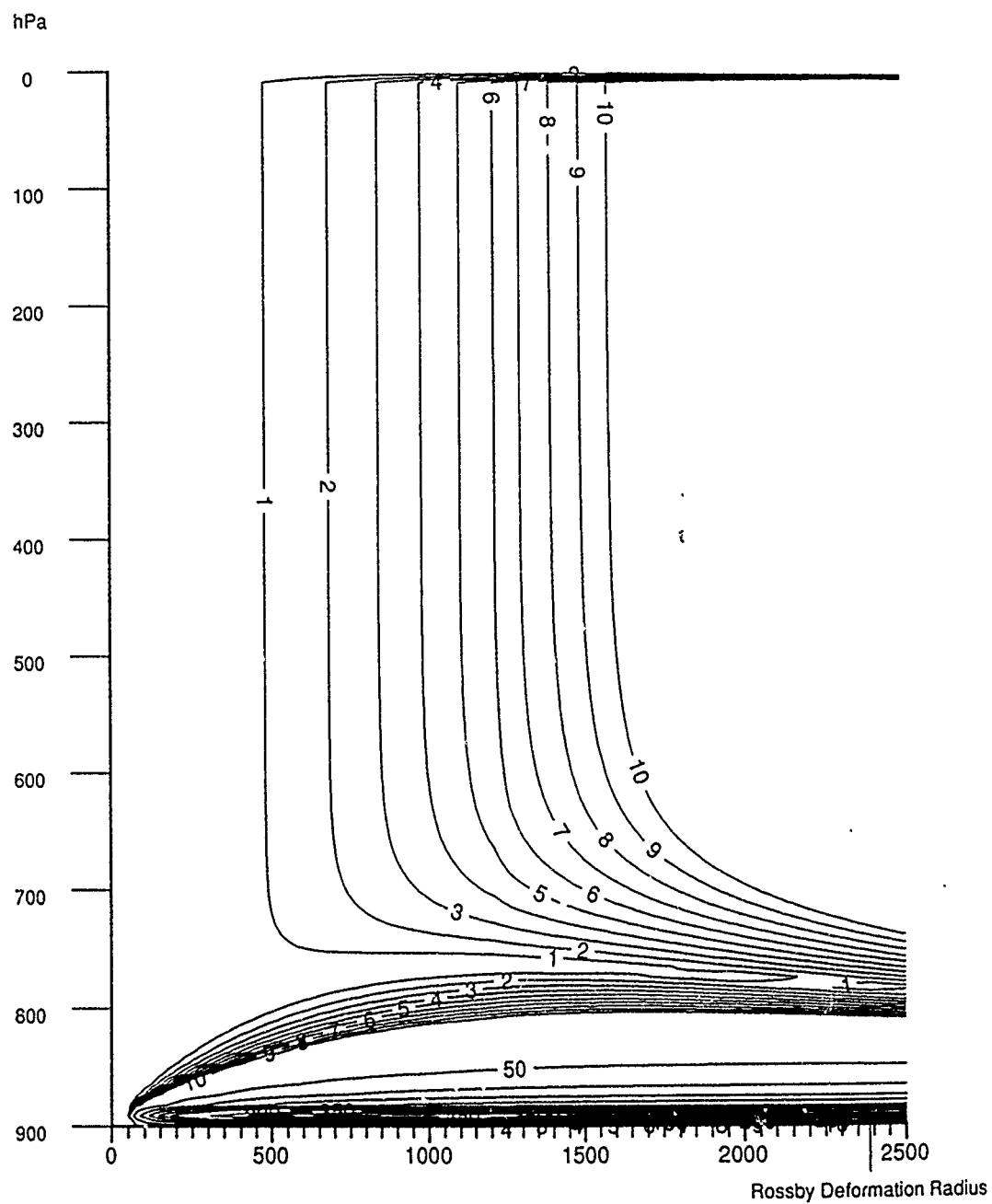
Perturbation wave length

Fig. 5.07



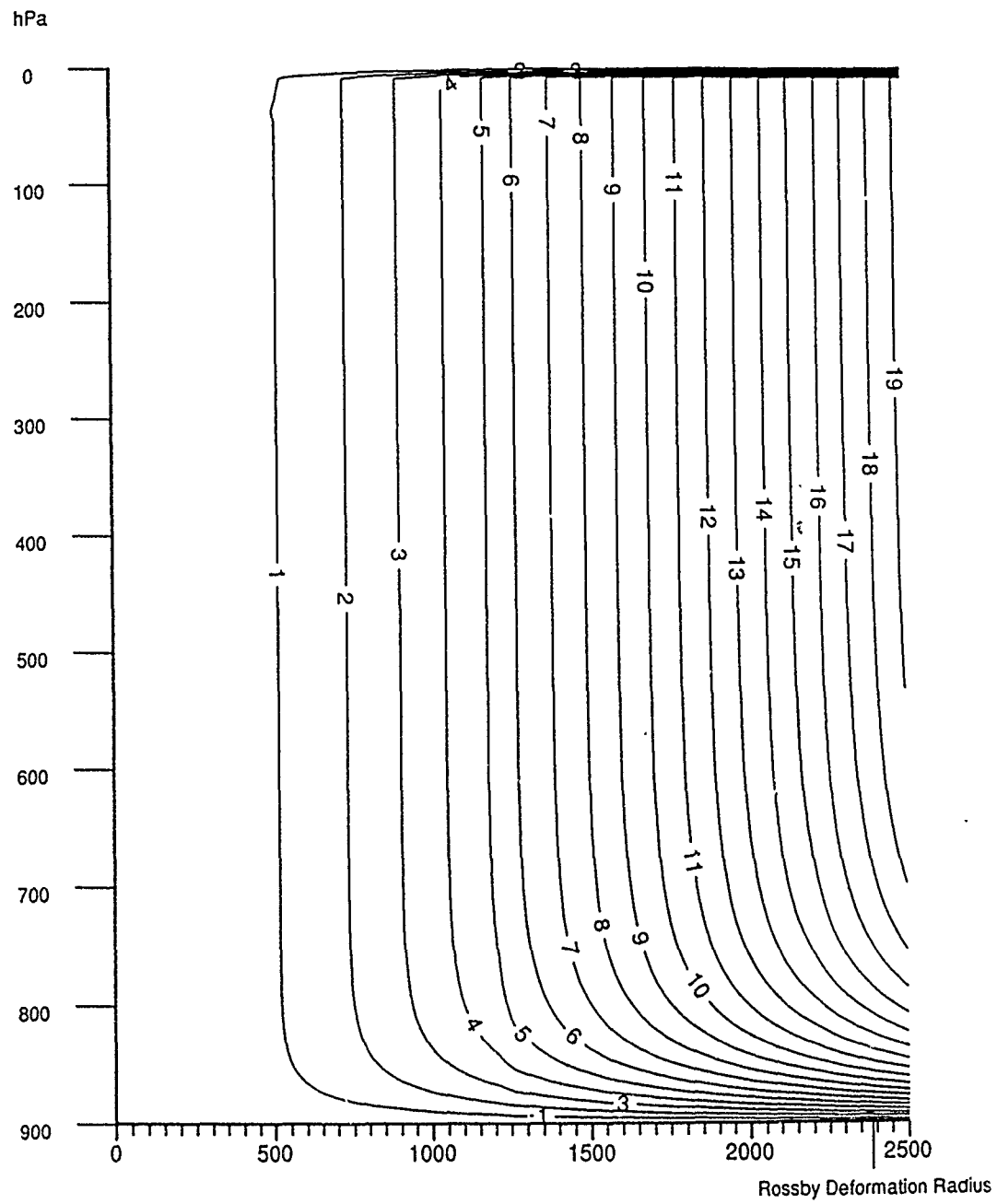
Perturbation wave length

Fig. 5.08a



Perturbation wave length

Fig 5.08b



Perturbation wave length

Fig. 5.09

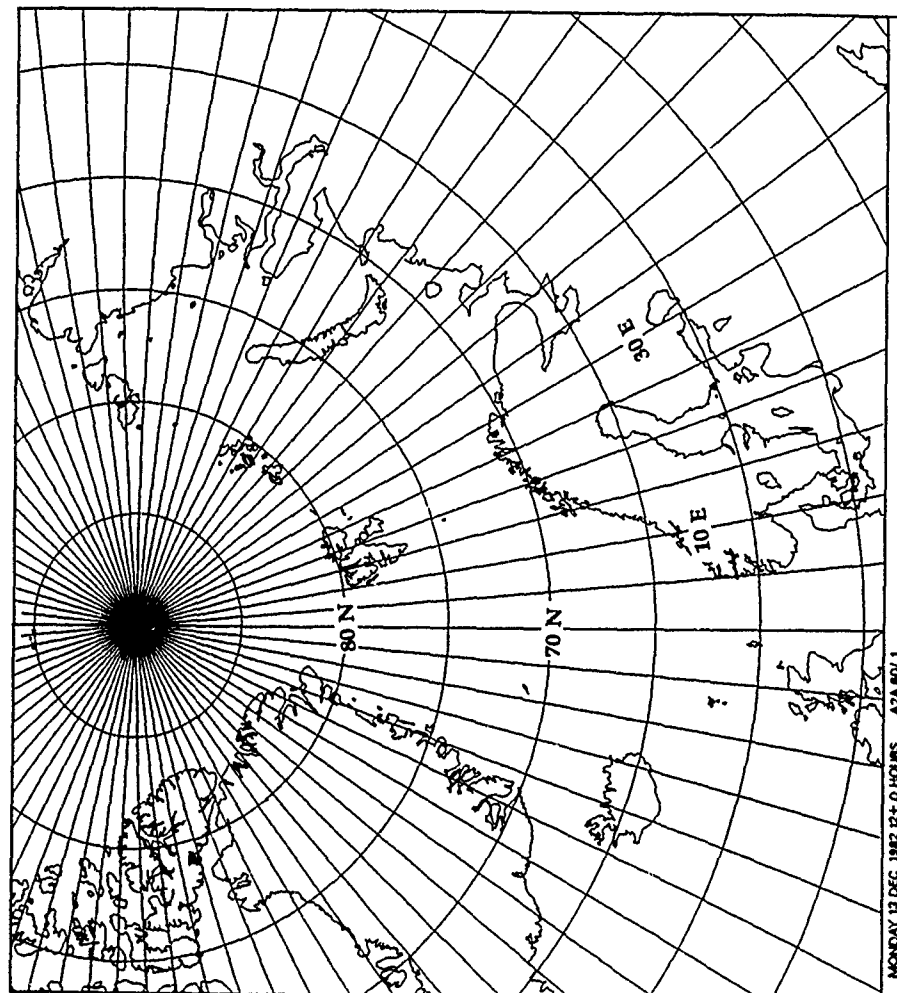


Fig. 5.10



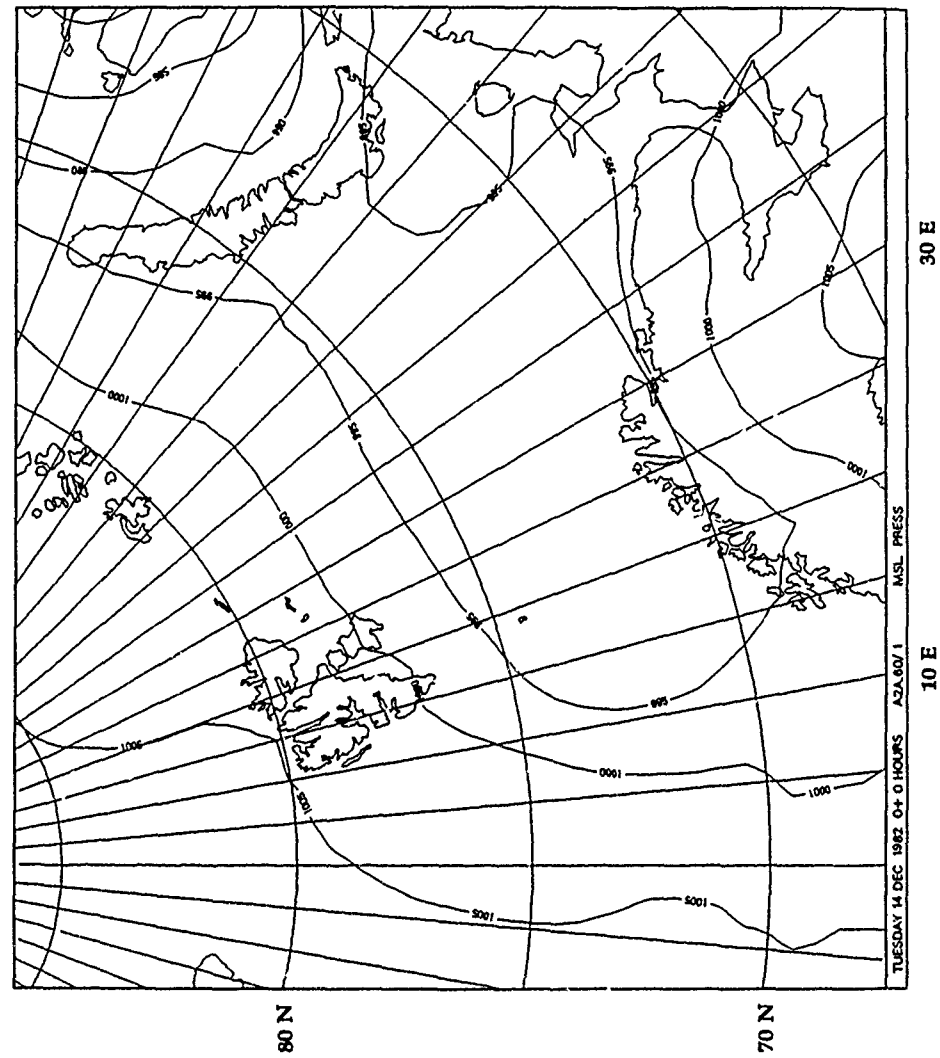


Fig. 5.11

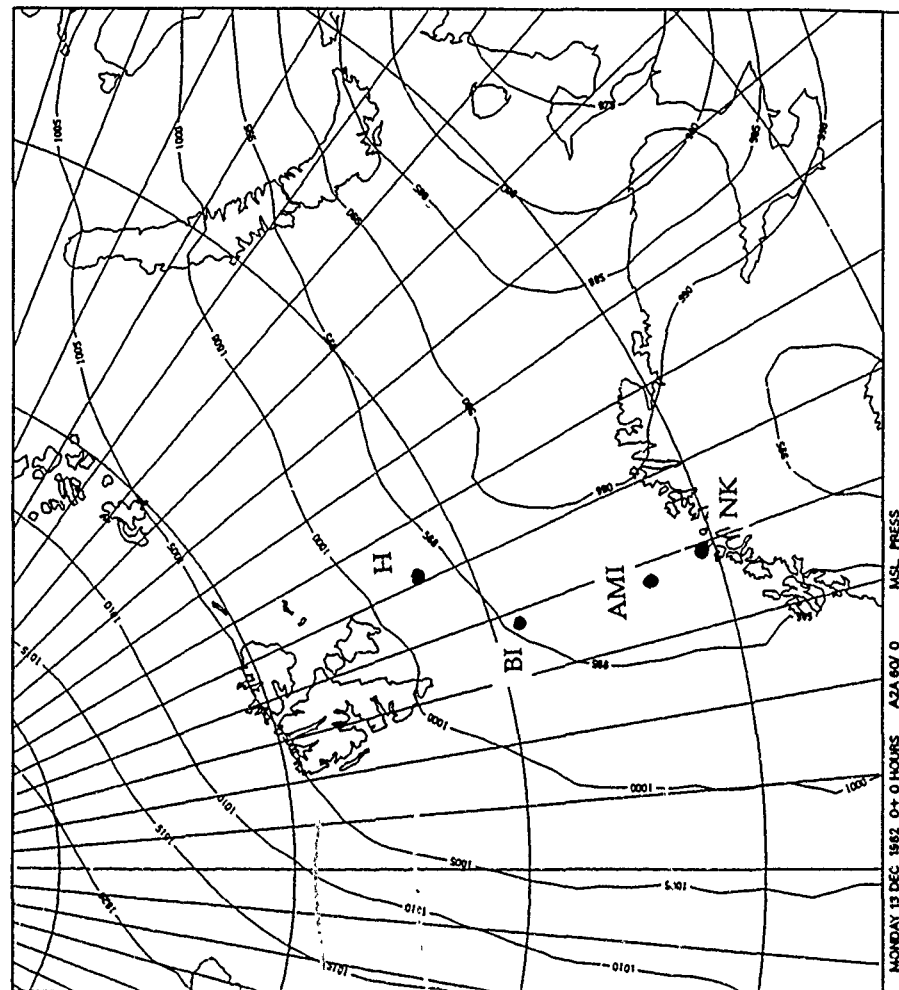


Fig. 5.12a

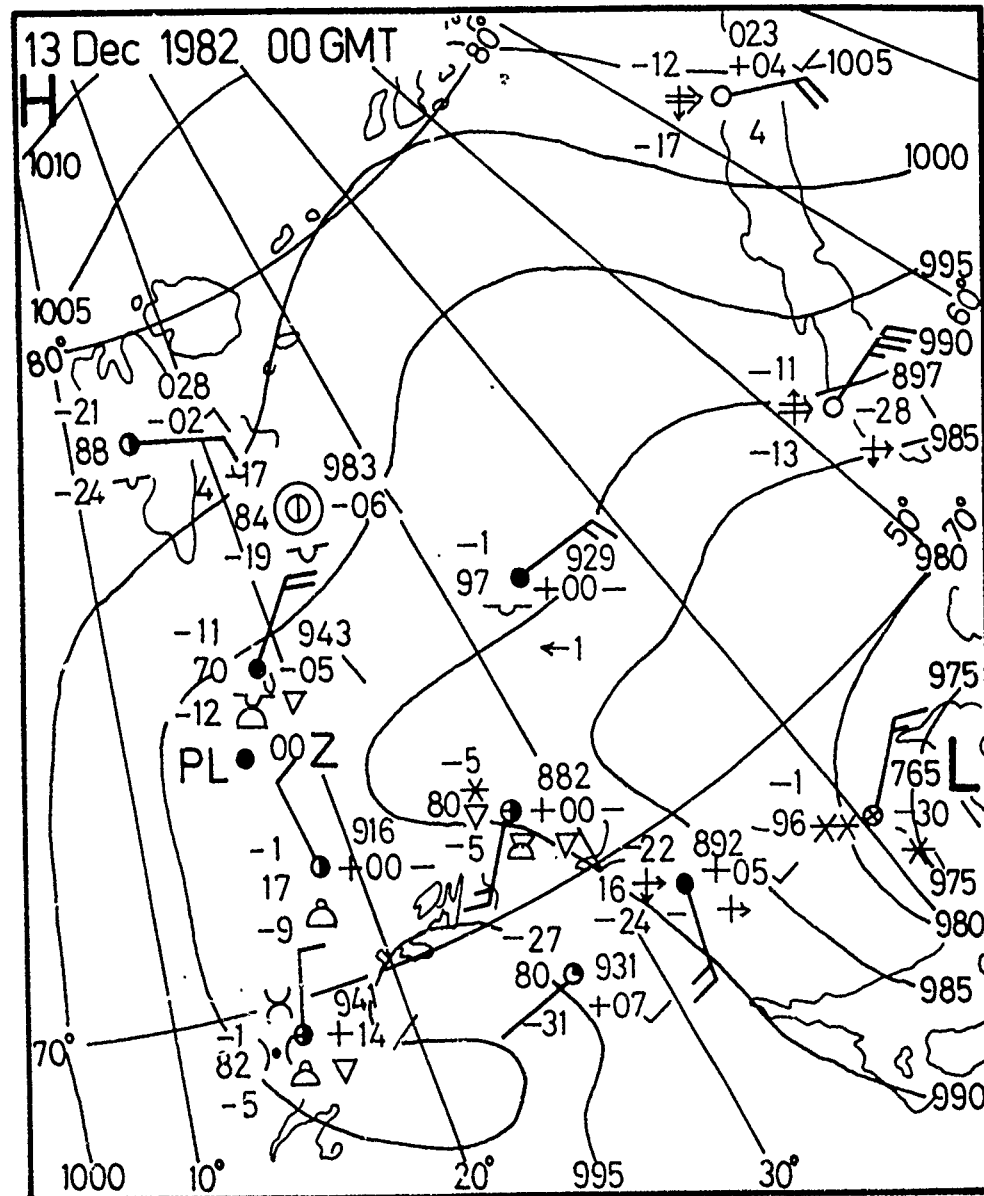


Fig. 5.12b

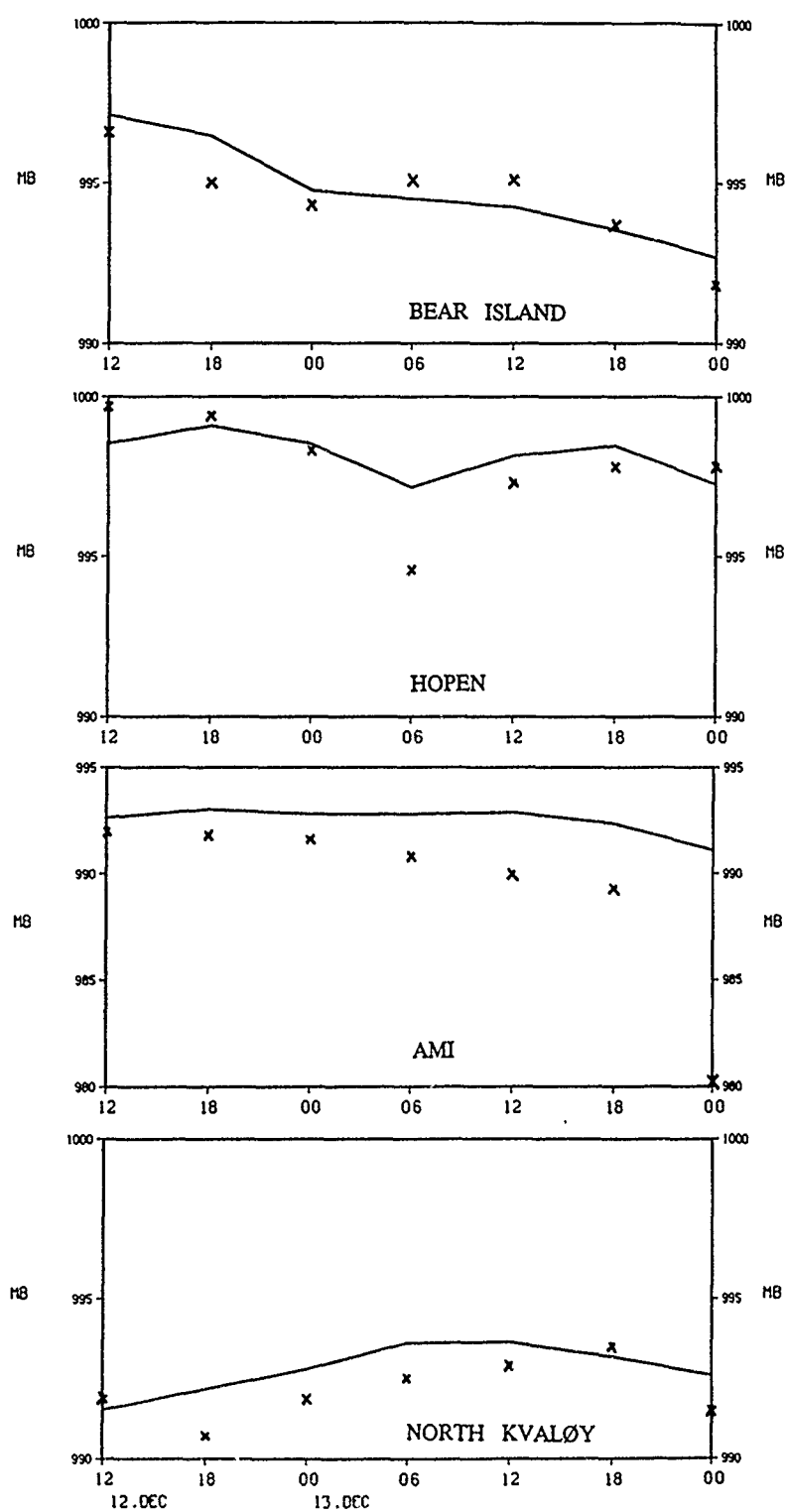


Fig. 5.13

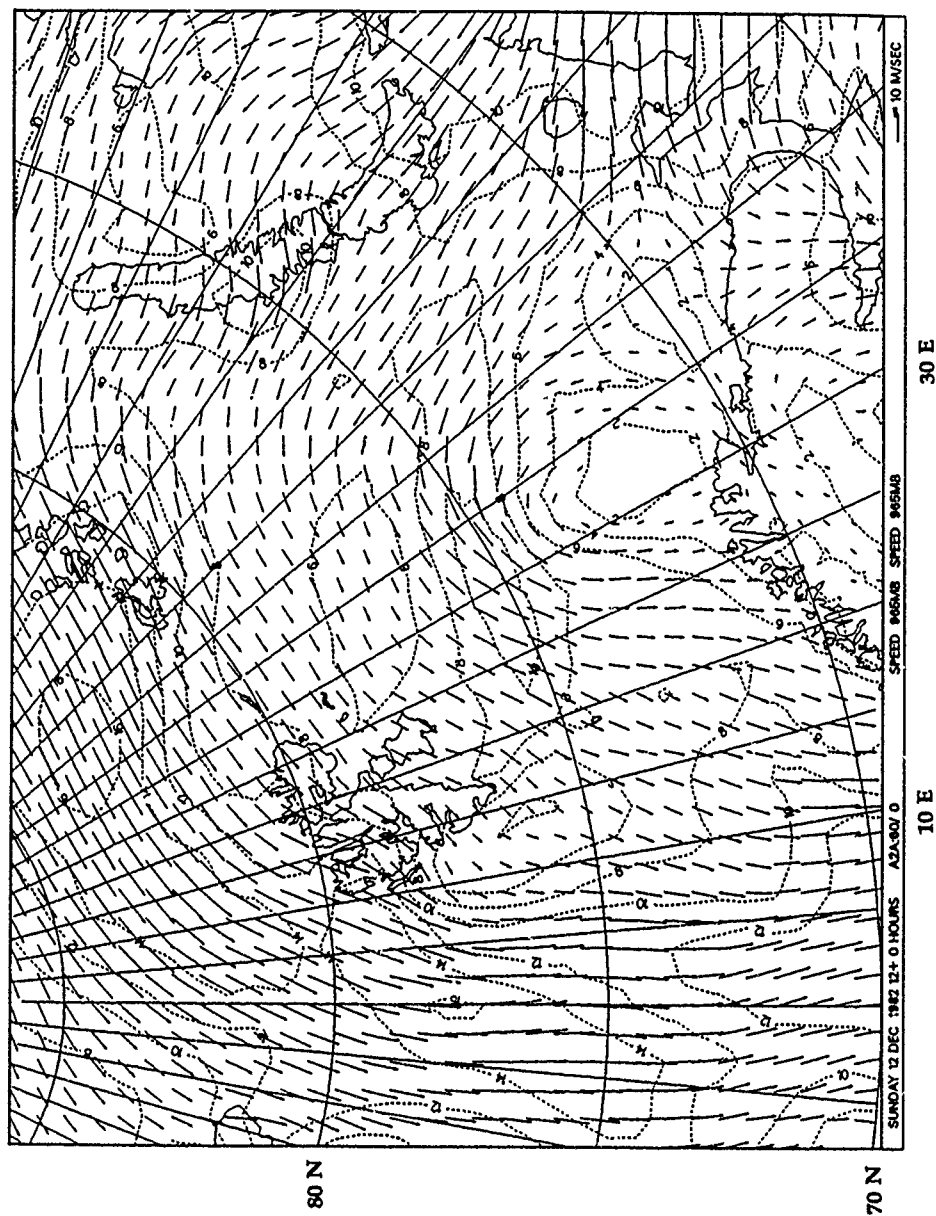
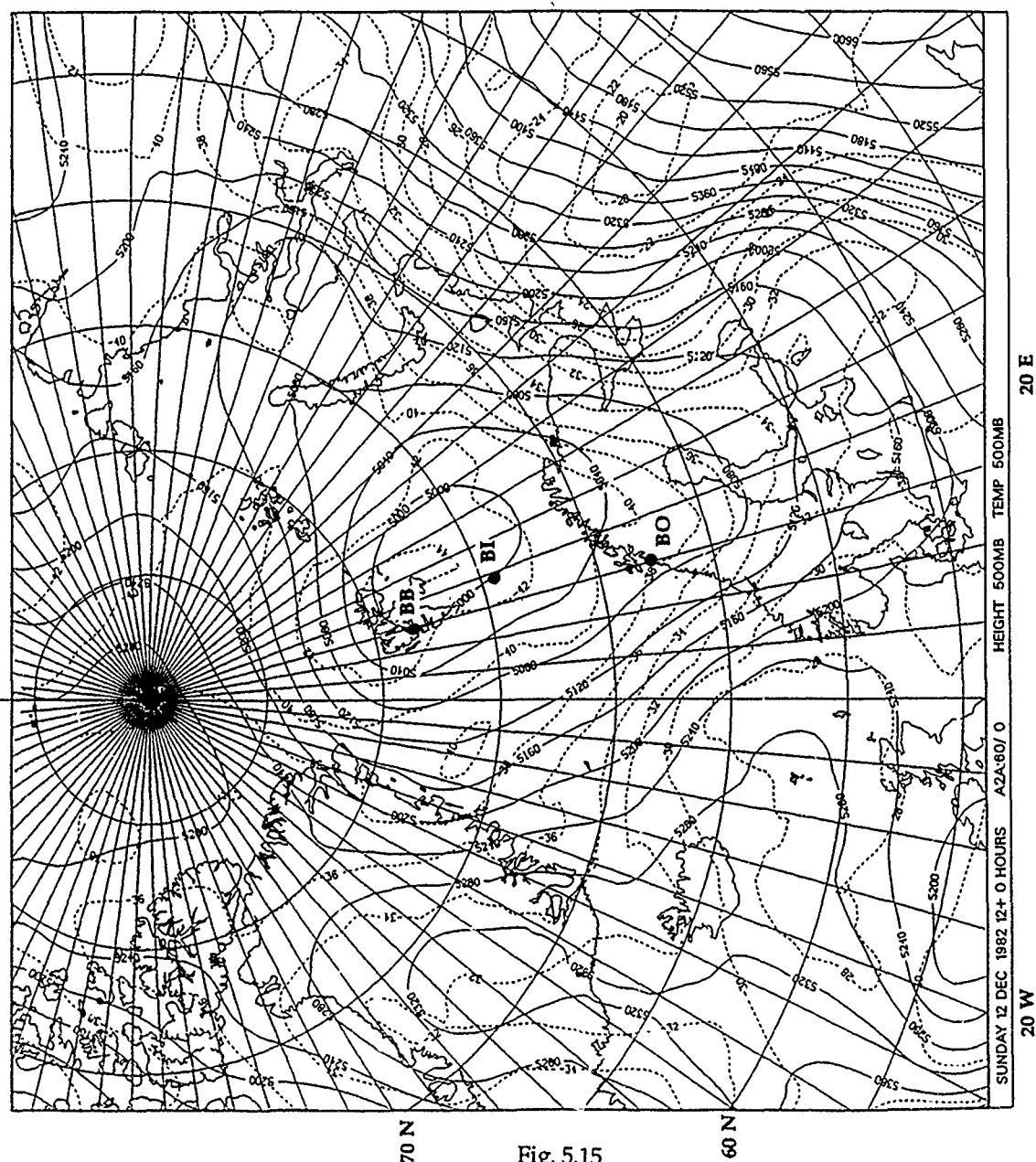


Fig. 5.14



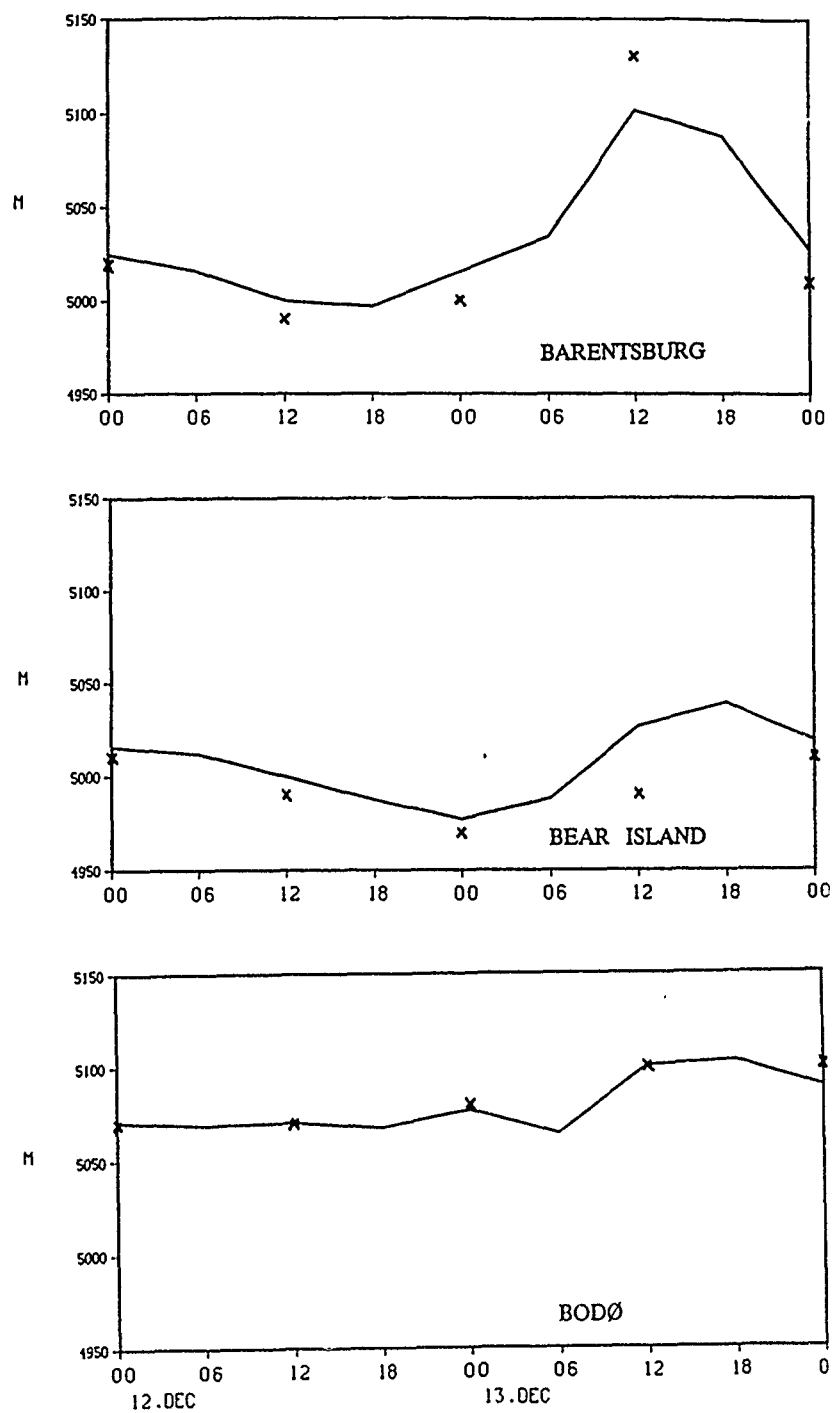


Fig. 5.16

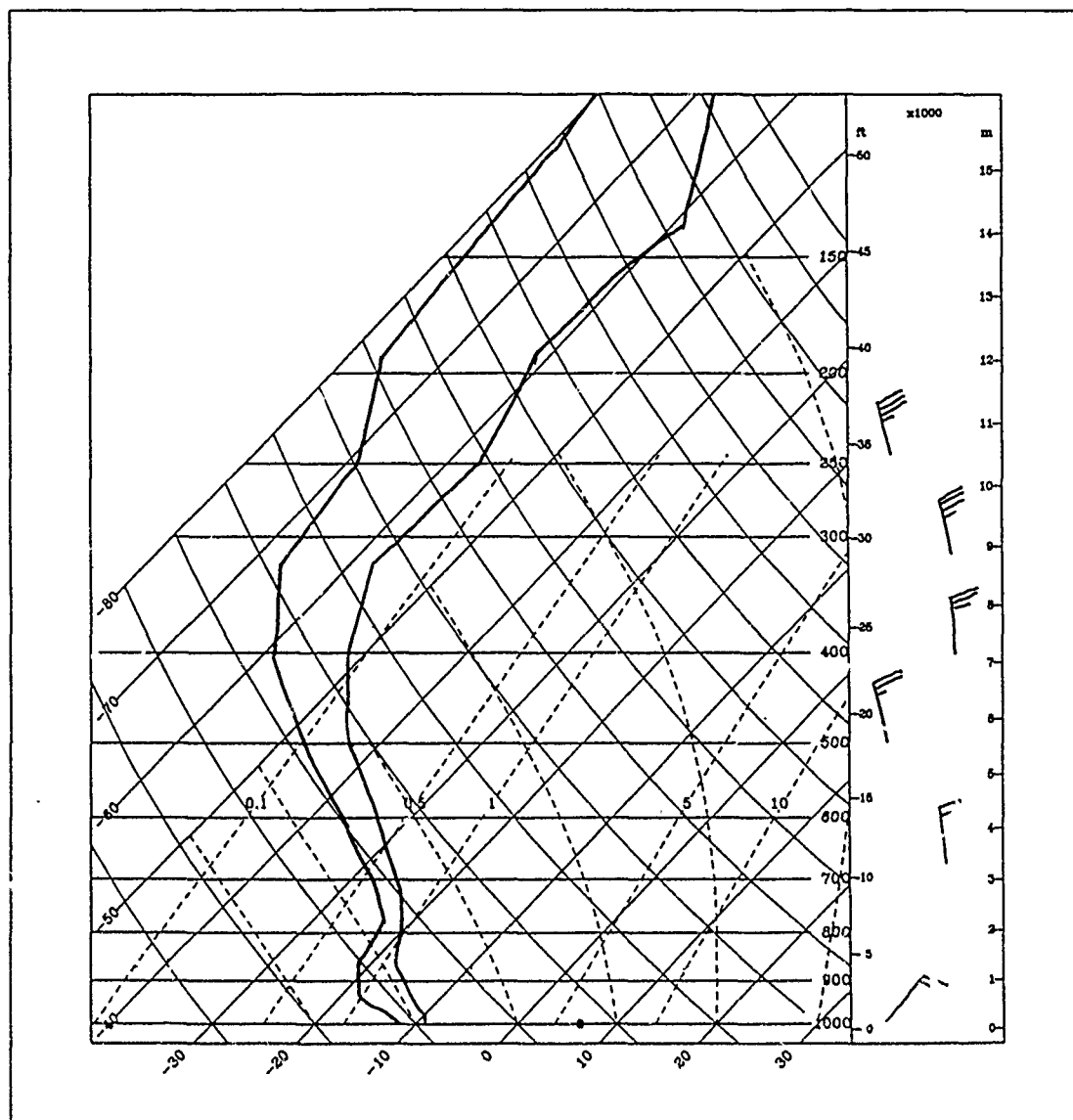


Fig. 5.17a



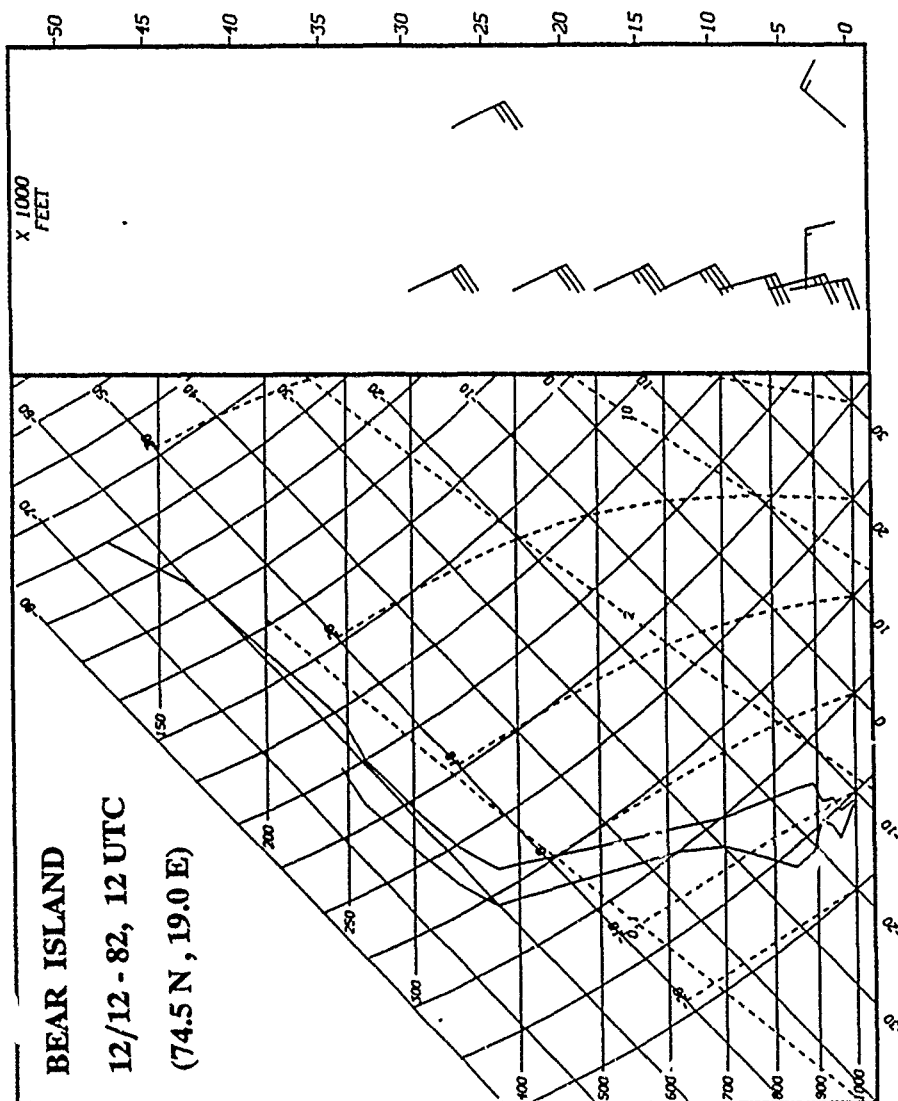
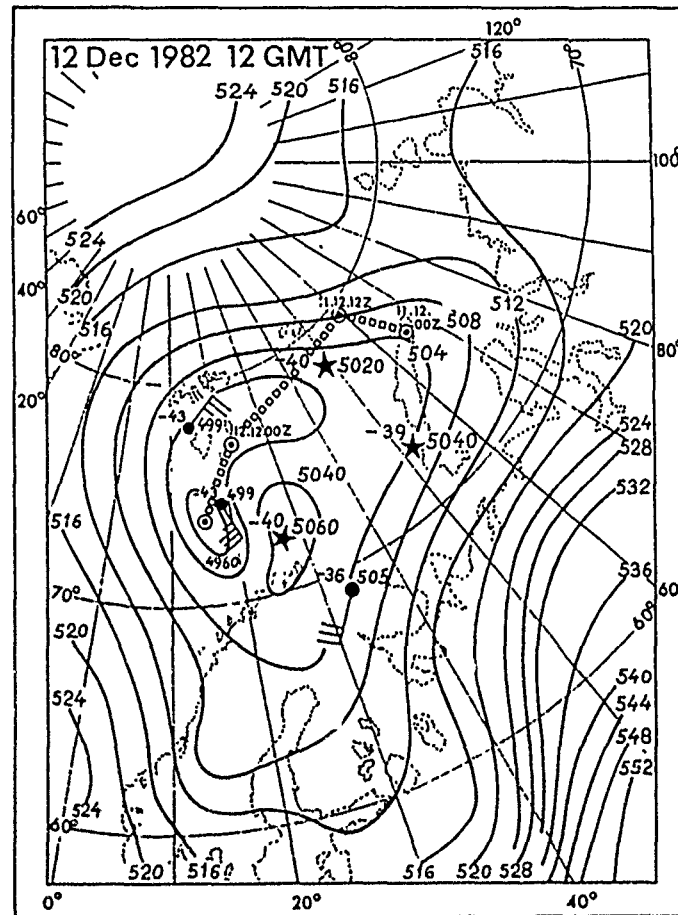


Fig. 5.17b



**Fig. 5.18**

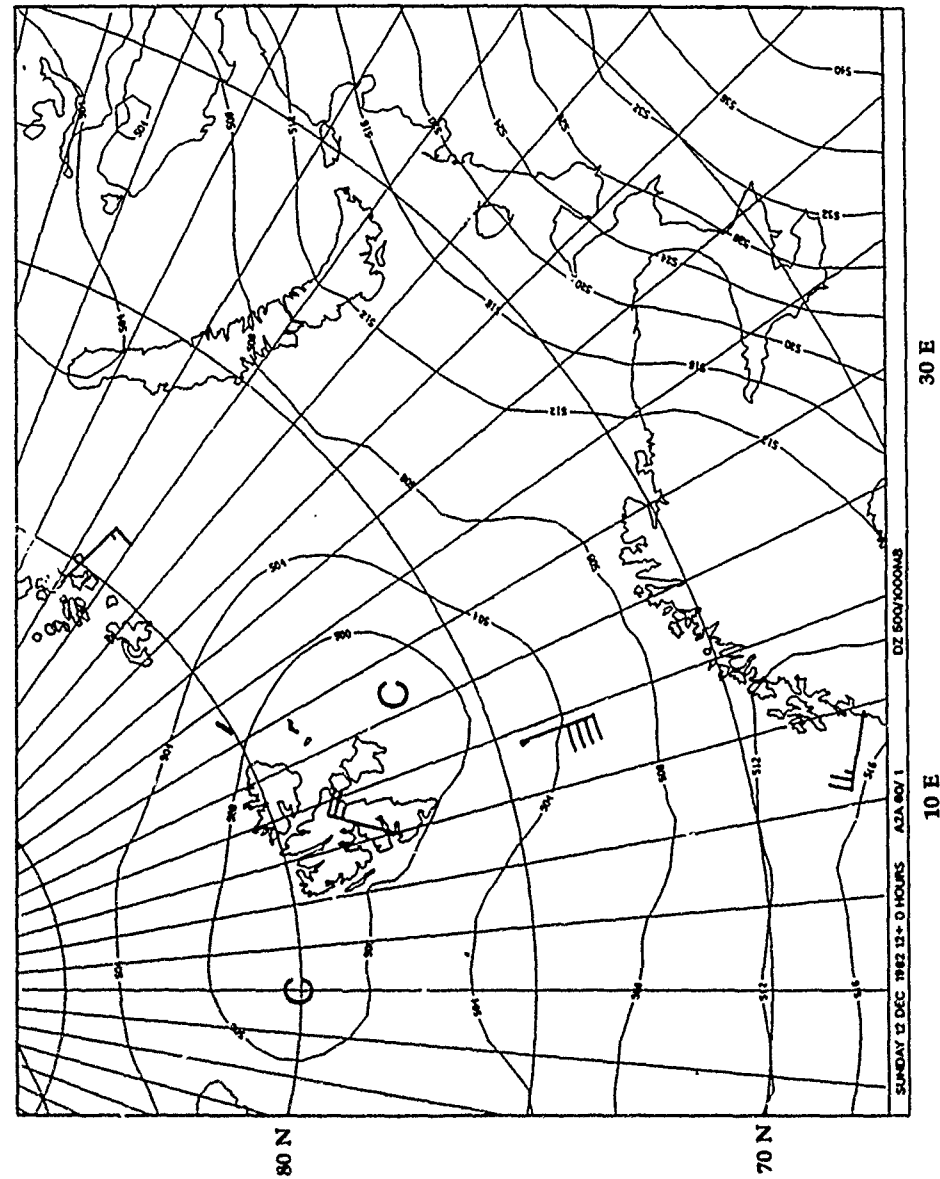


Fig. 5.19

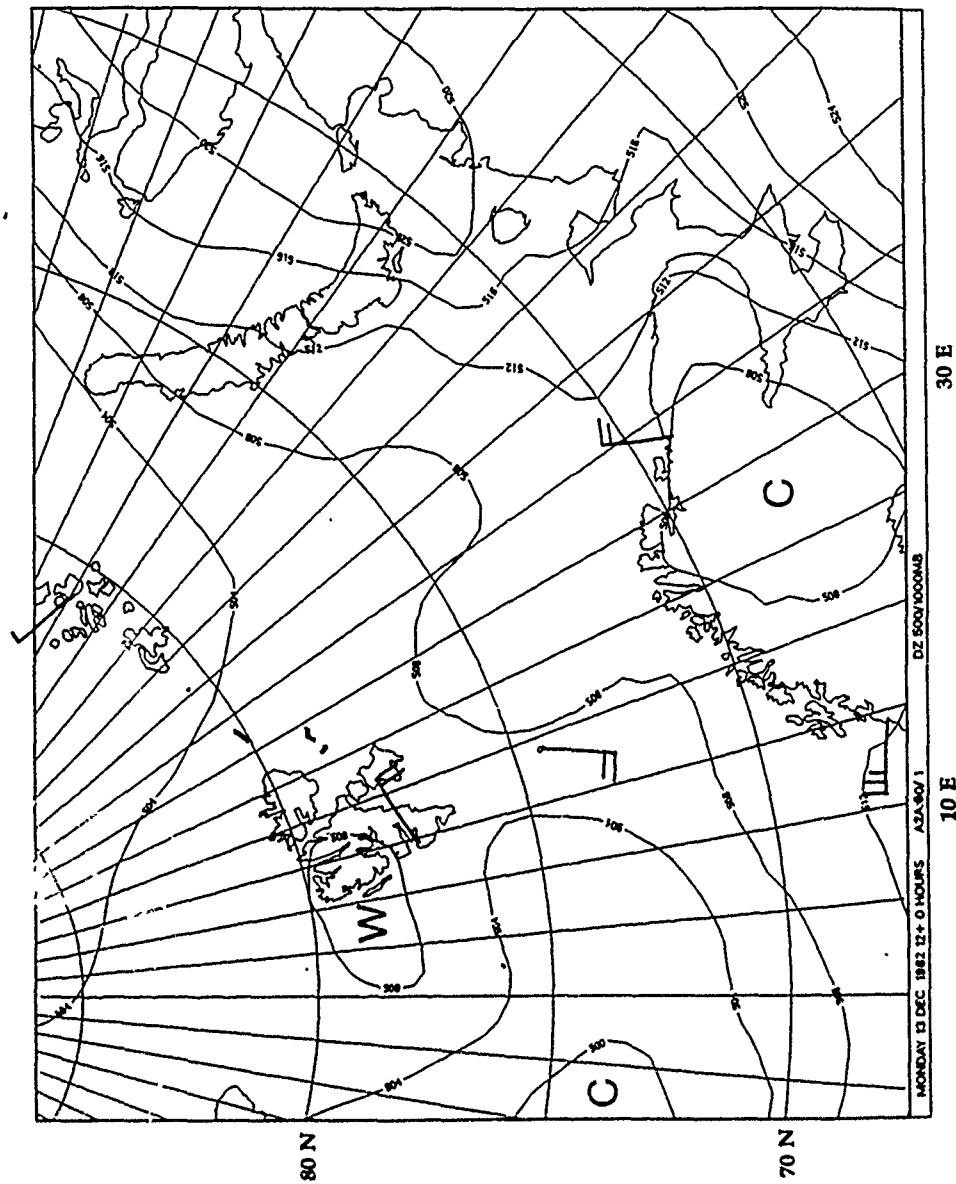


Fig. 5.20

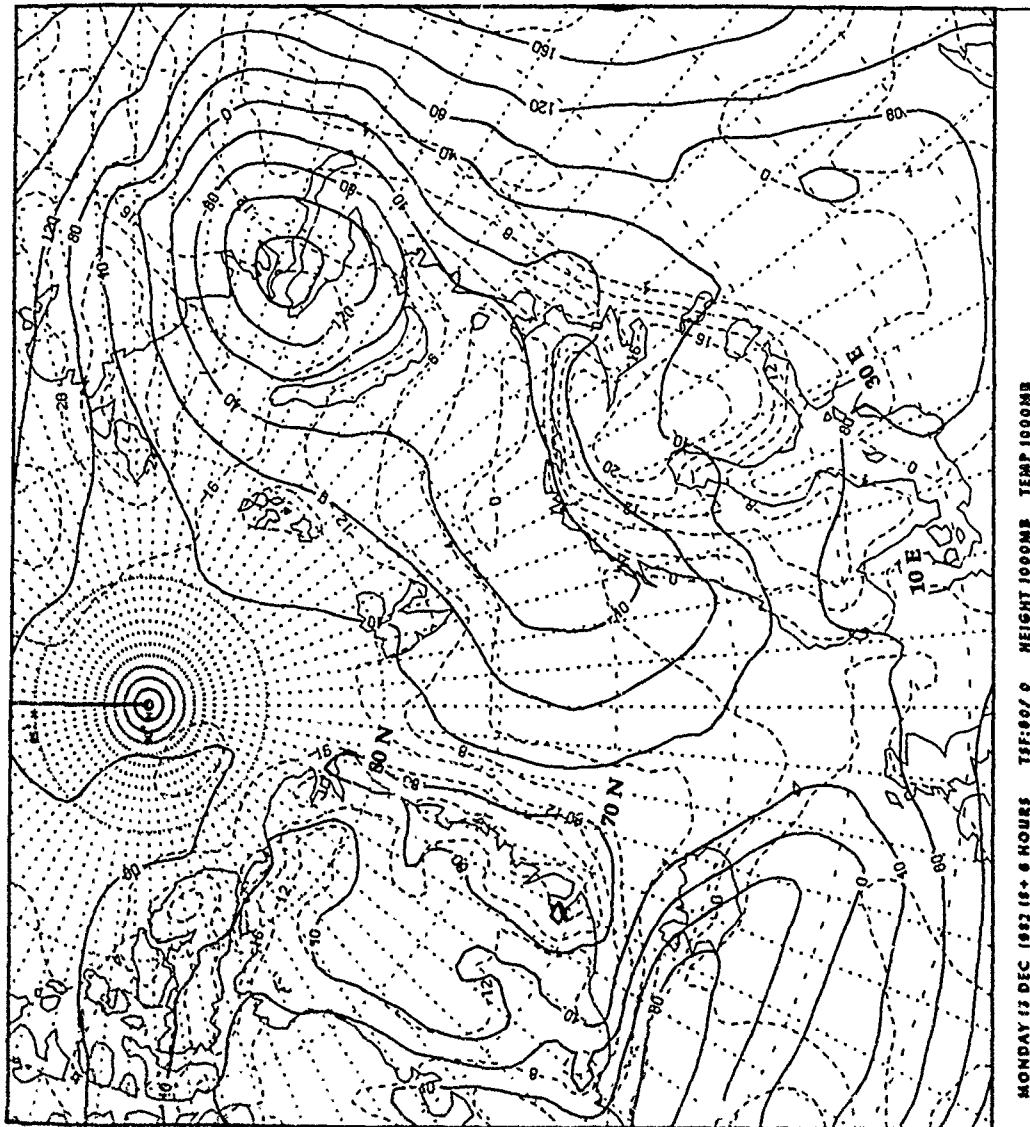


Fig. 5.21a

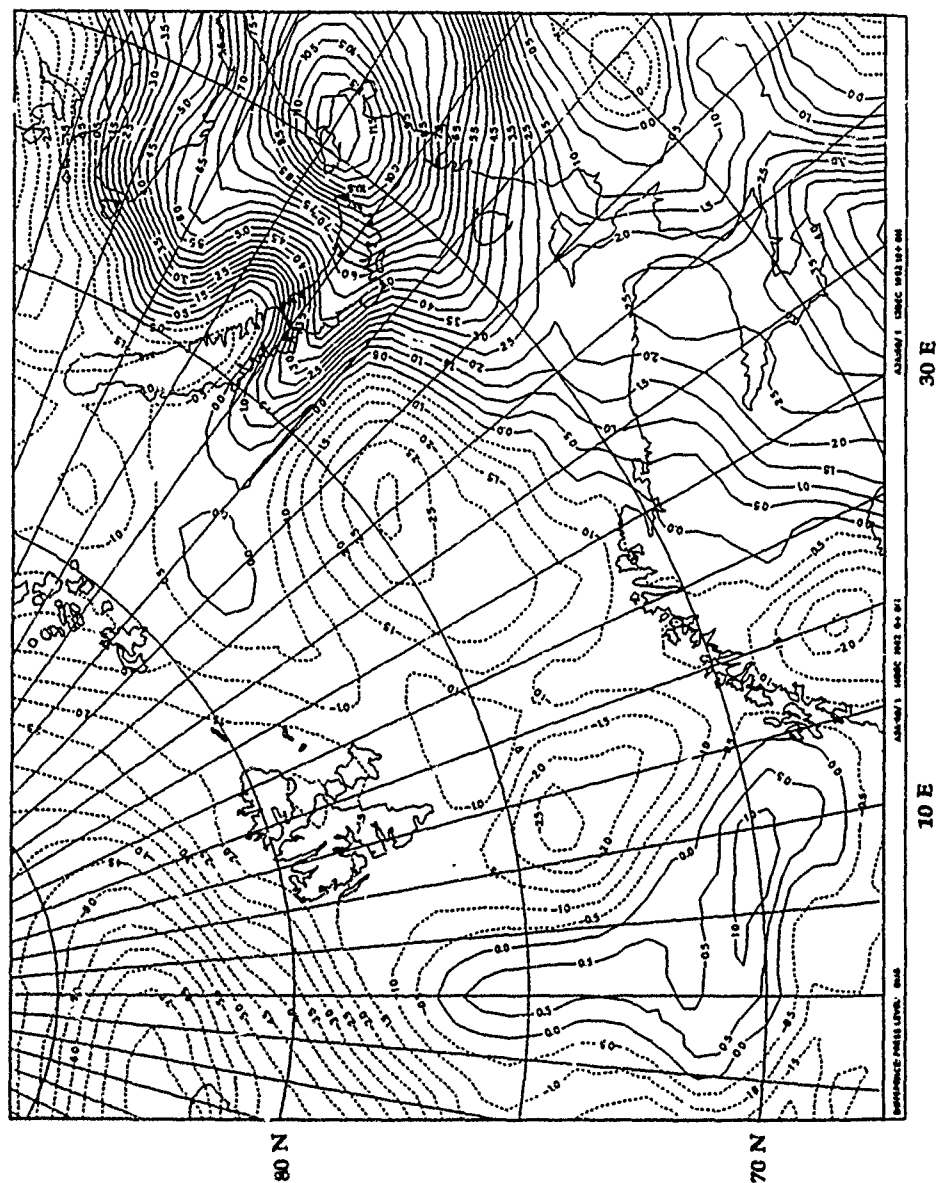


Fig.5.21b

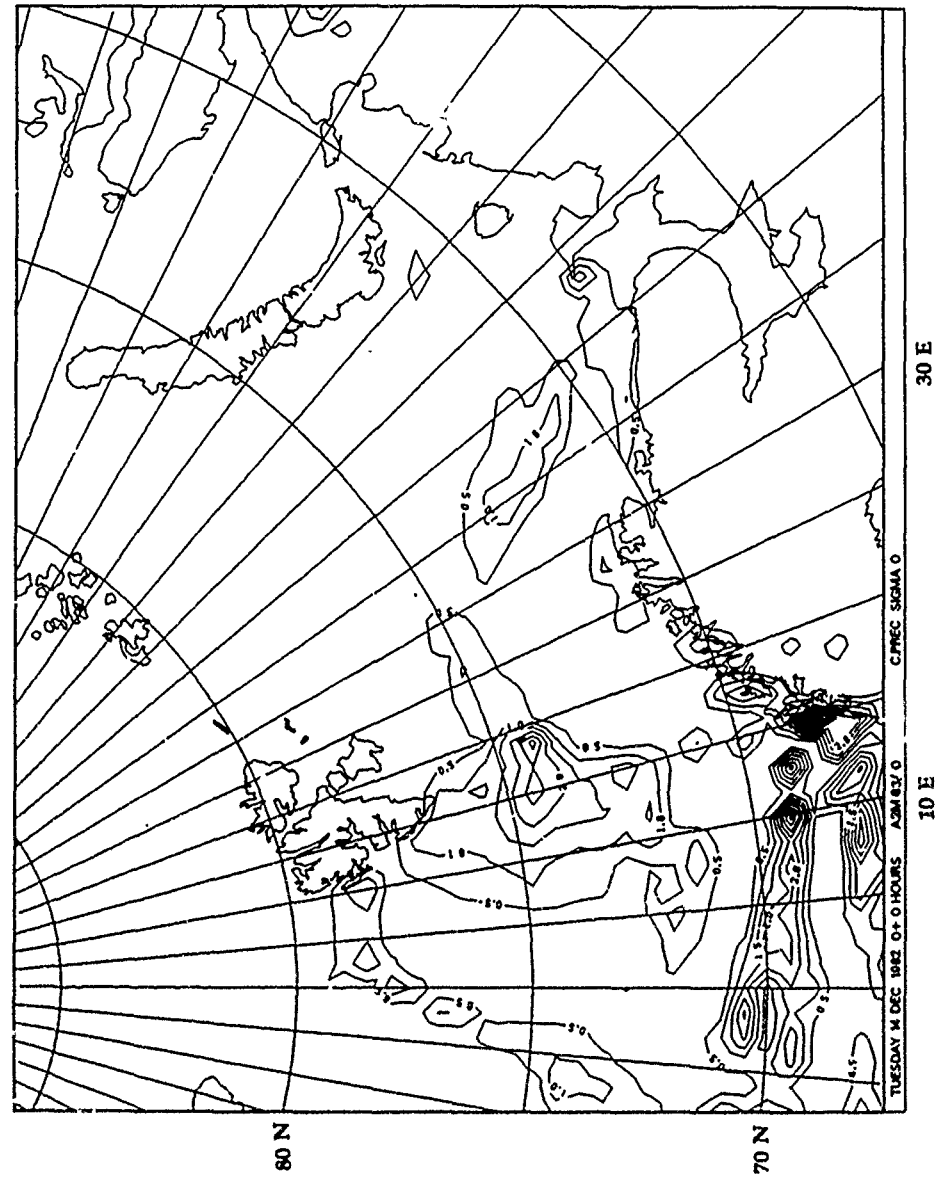


Fig. 5.22

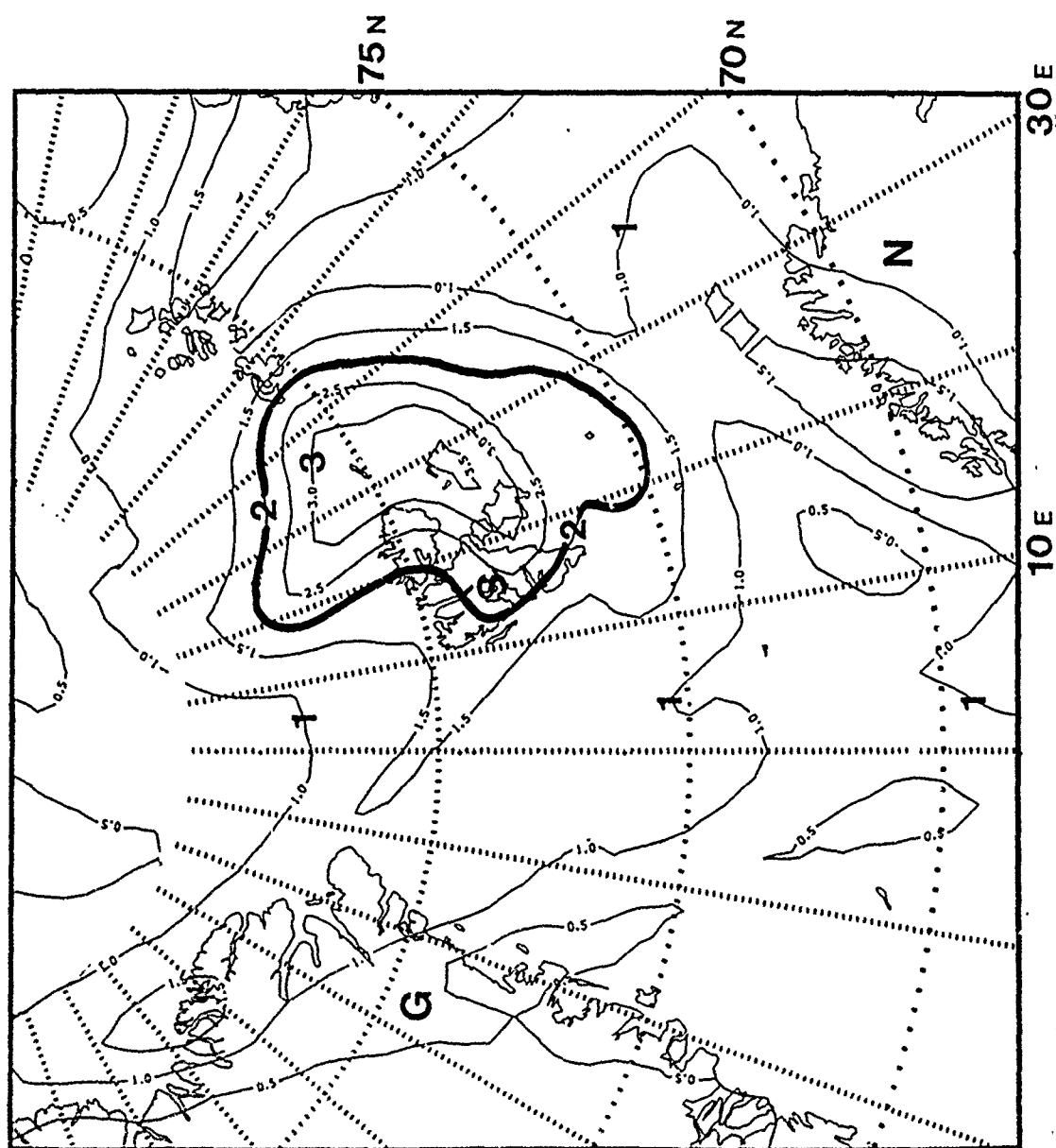


Fig. 5.23a



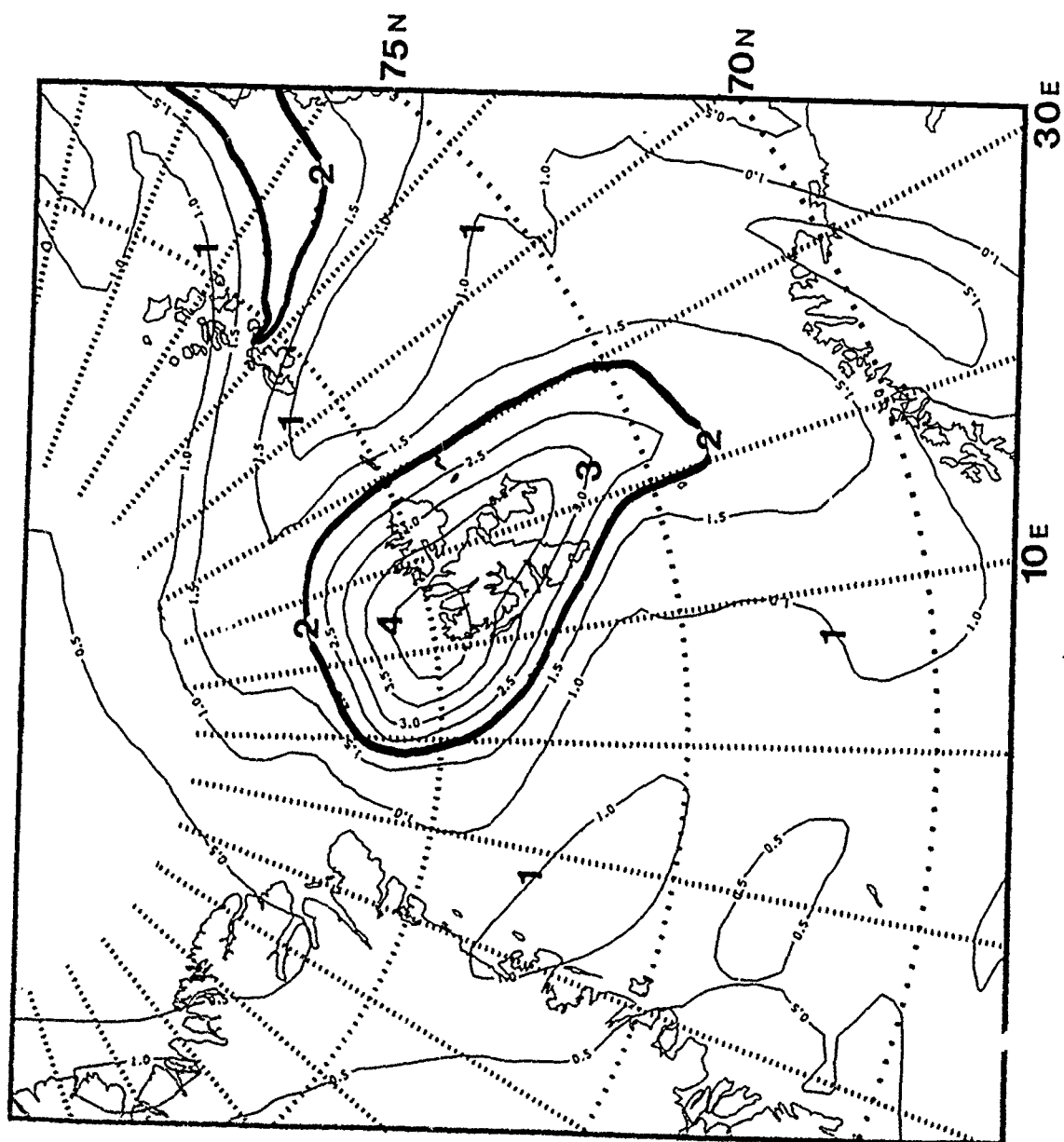


Fig. 5.23b

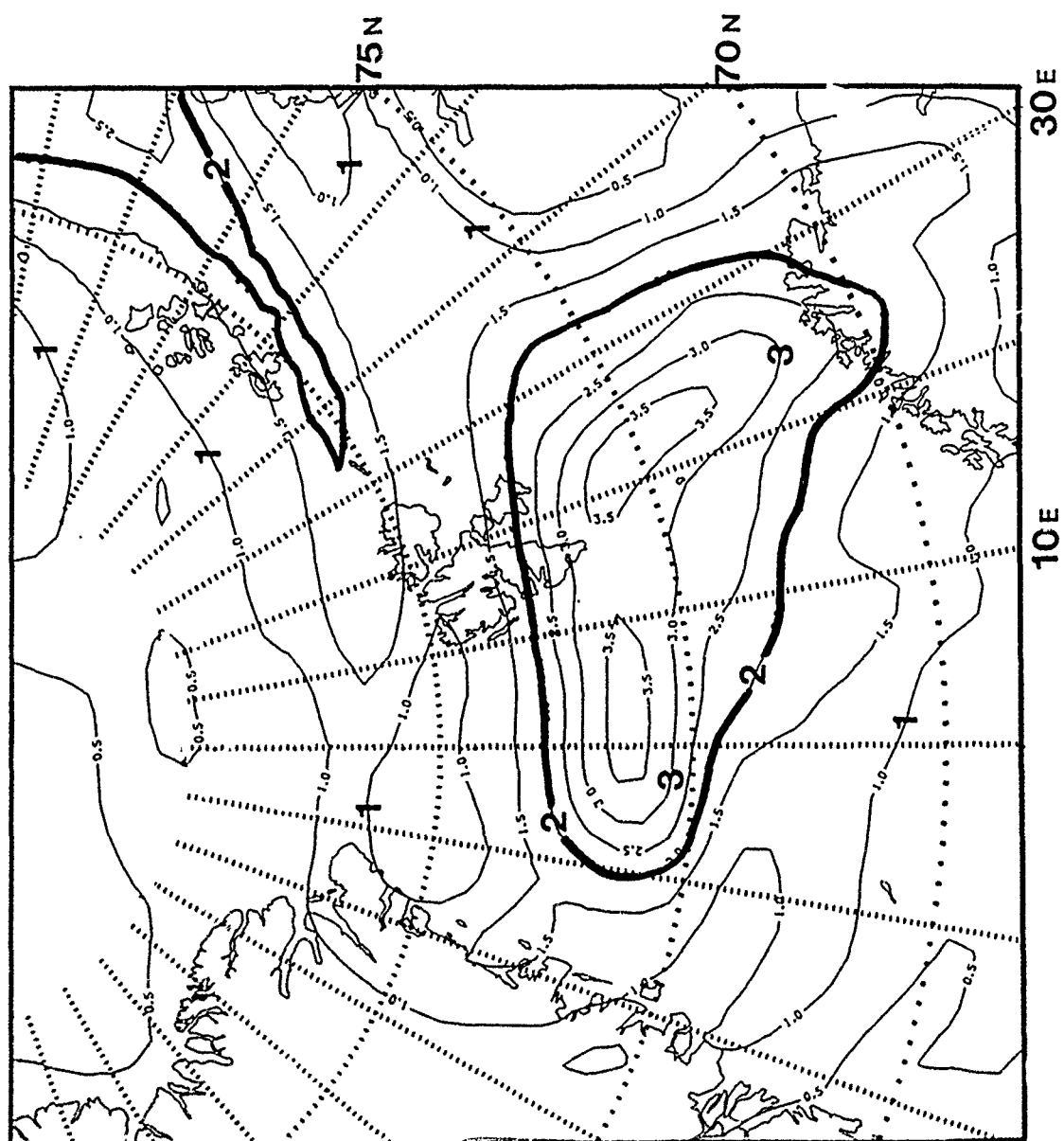


Fig. 5.23.c

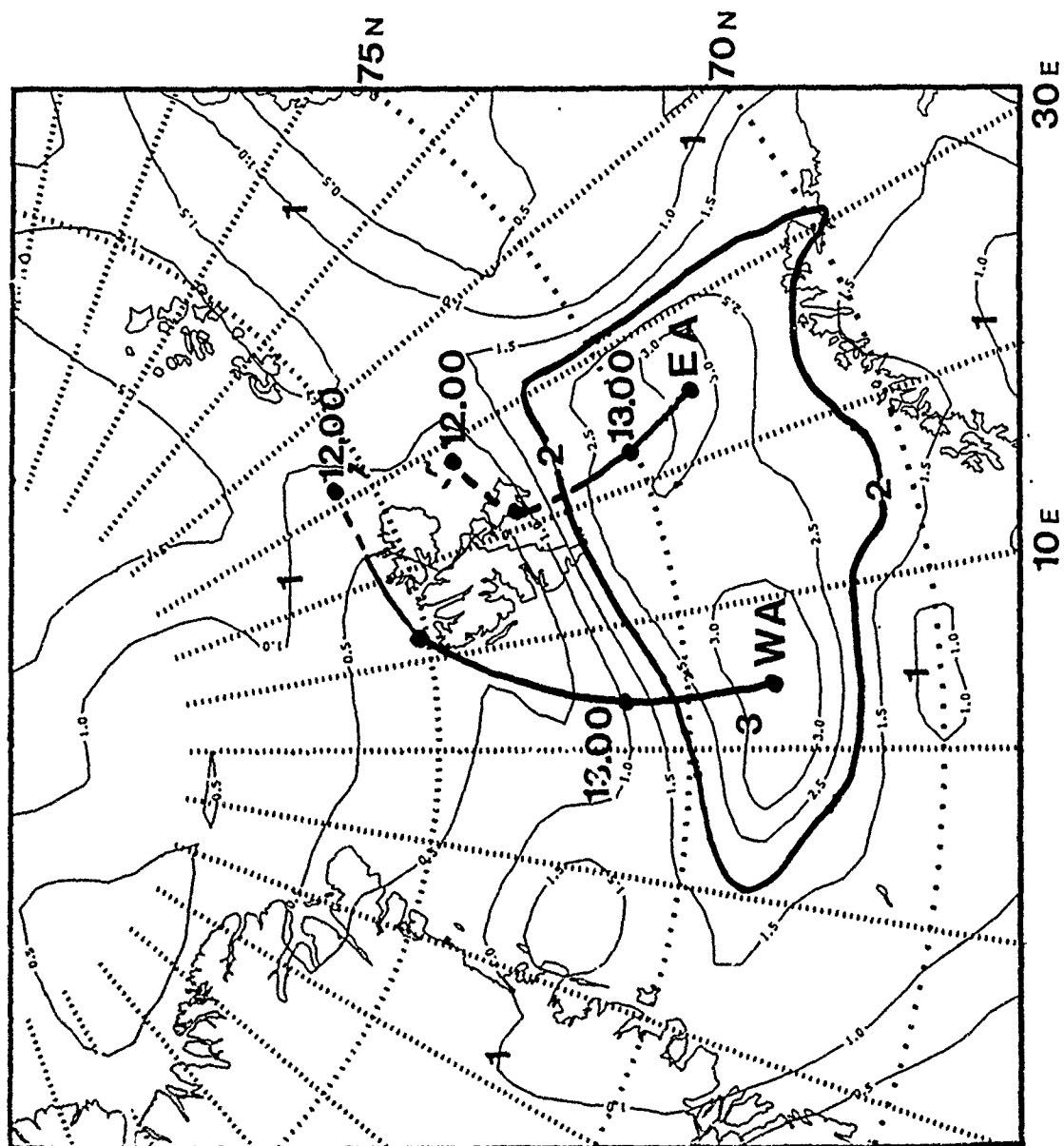


Fig. 5.23d

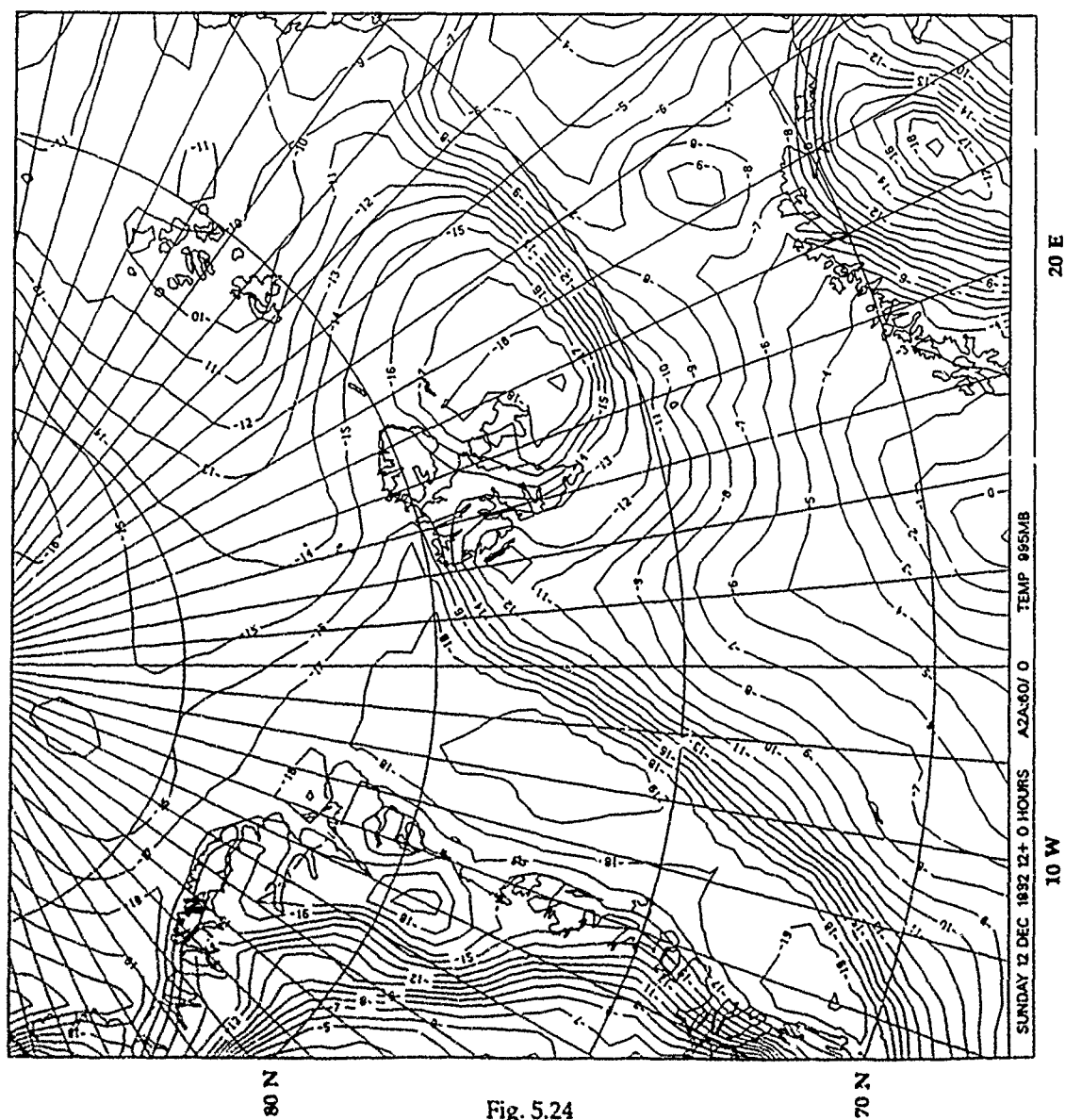


Fig. 5.24

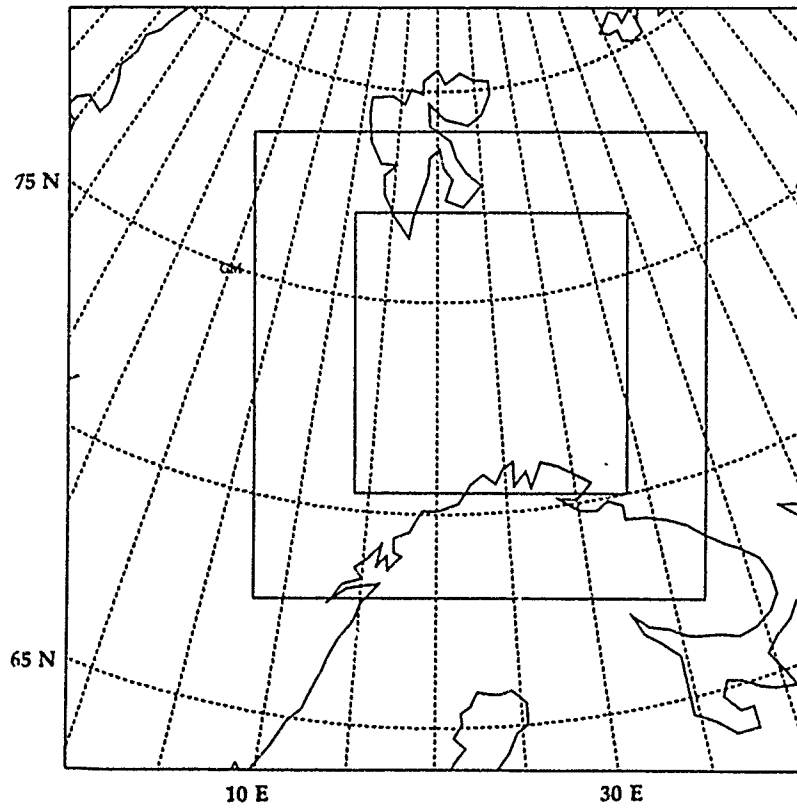
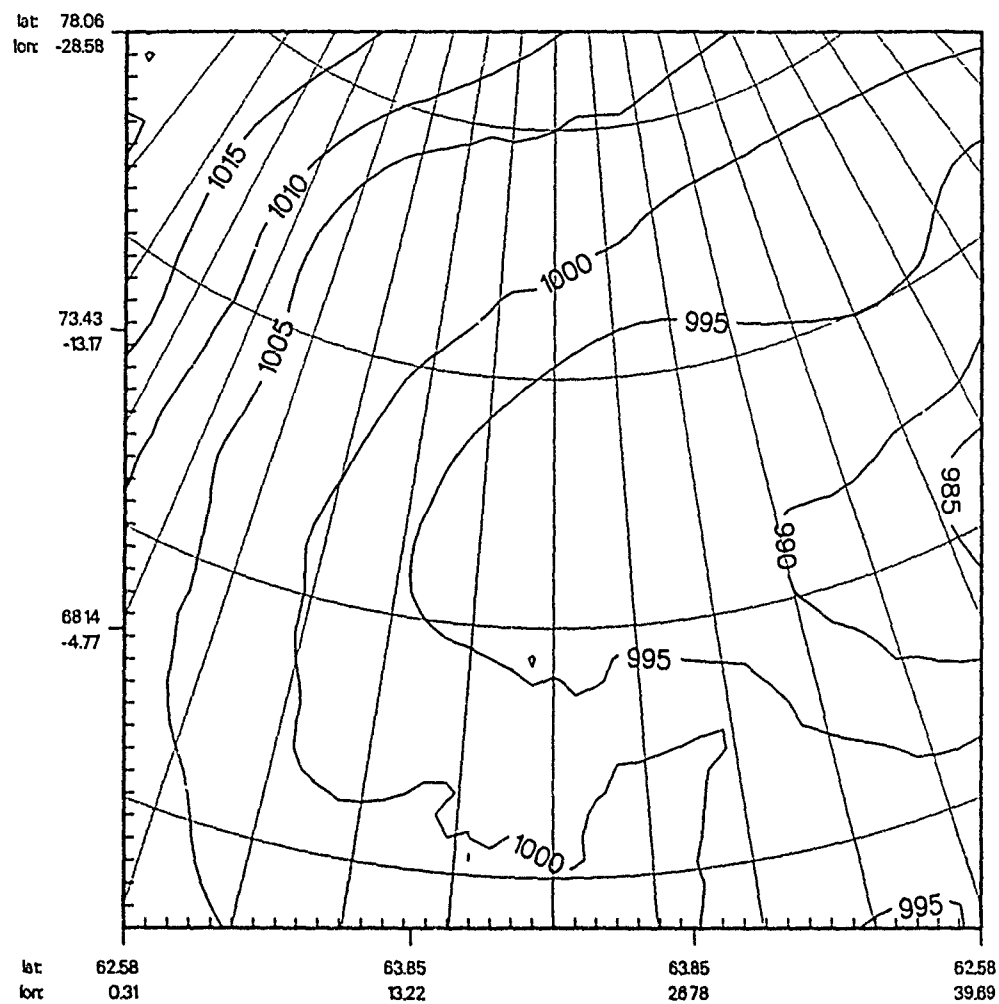


Fig. 5.25

run02:



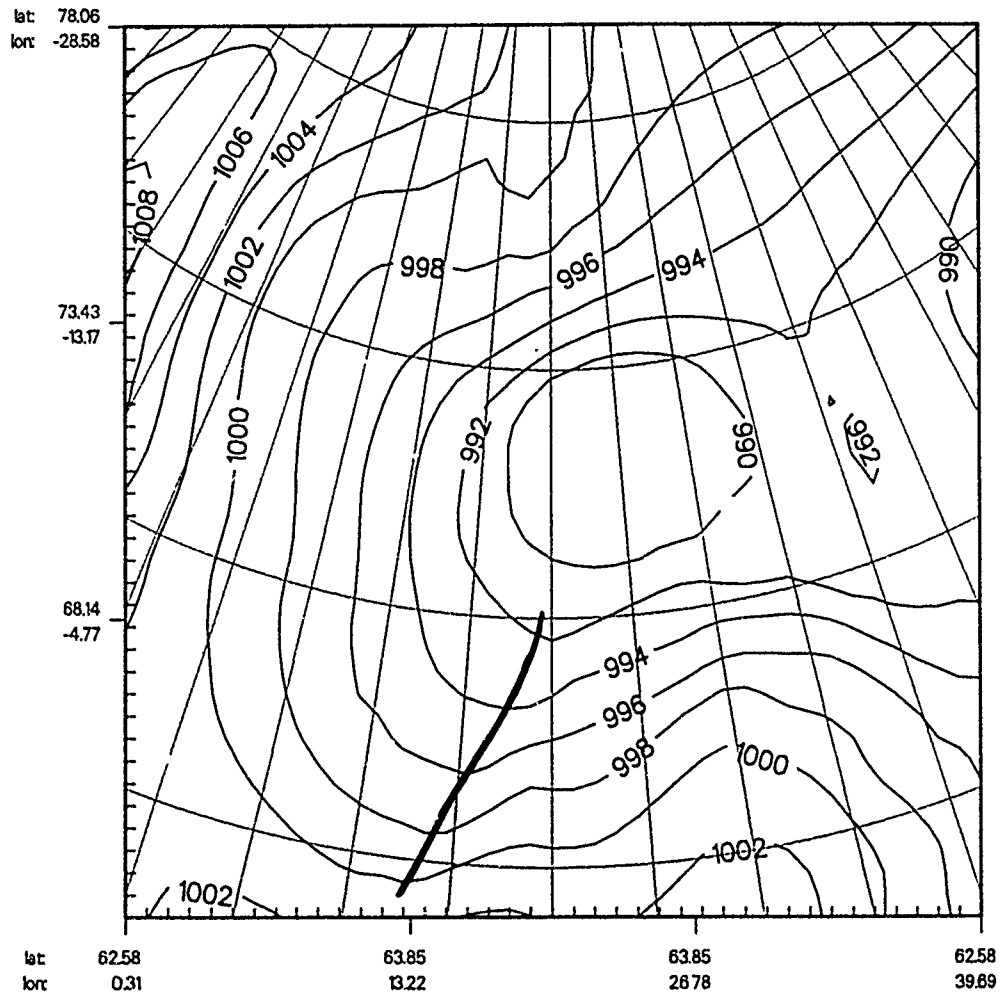
reduced MSL prs.

z = 0.0 m  
time: 0 day 0 hour 0 min 0 s  
file: an01cwig1

Contours:  
increment: 5.00E+00  
labels multiplied by: 100E+00  
min: 98138; max: 1020.81

Fig. 5.26

run2



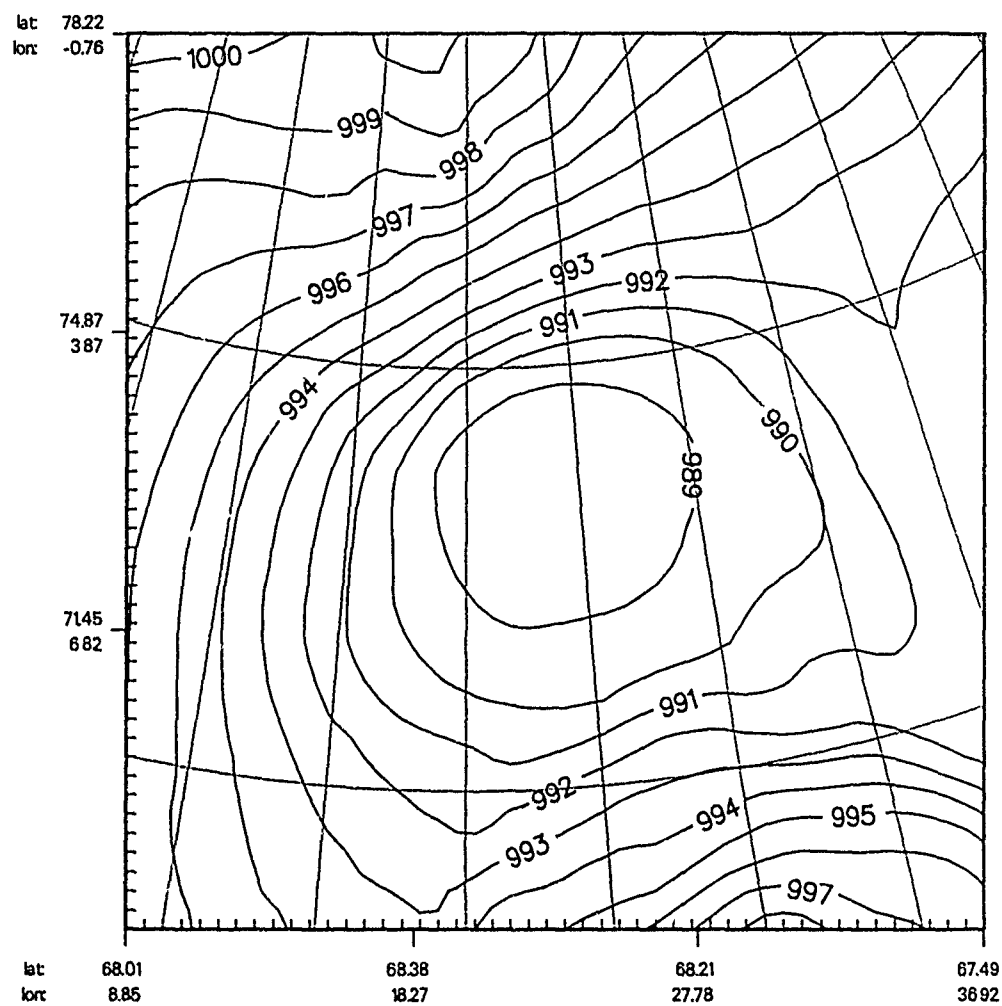
reduced MSL prs.

z = 0.0 m  
time: 0 day 12 hour 0 min 0 s  
file: an22cw1g1

Contours:  
increment: 2.00E+00  
labels multiplied by: 100E+00  
min: 9.883E+02; max: 1009E+03

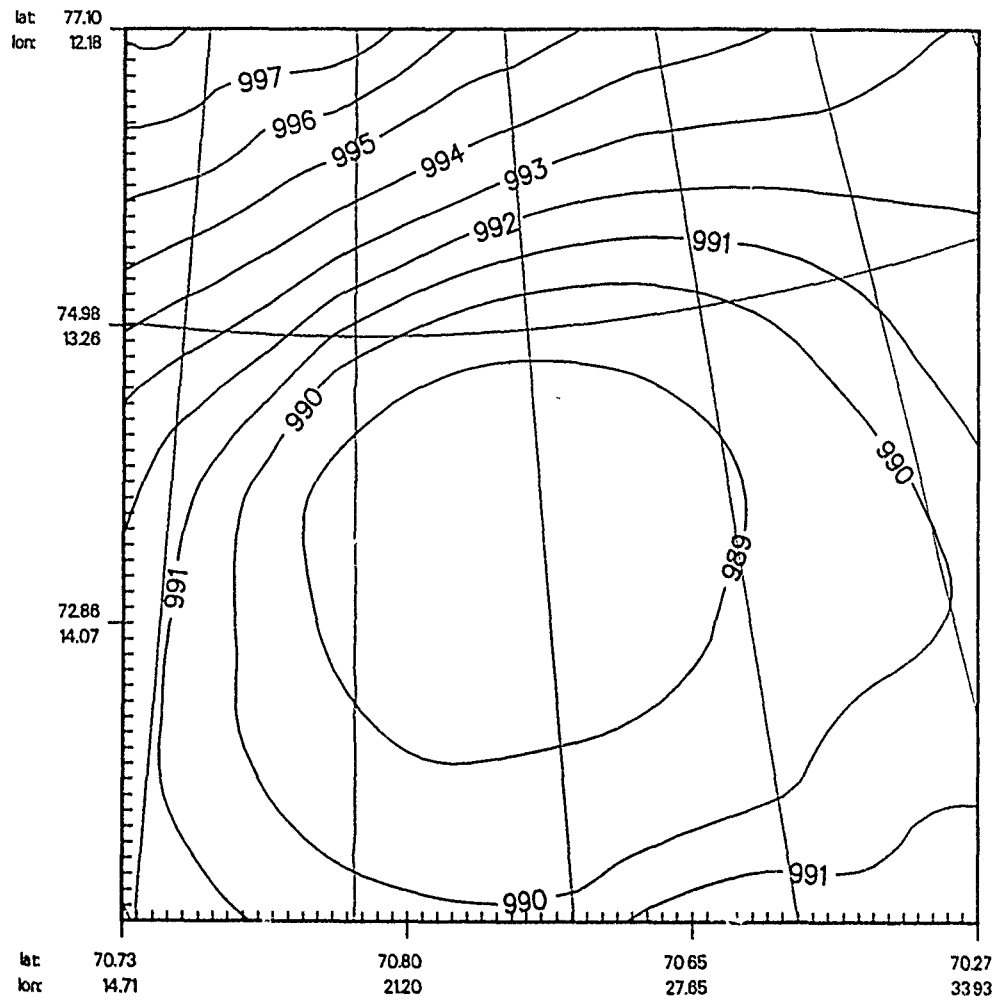
Fig. 5.27a

run02:





run02:



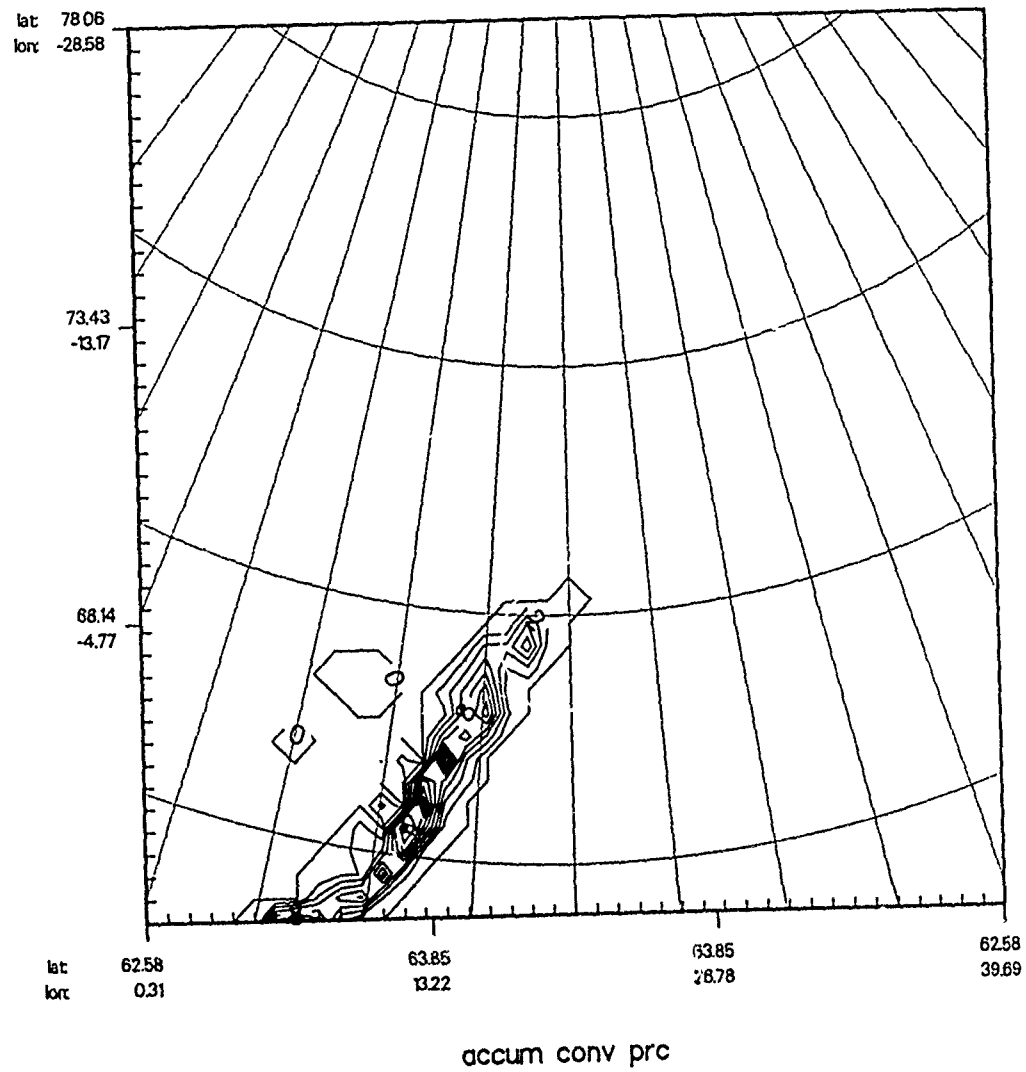
reduced MSL prs.

z = 0.0 m  
time: 0 day 12 hour 0 min 0 s  
file: an22cw1g3

Contours:  
increment: 100E+00  
labels multiplied by: 100E+00  
min: 988.23; max: 998.15

Fig. 5.27c

run02:

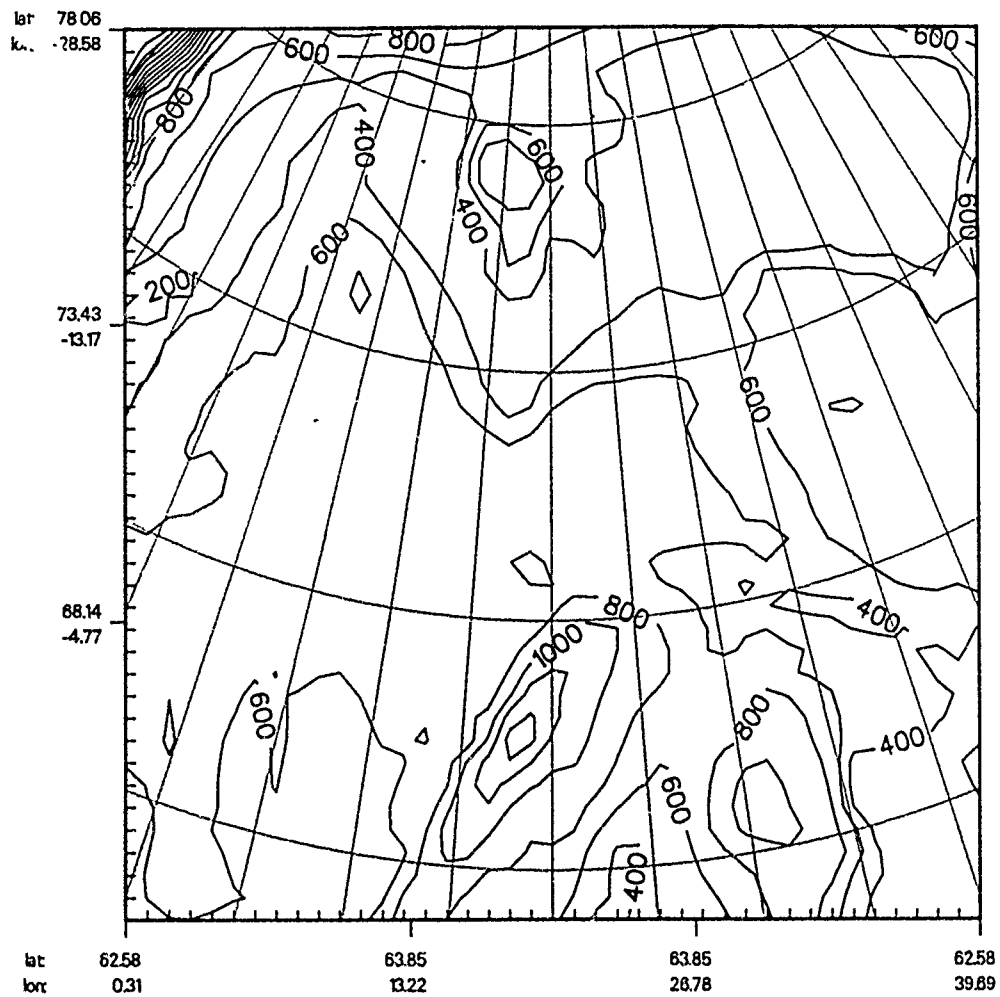


z = 0.0 m  
time: 0 day 12 hour 0 min 0 s  
file: an22cw1g1

Contours:  
increment: 2.00E-01  
labels multiplied by: 100E+01  
min: -0.00; max: 173

Fig. 5.28

Run2:



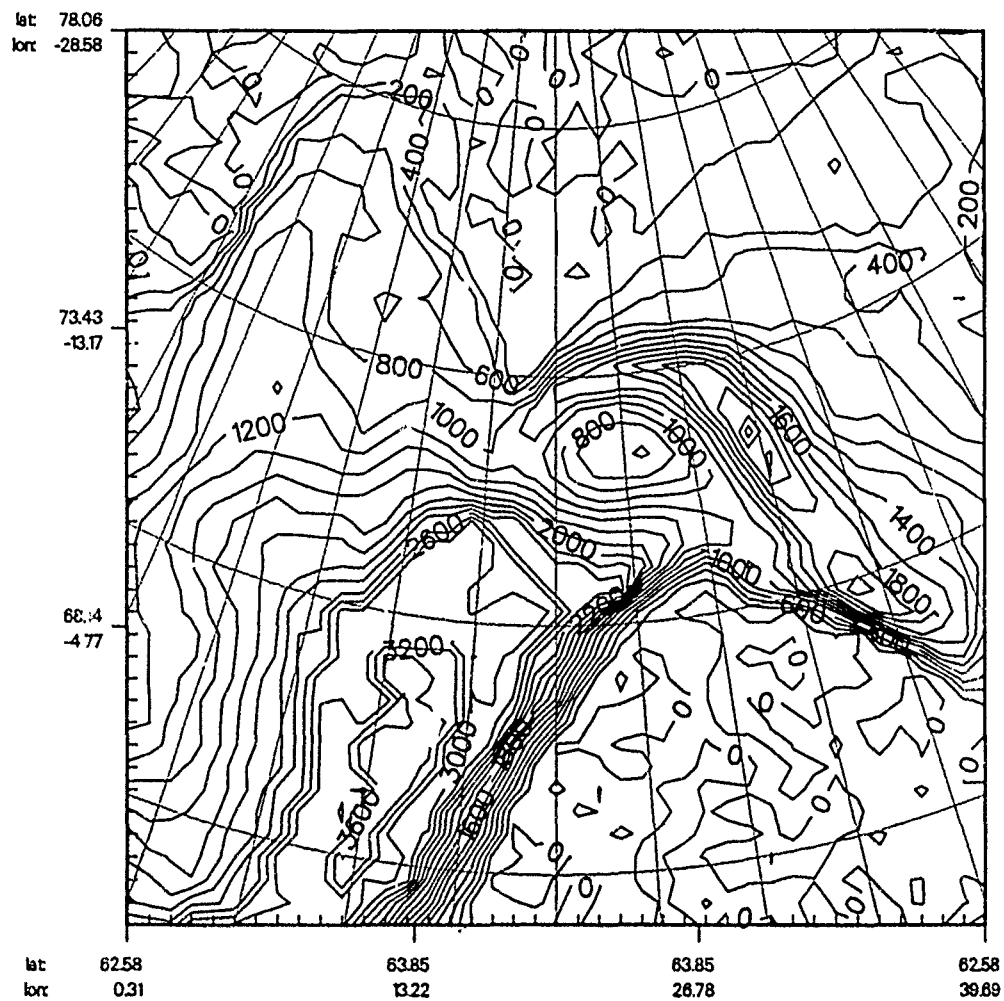
LCL

z = 97.6 m K= 2  
 time: 0 day 12 hour 0 min 0 s  
 file: an22cw1g1

Contours:  
 increment: 2.00E+02  
 labels multiplied by: 100E+00  
 min: 1427E+02; max: 3.215E+03

Fig. 5.29

Run2:



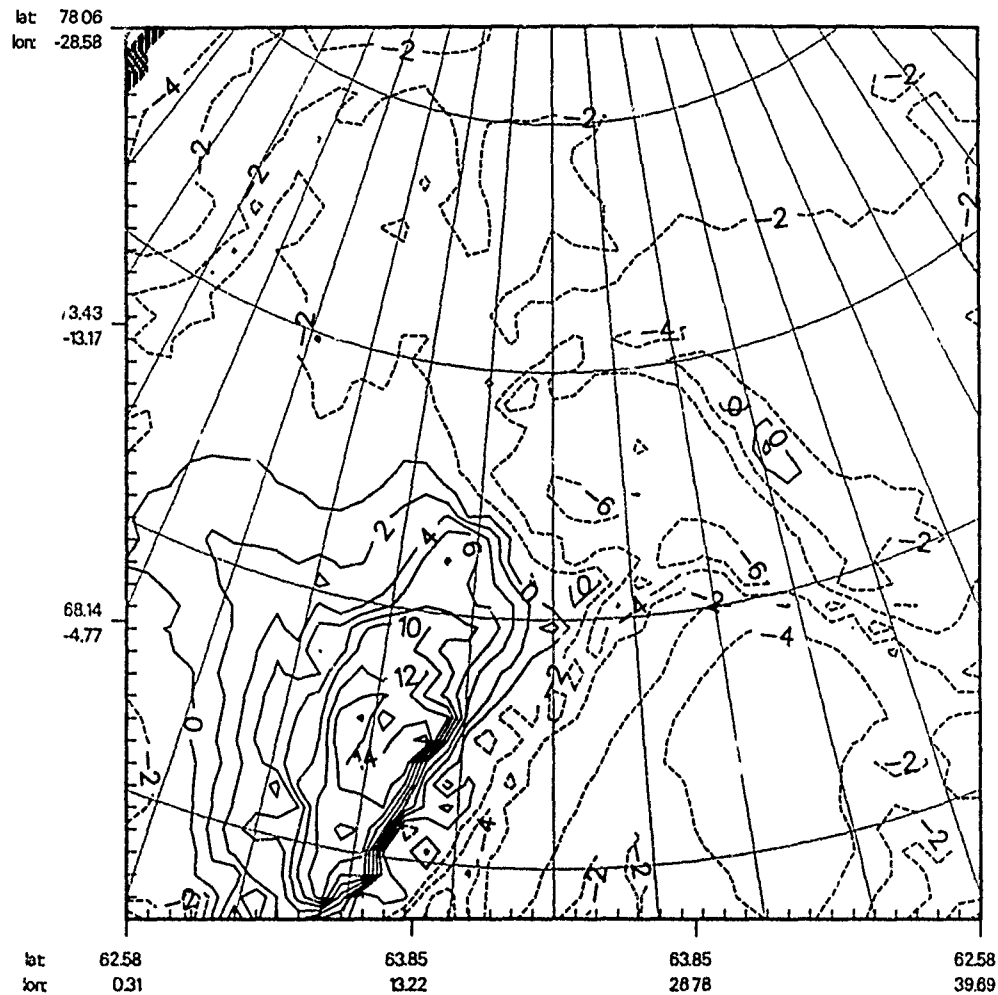
LCL - ETL depth

z = 97.6 m K= 2  
time: 0 day 12 hour 0 min 0 s  
file: an22cw\gl

Contours:  
increment: 2.00E+02  
labels multiplied by: 1.00E+00  
min: -5.846E+01; max: 3.802E+03

Fig. 5.30

run02:



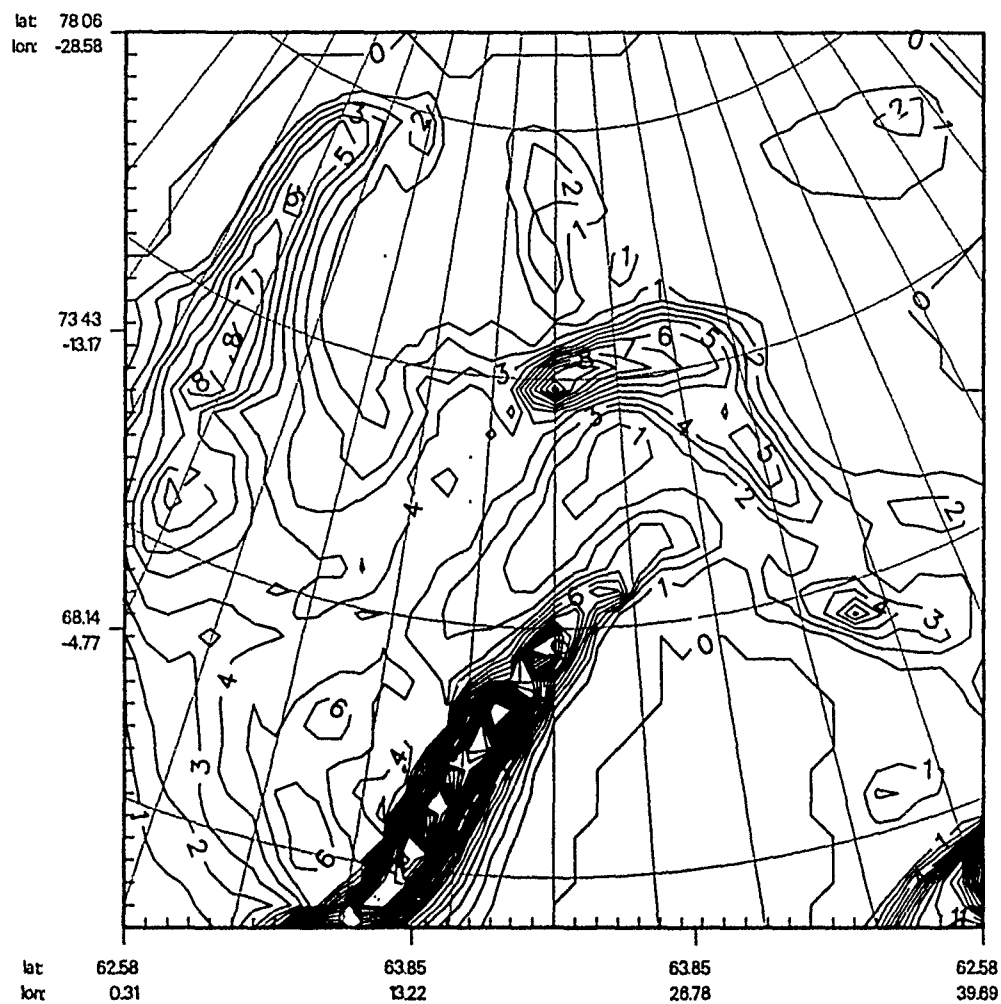
ABE

z = 97.6 m K<sub>2</sub> 2  
time: 0 day 12 hour 0 min 0 s  
file: an22cw1g1

Contours:  
increment: 2.00E+00  
labels multiplied by: 100E+00  
min: -28.54; max: 16.72

Fig. 5.31

run02:



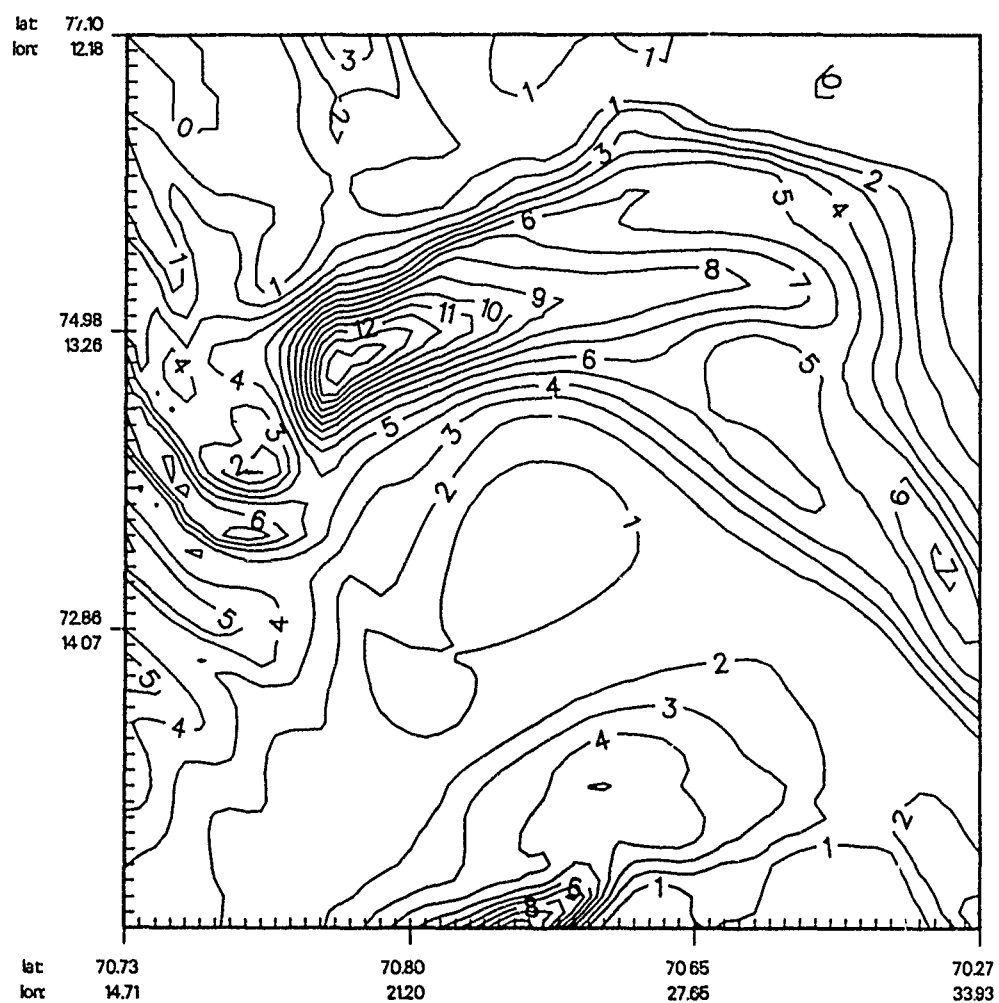
tot accum precip

z = 0.0 m  
time: 0 day 12 hour 0 min 0 s  
file: an22cw1g1

Contours:  
increment: 100E-01  
labels multiplied by: 100E+01  
min: -4.000E-20; max: 3.157E+00

Fig. 5.32a

run02:



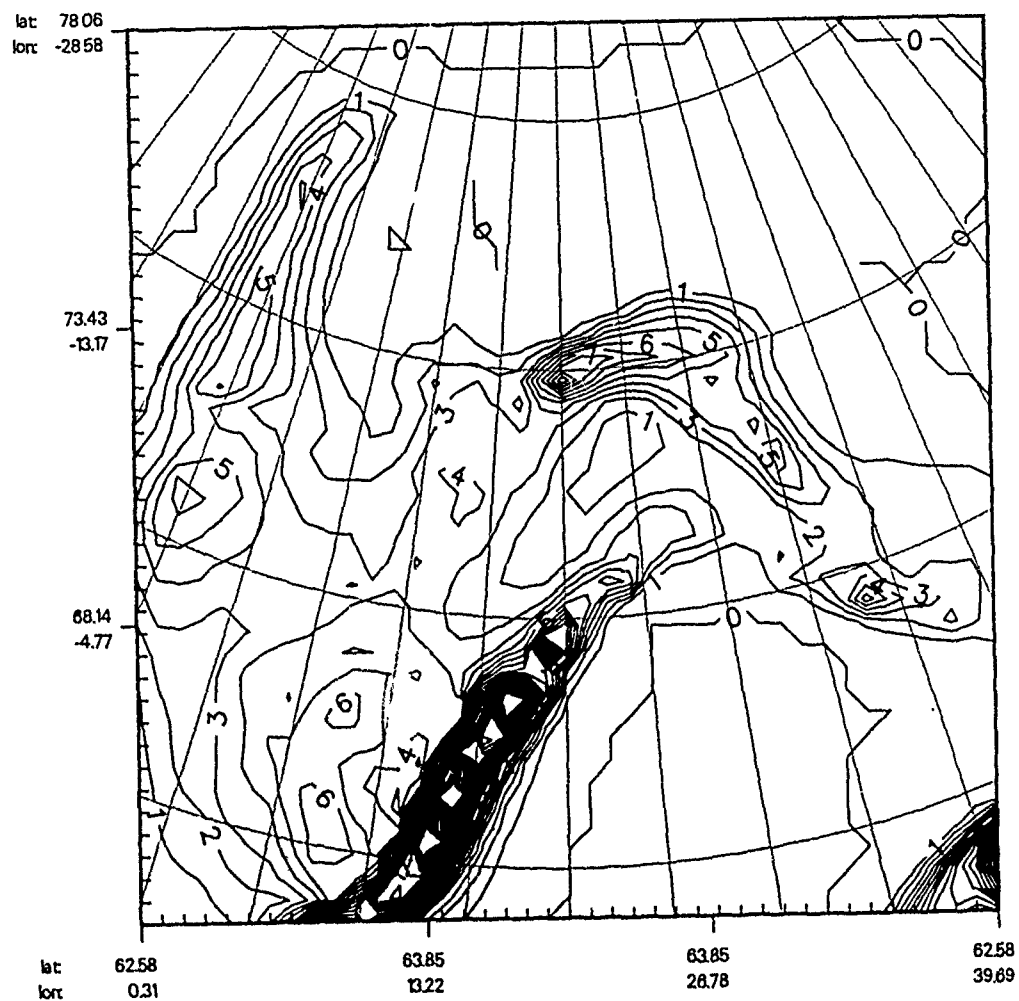
tot accum precip

z = 0.0 m  
time: 0 day 12 hour 0 min 0 s  
file: an22cw1g3

Contours:  
increment: 100E-01  
labels multiplied by: 100E+01  
min: -4.000E-20; max: 1480E+00

Fig. 5.32b

run02:



accum agg reg prc

z = 0.0 m  
time: 0 day 12 hour 0 min 0 s  
file: an22cw1g1

Contours:  
increment: 100E-01  
labels multiplied by: 100E+01  
min: -2.000E-20; max: 2.973E+00

Fig. 5.33



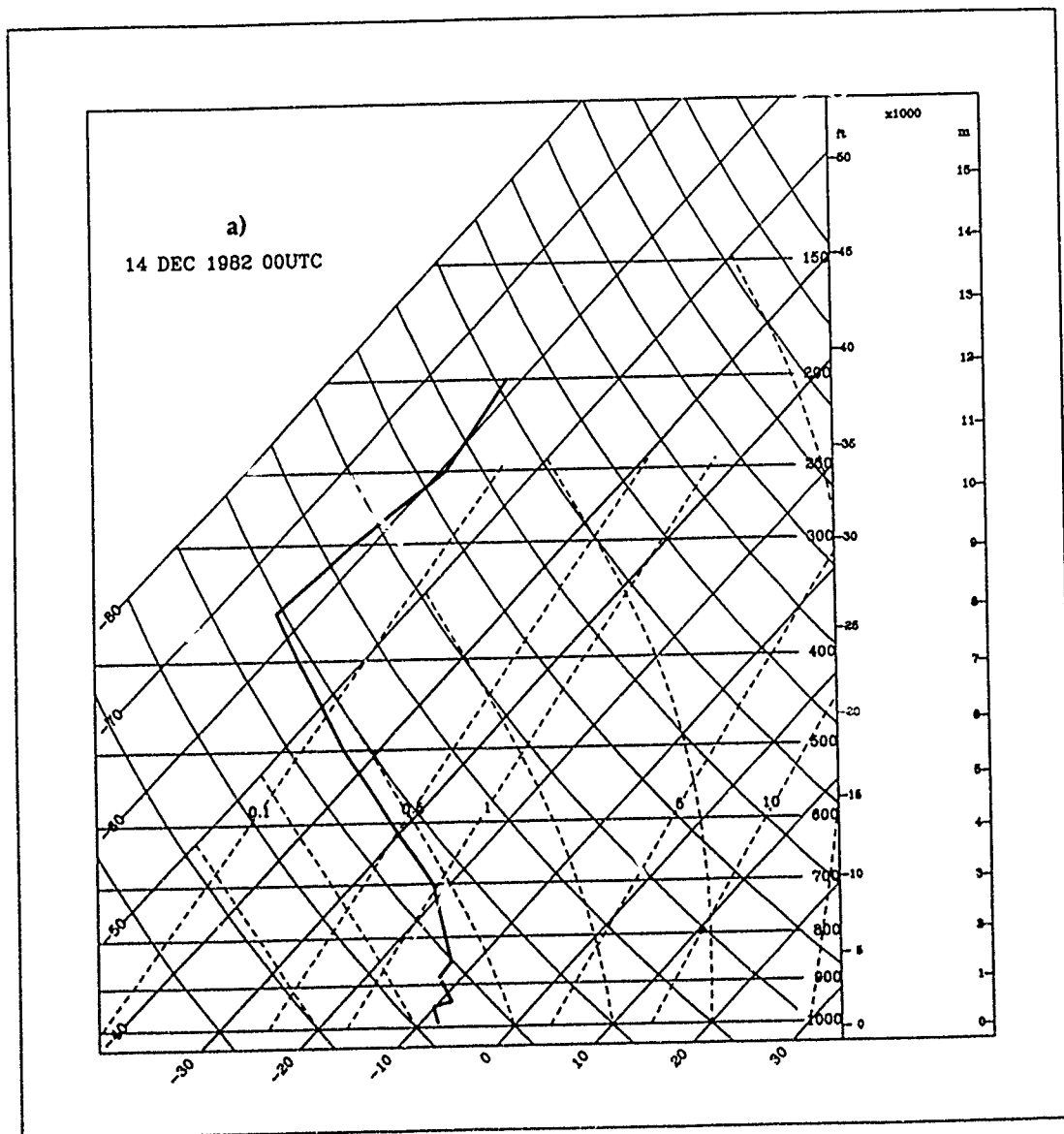


Fig. 5.34

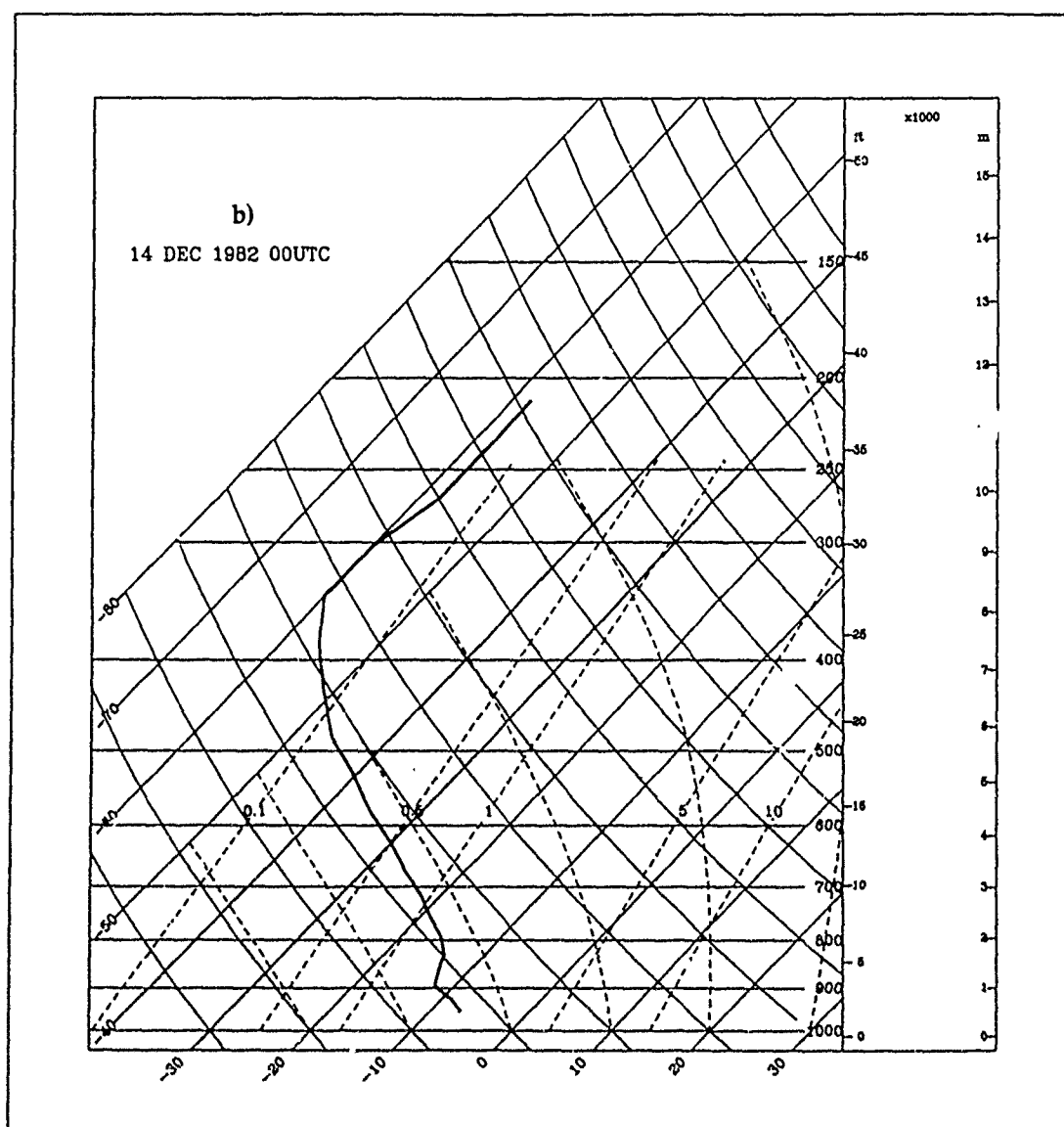
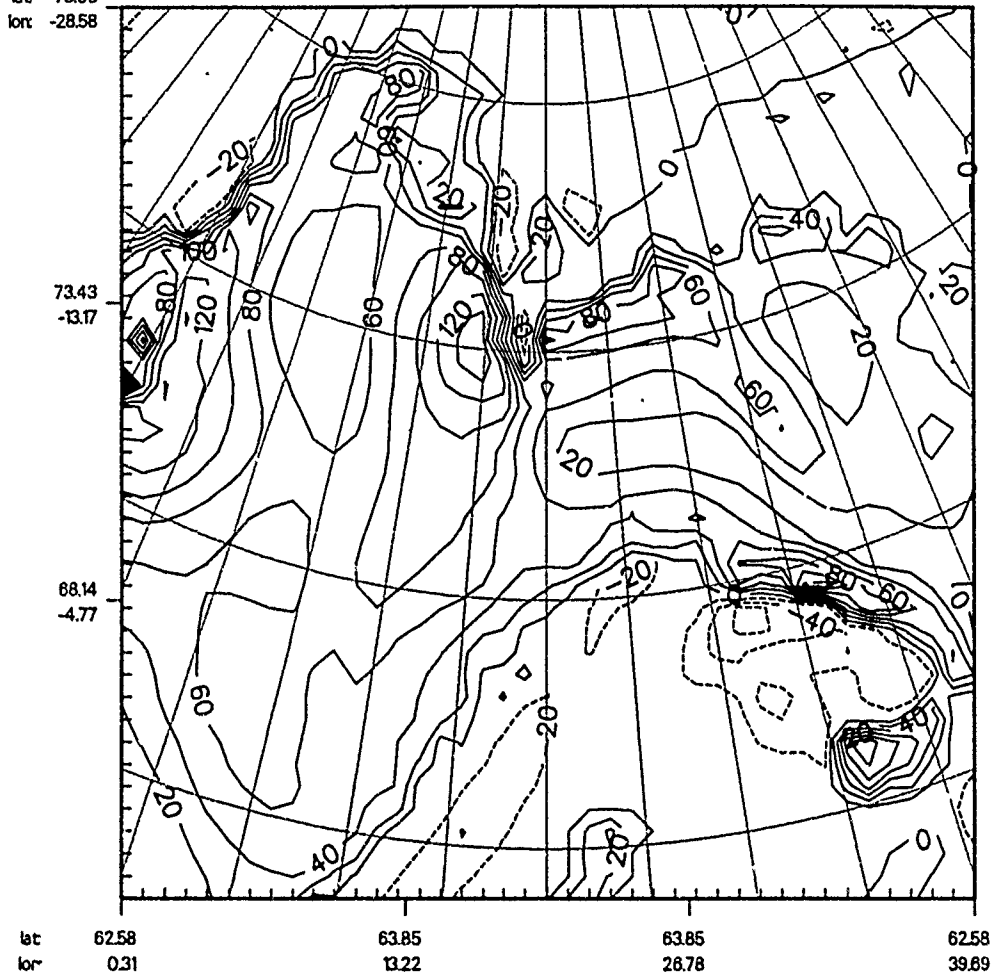


Fig. 5.34

run2

lat: 78.06  
lon: -28.58

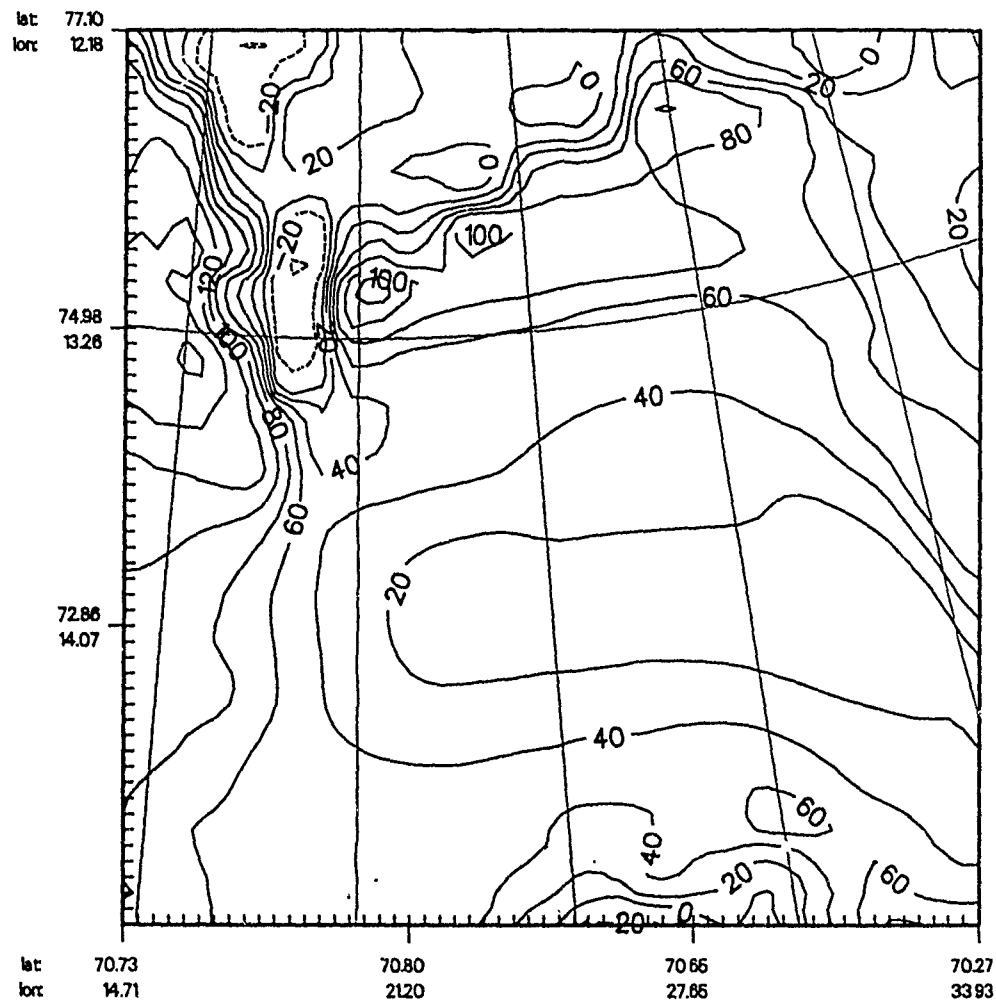
sfc. sen. heatfx

z = 0.0 m  
time: 0 day 12 hour 0 min 0 s  
file: an22cw1g1

Contours:  
increment: 2.00E+01  
labels multiplied by: 1.00E+00  
min: -6.482E+01; max: 1.622E+02

Fig. 5.35a

Run2:



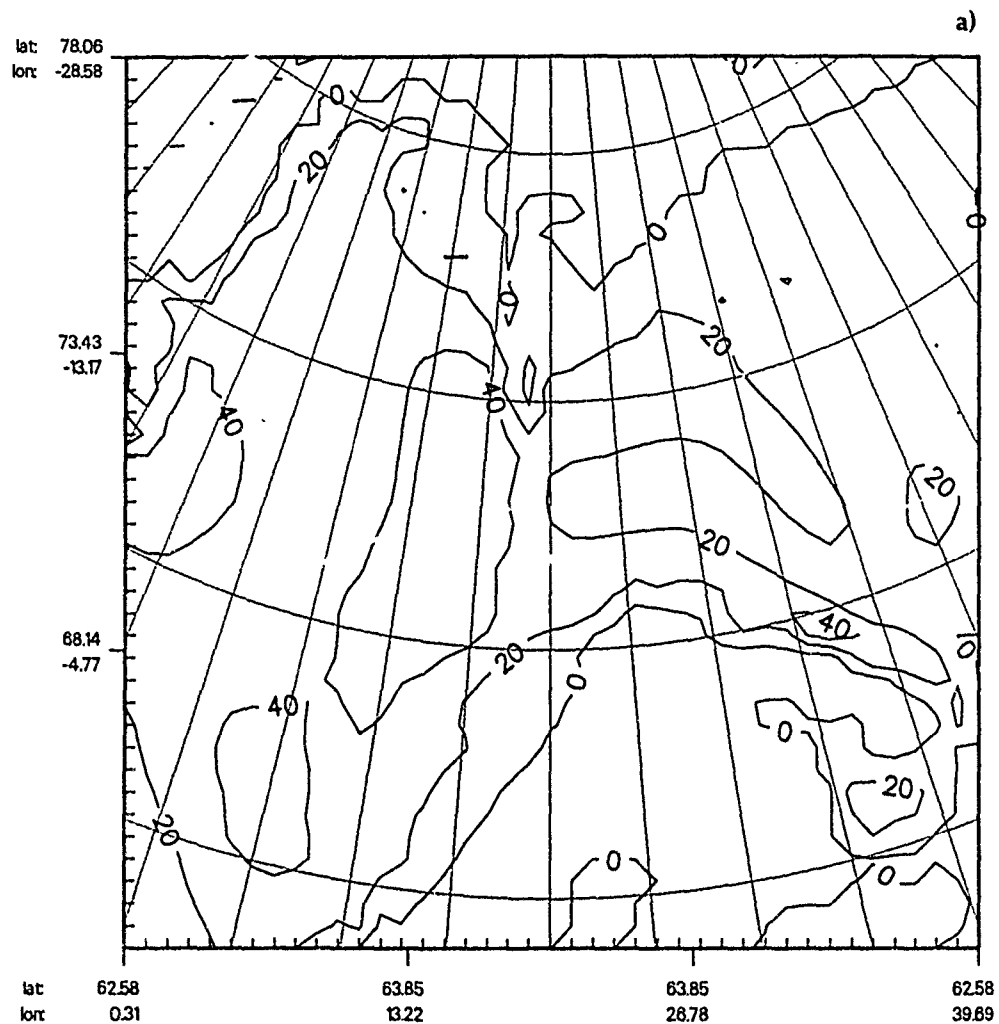
sfc. sen. heatfx

z = 0.0 m  
time: 0 day 12 hour 0 min 0 s  
file: an22cw1g3

Contours:  
increment: 2.00E+01  
labels multiplied by: 1.00E+00  
min: -4.125E+01; max: 1.640E+02

Fig. 5.35b

run2



sfc. lat. heatfx

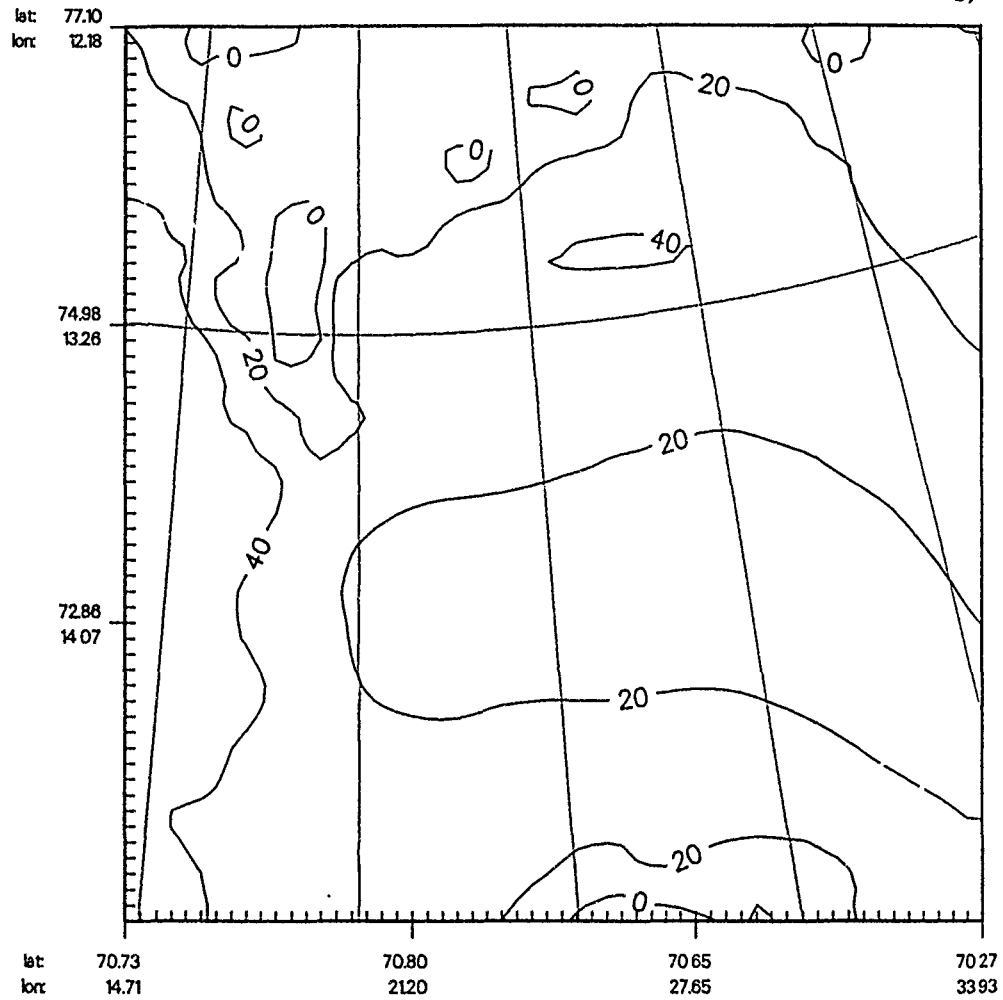
z = 0.0 m  
time: 0 day 12 hour 0 min 0 s  
file: an22cw1g1

Contours:  
increment: 2.00E+01  
labels multiplied by: 100E+00  
min: -1.313E+01; max: 5.626E+01

Fig. 5.36

Run2:

b)



sfc. lat. heatfx

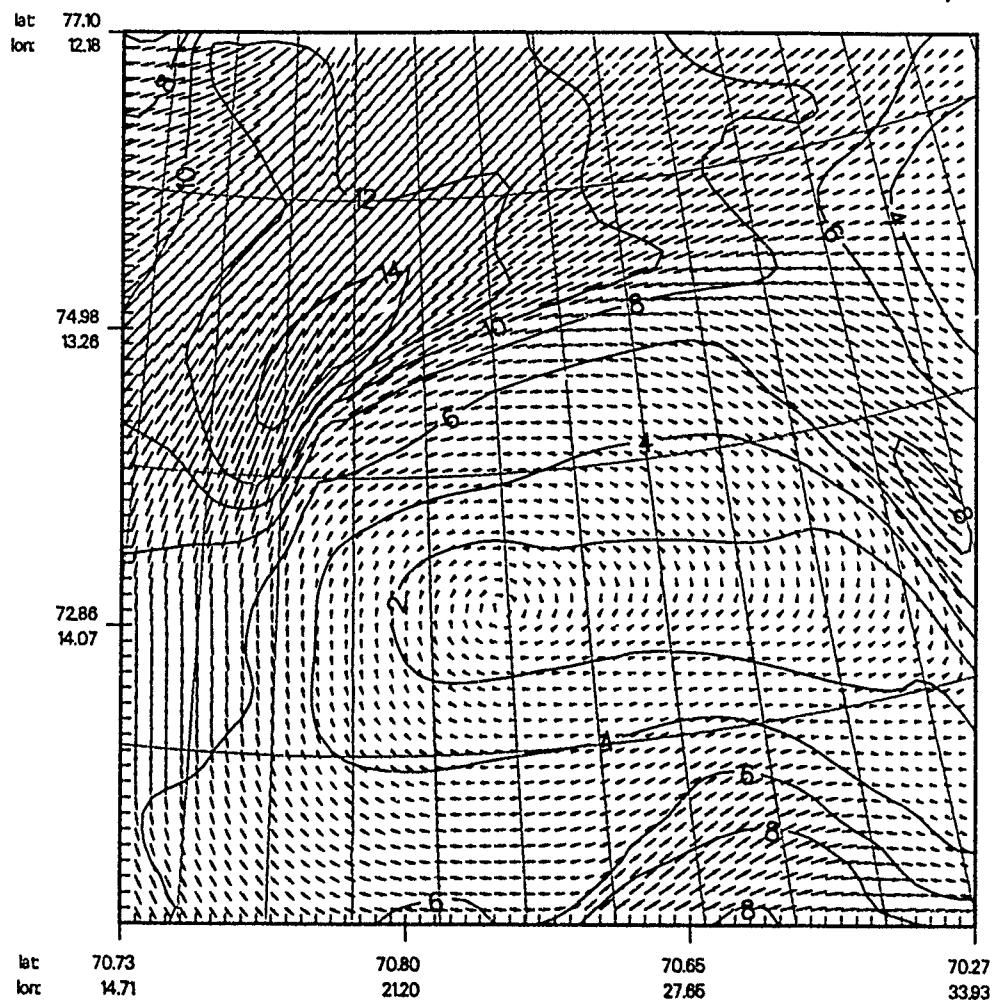
z = 0.0 m  
time: 0 day 12 hour 0 min 0 s  
file: an22cw1g3

Contours:  
increment: 2.00E+01  
labels multiplied by: 1.00E+00  
min: -1.118E+01; max: 5.817E+01

Fig. 5.36

Run2:

15 m/s



hor. wind speed

z = 97.6 m K= 2  
time: 0 day 12 hour 0 min 0 s  
file: an22cw1g3

Contours:  
increment: 2.00E+00  
labels multiplied by: 1.00E+00  
min: 6.106E-02; max: 1.495E+01

Fig. 5.37

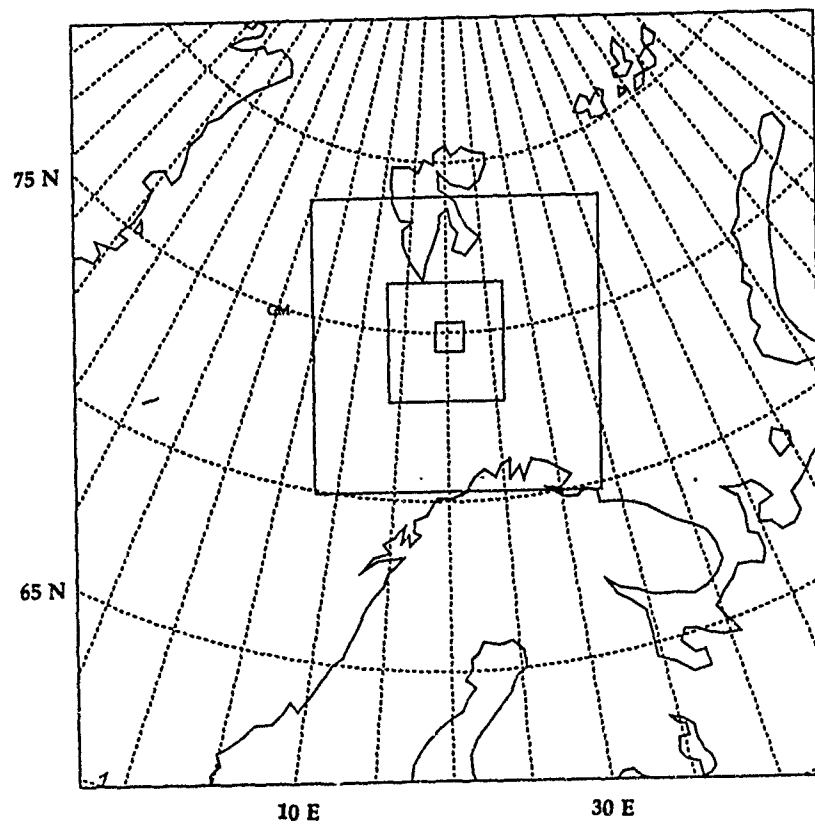
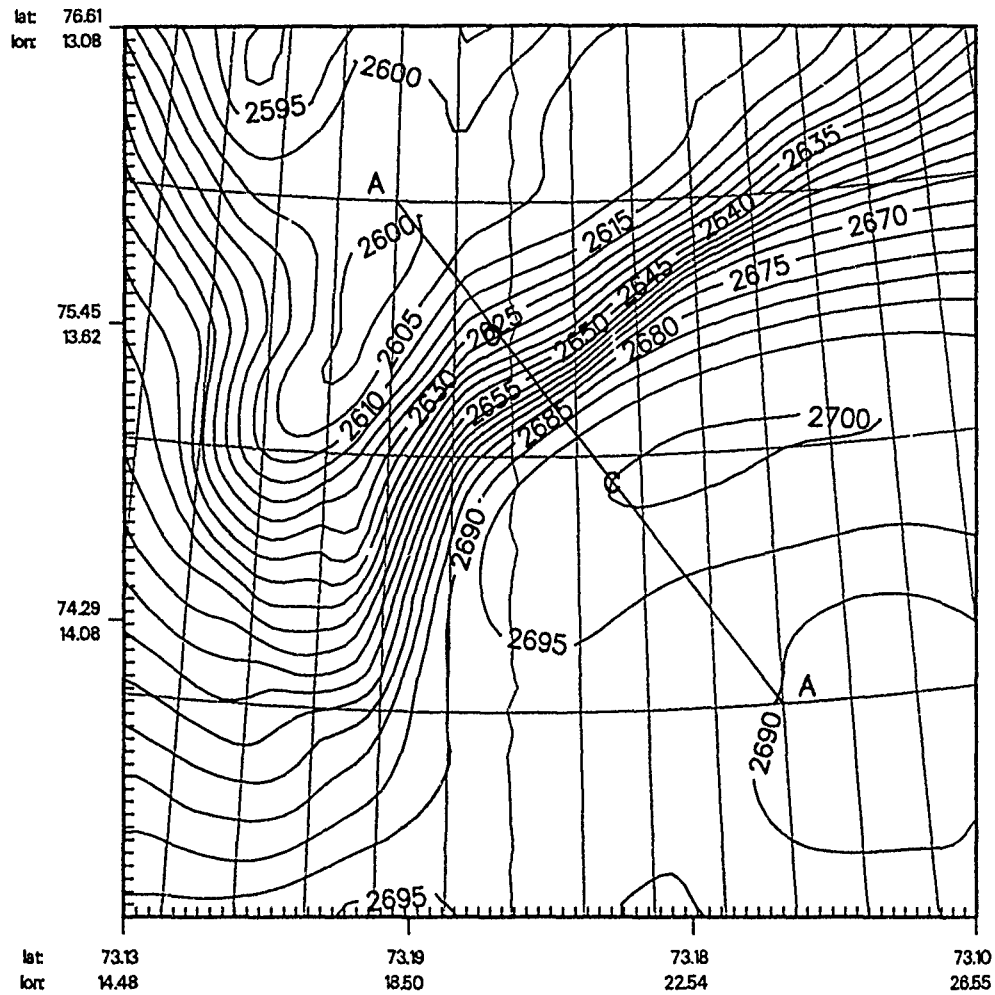


Fig. 5.38



Run3:

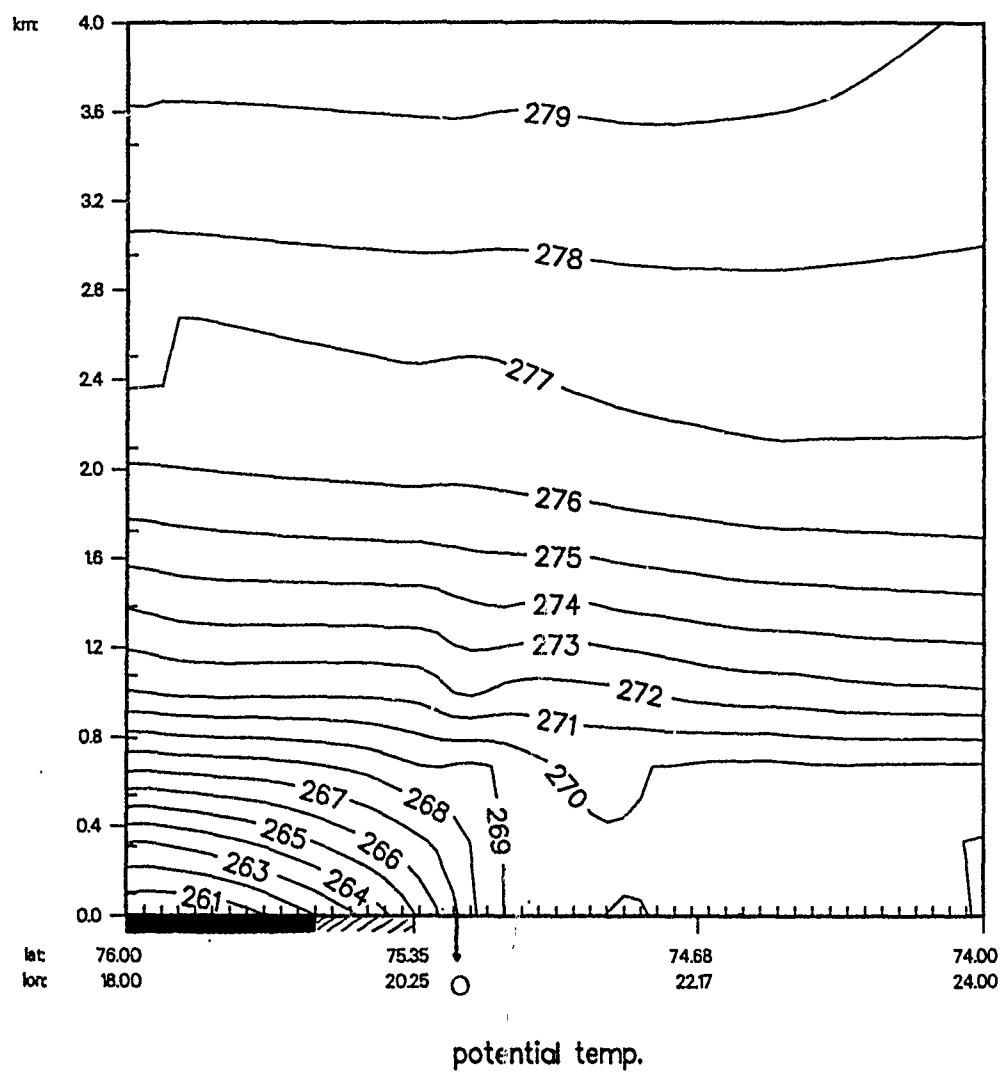


potential temp.

z = 97.6 m K= 2  
time: 0 day 8 hour 0 min 0 s  
file: ./run3/an09ig3

Contours:  
increment: 5.00E-01  
labels multiplied by: 100E+01  
min: 2.589E+02; max: 2.700E+02

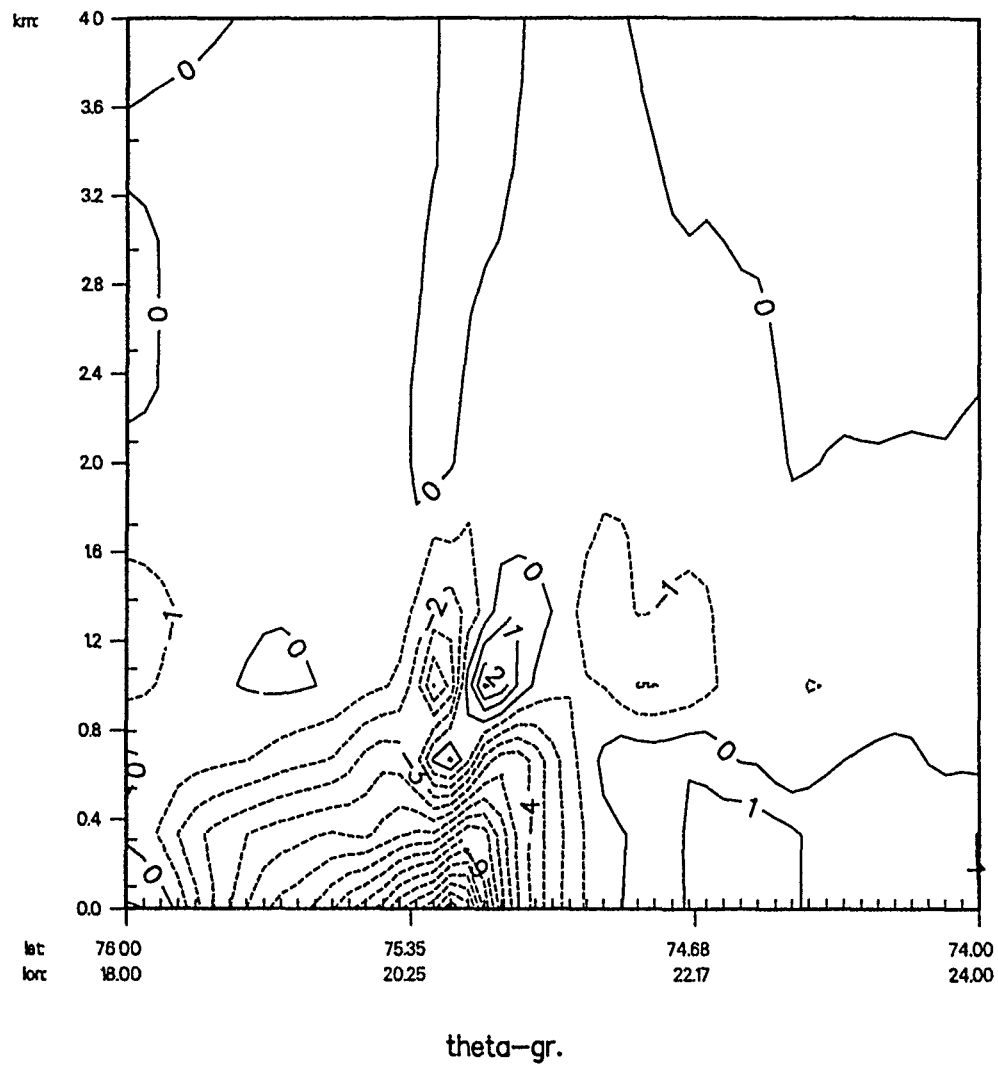
Fig. 5.39



time: 0 day 8 hour 0 min 0 s  
 file: an09ig3

Contours:  
 increment: 100E+00  
 labels multiplied by: 100E+00  
 min: 2600E+02; max: 2793E+02

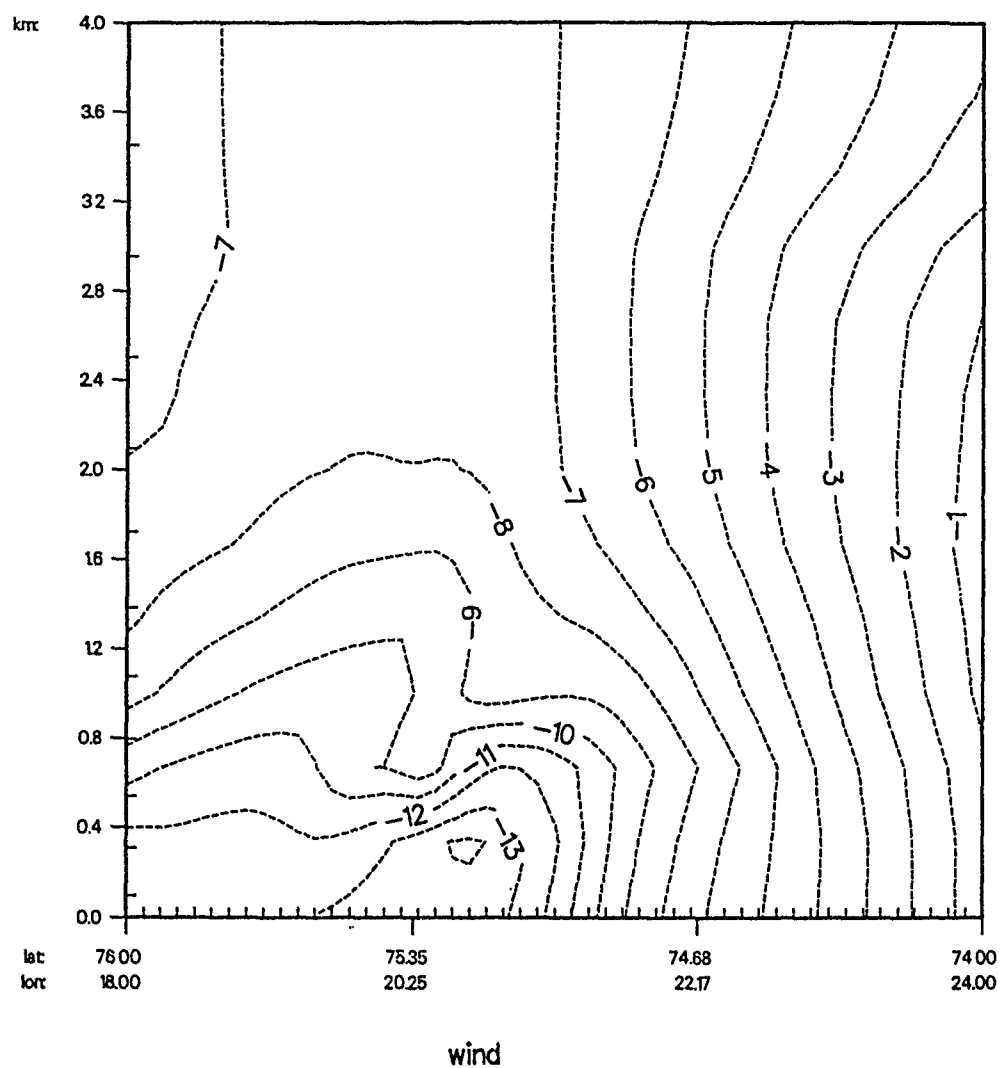
Fig. 5.40



time: 0 day 8 hour 0 min 0 s  
 file: an09ig3

Contours:  
 increment: 100E-05  
 labels multiplied by: 100E+05  
 min: -1.578E-04; max: 5.269E-05

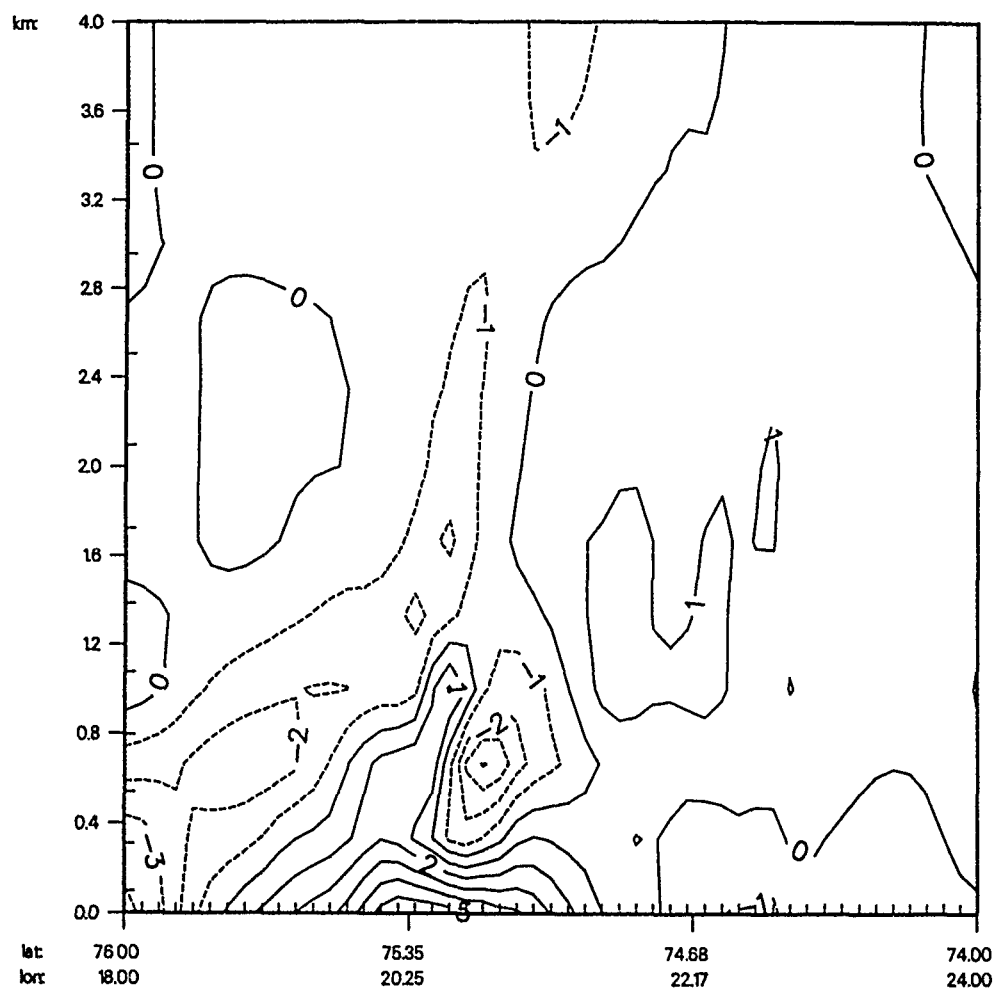
Fig. 5.41



time: 0 day 8 hour 0 min 0 s  
 file: an09ig3

Contours:  
 increment: 100E+00  
 labels multiplied by: 100E+00  
 min: -1414E+01; max: -4.719E-01

Fig. 5.42

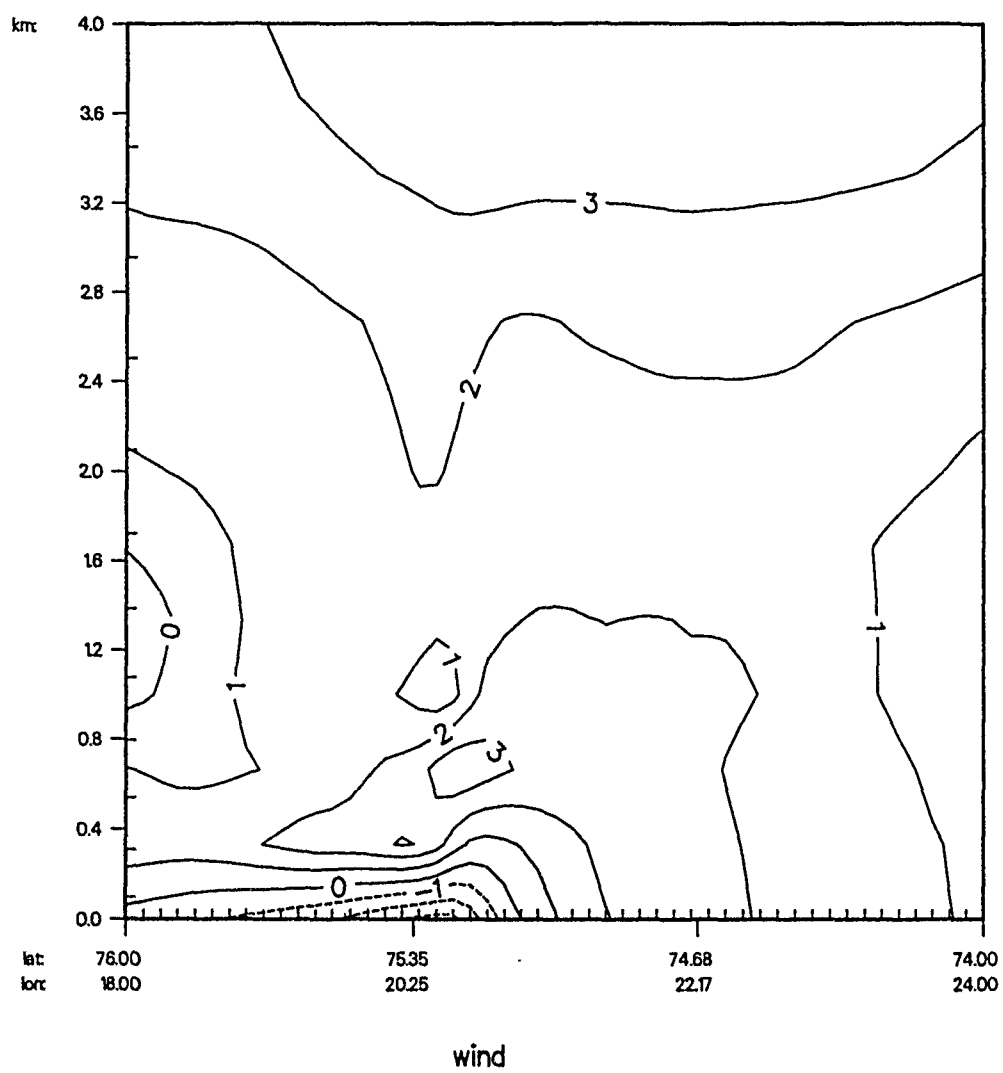


a-geo.

time: 0 day 8 hour 0 min 0 s  
file: an09ig3

Contours:  
increment: 100E+00  
labels multiplied by: 100E+00  
min: -4.636E+00; max: 5.947E+00

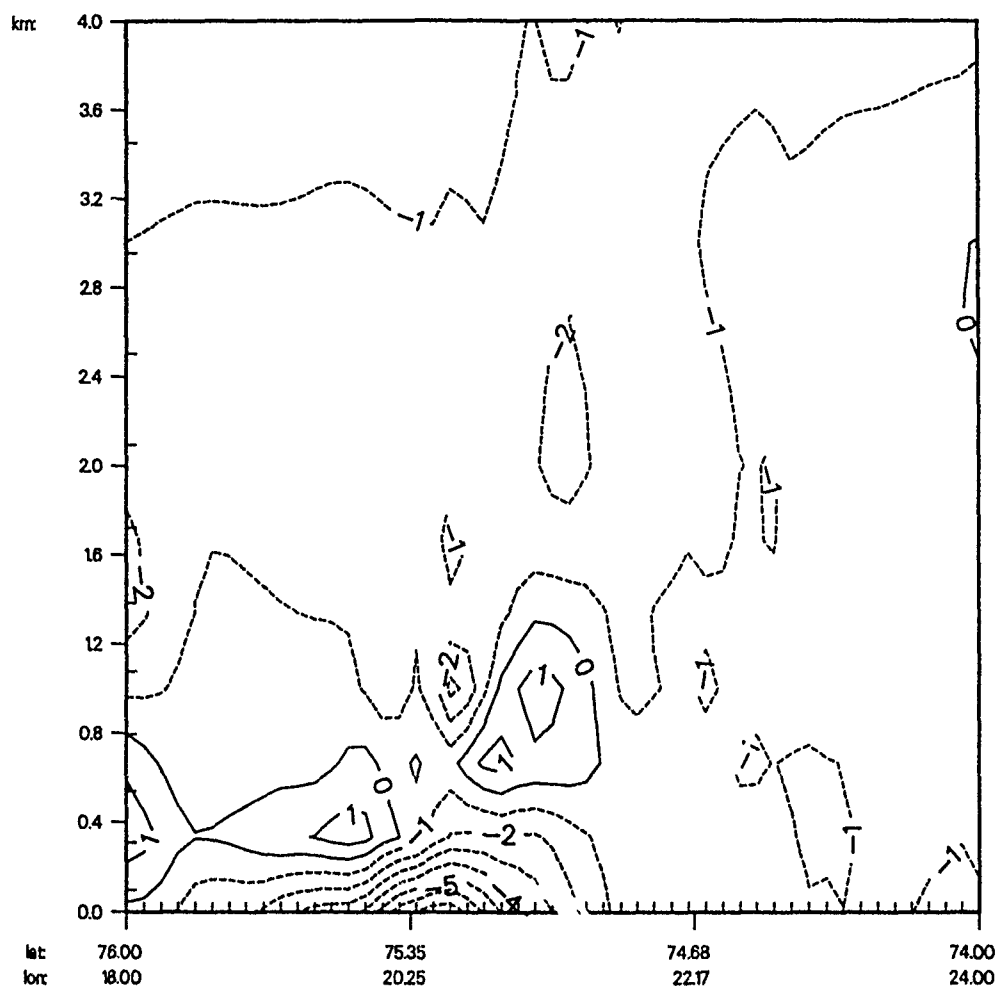
Fig. 5.43



time: 0 day 8 hour 0 min 0 s  
 file: an09ig3

Contours:  
 increment: 100E+00  
 labels multiplied by: 100E+00  
 min: -3.413E+00; max: 4.334E+00

Fig. 5.44

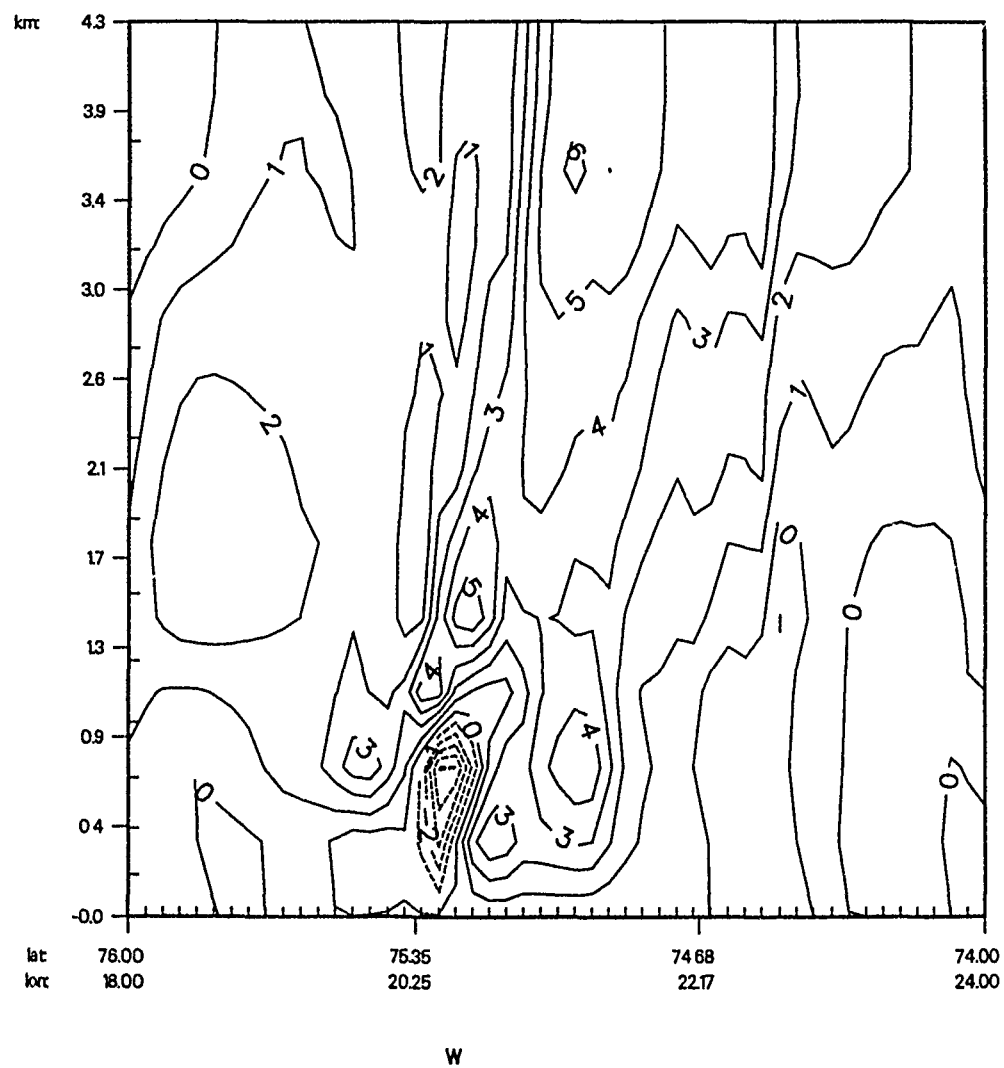


a-geo.

time: 0 day 8 hour 0 min 0 s  
 file: an09ig3

Contours:  
 increment: 100E+00  
 labels multiplied by: 100E+00  
 min: -7.669E+00; max: 2.145E+00

Fig. 5.45

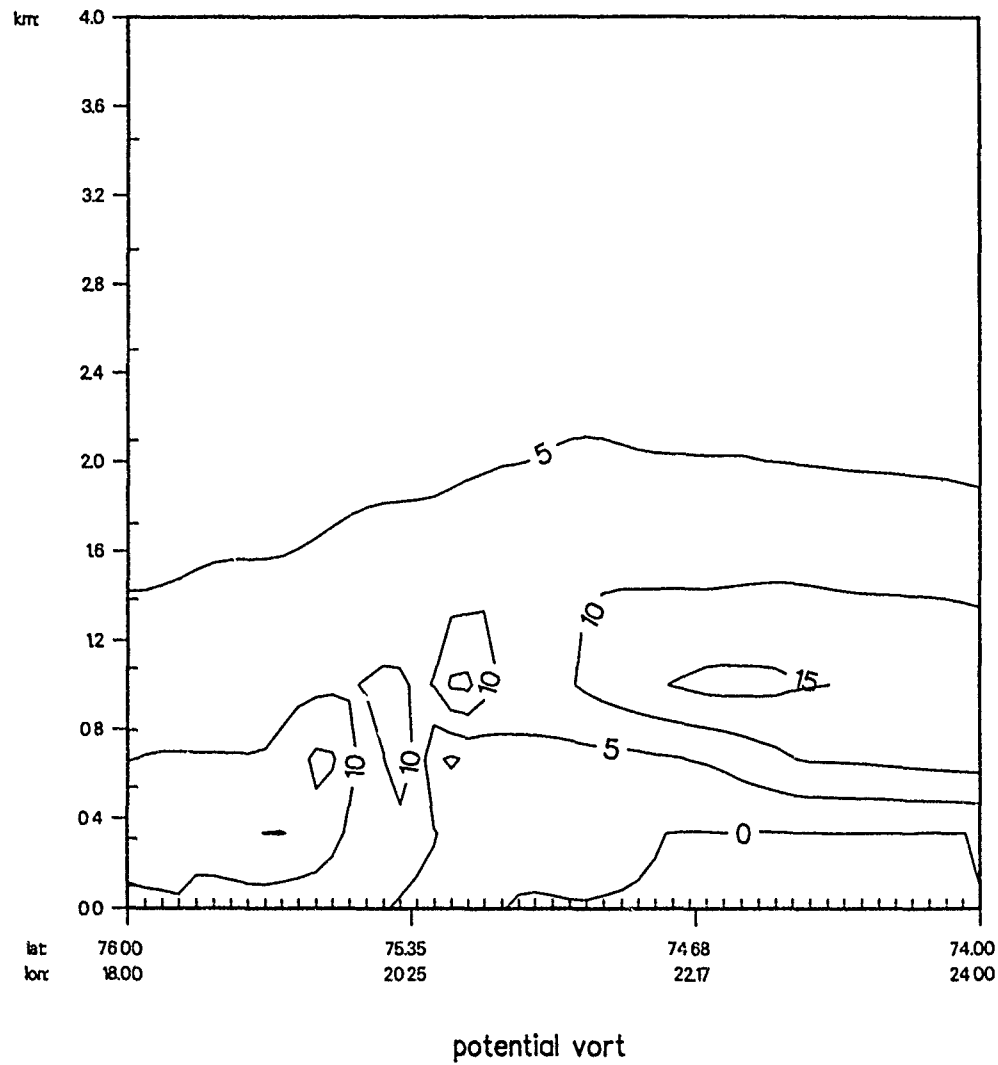


time: 0 day 8 hour 0 min 0 s  
 file: an09ig3

Contours:  
 increment: 100E-02  
 labels multiplied by: 100E+02  
 min: -5.116E-02; max: 6.175E-02

Fig. 5.46



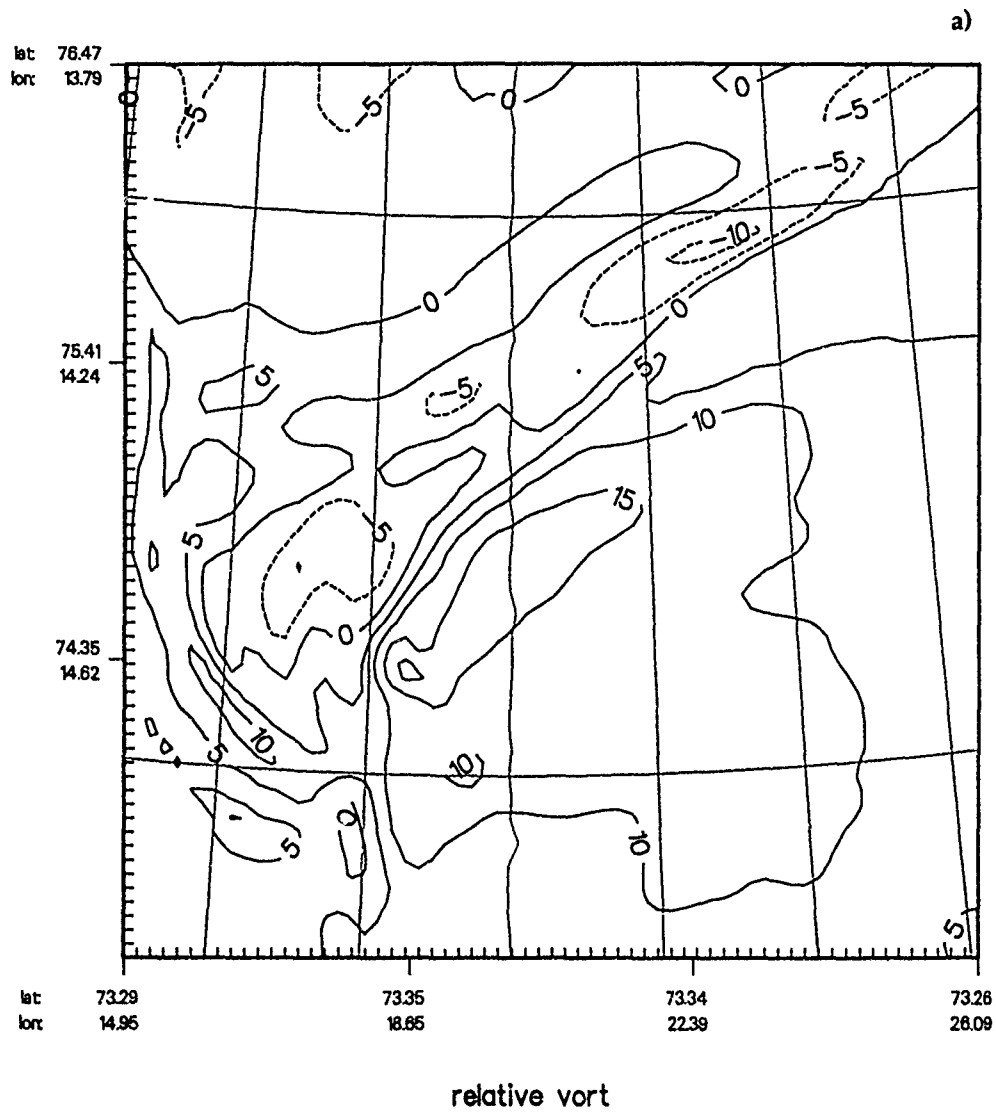


time: 0 day 8 hour 0 min 0 s  
 file: an09ig3

Contours:  
 increment: 5.00E-08  
 labels multiplied by: 100E+08  
 min: -2.339E-08; max: 2.156E-07

Fig. 5.47

run3:

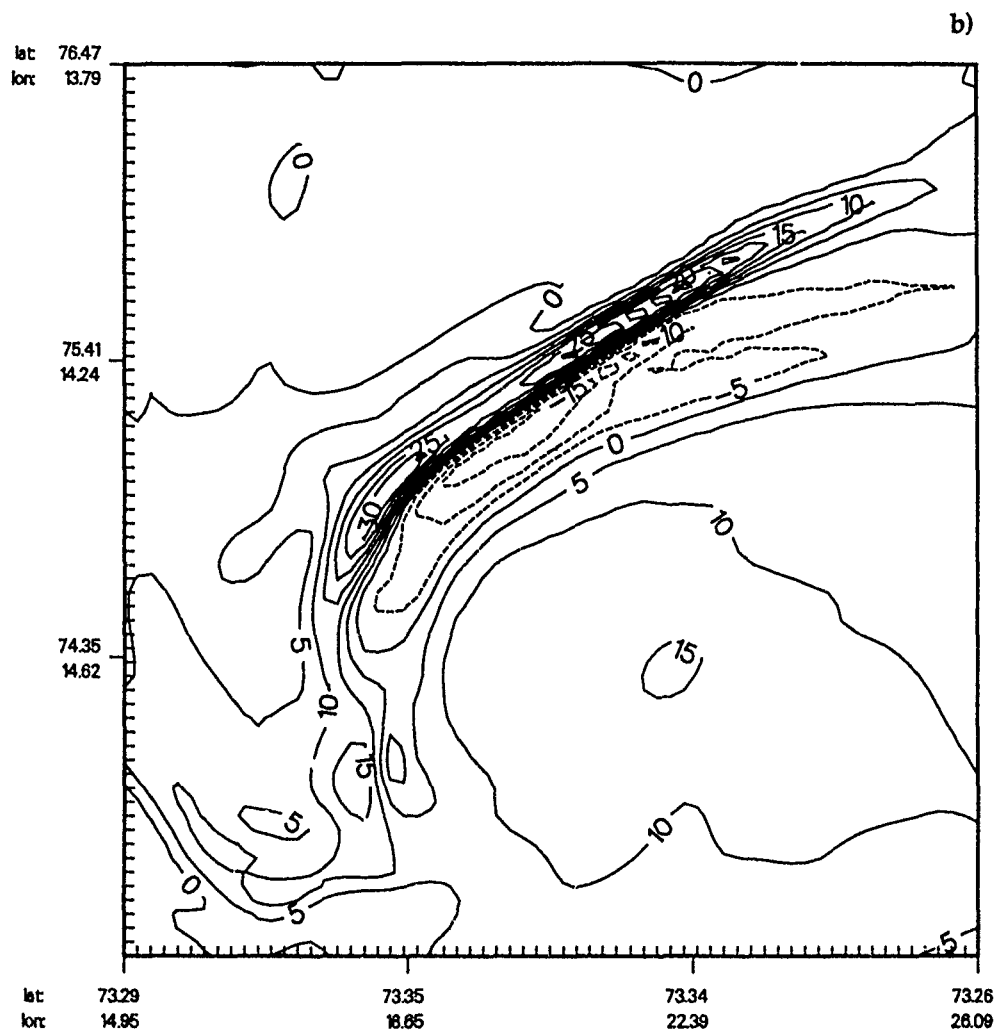


z = 307.4 m K= 3  
time: 0 day 8 hour 0 min 0 s  
file: an09ig3

Contours:  
increment: 5.00E-05  
labels multiplied by: 100E+05  
min: -1.127E-04; max: 2.108E-04

Fig. 5.48

run3:



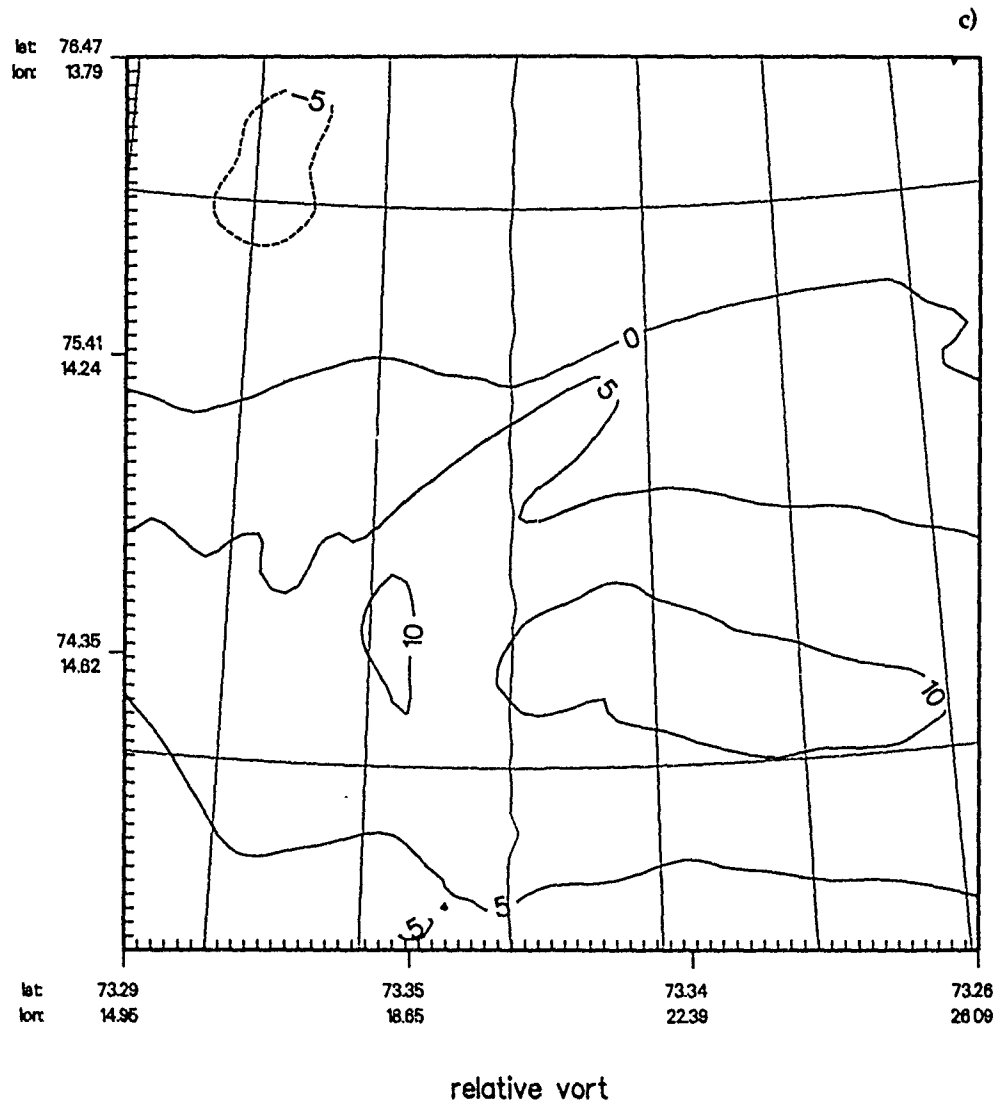
relative vort

z = 7919 m K= 5  
time: 0 day 8 hour 0 min 0 s  
file: an09ig3

Contours:  
increment: 5.00E-05  
labels multiplied by: 100E+05  
min: -1843E-04; max: 3.484E-04

Fig. 5.48

run3:



z = 1378.2 m K= 7  
time: 0 day 8 hour 0 min 0 s  
file: an09ig3

Contours:  
increment: 5.00E-05  
labels multiplied by: 1.00E+05  
min: -6.032E-05; max: 1.224E-04

Fig. 5.48

prist. ice mr

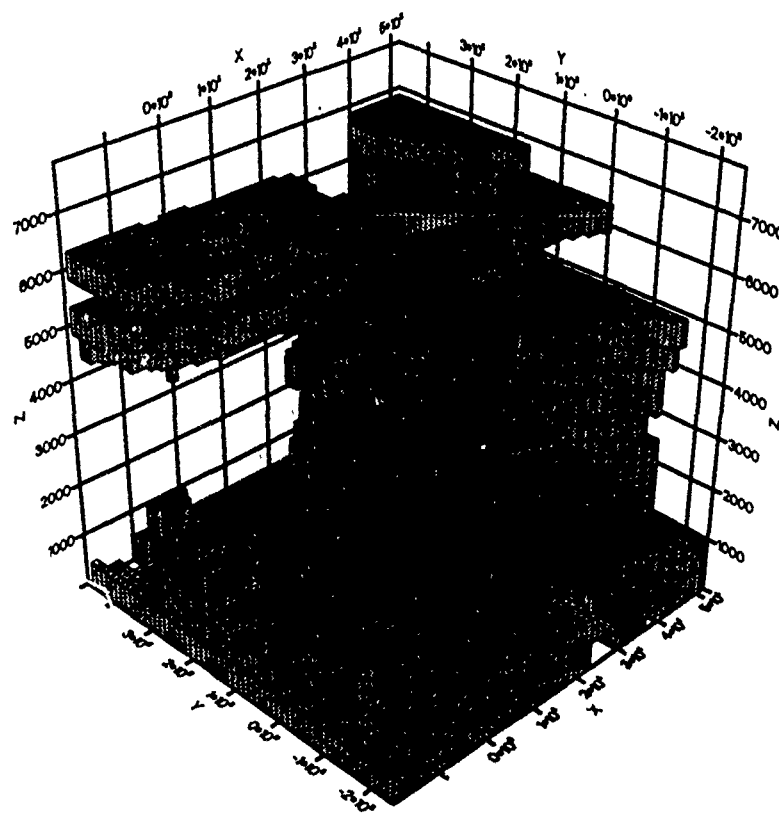


Fig. 5.49a

aggregates mr

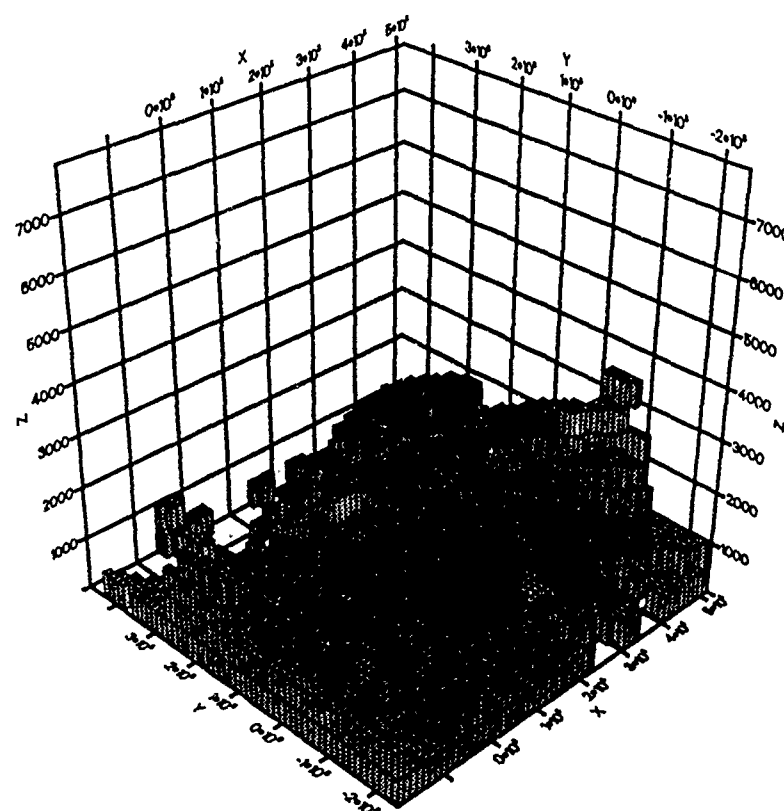


Fig. 5.49b